Hochschule für Angewandte Wissenschaften Hamburg
Hamburg University of Applied Science

Hamburg University of Applied Sciences

Faculty Life Sciences

Application of Deep Learning to Quantitative Susceptibility Mapping in MRI

Master Thesis

Biomedical Engineering

Submitted by Christine Geßner

Student number [redacted]

Hamburg

4th July 2019

First Examiner	Prof. Dr. Ing. Friedrich Ueberle	(Hamburg University of Applied Science)
Second Examiner	Dr. Jakob Meineke	(Philips Research Laboratories Hamburg)

Diese Abschlussarbeit wurde in Zusammenarbeit mit Philips Research erstellt.

Table of Contents

LIST OF ABBREVIATIONS ..... **V**

ZUSAMMENFASSUNG ..... **VI**

ABSTRACT ..... **VII**

1 INTRODUCTION **8**

2 FUNDAMENTALS **10**

2.1 MAGNETIC RESONANCE IMAGING 10

2.1.1 Physics *10*

2.1.2 Signal Acquisition *11*

2.1.3 Gradient Recalled Echo sequence *12*

2.2 QUANTITATIVE SUSCEPTIBILITY MAPPING 14

2.2.1 Magnetic Susceptibility *14*

2.2.2 Forward Solution *16*

2.2.3 Overview of Processing Steps in QSM *17*

2.2.4 Phase Unwrapping *17*

2.2.5 Background Field Removal *18*

2.2.5.1 Sophisticated Harmonic Artifact Reduction for Phase data (SHARP) 19

2.2.5.2 Projection onto Dipole Fields (PDF) 20

2.2.6 The inverse Problem of Dipole Inversion *20*

2.3 ARTIFICIAL NEURAL NETWORKS AND DEEP LEARNING 23

2.3.1 Orientation of Deep Learning in the Field of Machine Learning *23*

2.3.2 Artificial Neurons *23*

2.3.3 Fully-Connected Networks *24*

2.3.4 Optimization *25*

2.3.5 Loss Function *26*

2.3.6 Convolutional Neural Networks in Image Processing *26*

2.3.7 Transposed Convolutional Layer *29*

2.3.8 The U-net *29*

2.3.9 Challenges in Deep Learning *30*

3 MATERIAL AND METHODS **32**

3.1 DEEPQSM BASELINE MODEL 32

3.2 DEEPER ARCHITECTURE 34

3.3 EVALUATION CRITERIA AND LOSS FUNCTIONS 35

3.3.1 Weighted Image Gradient Loss *35*

3.3.2 Linear Regression Intercept and Slope *35*

3.3.3 Structural Similarity (SSIM) ... *35*
3.3.4 Root-Mean-Squared Error ... *36*
3.4 Data Generation for the Dipole Inversion Model ... 37
3.5 Data Generation for the Background Field Removal Model ... 39
3.5.1 Mask, Susceptibility Map and Local Field ... *40*
3.5.2 Total Field created with Offset ... *41*
3.5.3 Total Field created with external Susceptibility Sources ... *41*
3.5.4 Total Field created with stronger external Susceptibility Sources ... *41*
3.6 Data Generation for the Background Field Removal and Dipole Inversion Model ... 42
3.7 Numerical Brain Phantom ... 43
3.8 In vivo Scan Data ... 44
3.9 Libraries and Tools ... 46

4 RESULTS ... 47

4.1 ANN for Dipole Inversion ... 47
4.1.1 DeepQSM as Baseline for Evaluation ... *47*
4.1.2 Improving Model Performance ... *48*
4.1.3 Stability of DeepQSM ... *52*
4.1.3.1 Strong Susceptibilities ... 52
4.1.3.2 Cylinders ... 55
4.1.3.3 Scaling ... 56
4.1.3.4 Noise ... 57
4.1.3.5 Propagation of non-Dipole-Kernel Sources ... 58
4.1.4 Numerical Brain Phantom ... *59*
4.1.5 In-vivo Data ... *61*
4.1.6 Discussion ... *64*
4.2 ANN for Background Field Removal ... 66
4.2.1 Evaluation on Synthetic Data ... *66*
4.2.2 Evaluation with Numerical Brain Phantom ... *68*
4.2.3 In-vivo Scan Data ... *70*
4.2.4 Discussion ... *73*
4.3 Results ANN for both Background Field Removal and Dipole Inversion ... 74
4.3.1 Synthetic Validation Data ... *74*
4.3.2 Numerical Brain Phantom ... *76*
4.3.3 In-vivo Scan Data ... *77*
4.3.4 Discussion ... *80*

5 CONCLUSION ... 82

BIBLIOGRAPHY ... 84

List of Abbreviations

ANN	Artificial neural network
BFR	Background Field Removal
CNN	Convolutional neural network
COSMOS	Calculation of Susceptibility through Multiple Orientation Sampling
FCN	Fully Convolutional Neural Network
GRE	Gradient Recalled Echo
H	Hydrogen
LBV	Laplacian Boundary Value
MAE	Mean Absolut Error
MEDI	Morphology Enabled Dipole Inversion
MR	Magnetic Resonance
MRI	Magnetic Resonance Imaging
MSE	Mean Squared Error
PDF	Projection into Dipole Field
ppm	parts per million
QSM	Quantitative Susceptibility Mapping
ReLU	Rectified Linear Unit
RESHARP	Regularization based SHARP
RF	Radio Frequency
RMSE	Root Mean Squared Error
RNN	Recurrent neural network
ROI	Region of Interest
SD	Standard Deviation
SHARP	Sophisticated Harmonic Artifact Reduction for Phase Data
SMV	Spherical Mean Value
SSIM	Structural Similarity Index
SWI	Susceptibility Weighted imaging
TE	echo time in MRI
TKD	Truncated k-space Divison
TR	repetition time in MRI
VSHARP	variable kernel SHARP
WGL	Weighted Image Gradient Loss

Zusammenfassung

Magnetische Suszeptibilität ist eine physikalische Größe, welche die Magnetisierbarkeit von Stoffen in einem externen Magnetfeld beschreibt. Quantitative Susceptibility Mapping (QSM) ist eine MRT Methode welche diese Eigenschaft nutzt, um Bilder zu erstellen, welche Substanzen wie Kalzium oder Eisen hervorheben. Diese Substanzen sammeln sich bei Erkrankungen wie der Alzheimer Demenz, Multipler Sklerose oder der Parkinson-Krankheit vermehrt an. QSM nutzt die Phasenbilder von MRT Messungen um örtliche, durch Suszeptibilität verursachte Feldverzerrungen zu messen. Während es bekannt ist, wie man aus einer gegebenen Suszeptibilitätsverteilung das resultierende magnetische Feld erhält [1], stellt der umgekehrte Schritt für Aufnahmen die nur in einer Richtung aufgenommen wurden, ein inverses Problem dar [2]. Dies liegt daran, dass eine gegebene Feldverteilung unterschiedliche zugrundeliegende Verteilungen der Quellen haben kann. Um dieses Problem zu lösen, gibt es bereits verschiedene Methoden. Diese erfordern jedoch die Einstellung von selbstgewählten Parametern oder die Aufnahme in verschiedenen räumlichen Ausrichtungen. In dieser Arbeit wurde ähnlich wie bei [3] und [4] ein fully convolutional neural network (zu Deutsch etwa „vollkommen faltendes neuronales Netz“) benutzt um das inverse Problem der Dipolinvertierung zu lösen. Das Netzwerk war fähig das inverse Problem zu lösen und dabei vergleichbar gute Resultate gegenüber etablierten Methoden zu erzielen.

Zusätzlich zum Problem der Dipolinversion beinhaltet QSM das Problem der Hintergrundfeldentfernung. Hier erzeugen Suszeptibilitätsquellen außerhalb des Untersuchungsgebiet starke Hintergrundfelder, welche die schwachen Felder der lokalen Quellen überlagern. Diese starken Felder müssen erst entfernt werden, bevor eine Dipolinversion angewendet werden kann. In dieser Arbeit wurde ein weiteres CNN, ähnlich zum obigen, verwendet um die Hintergrundfelder zu entfernen. Des Weiteren wurde ein baugleiches drittes Netzwerk getestet, um die Dipolinvertierung und die Hintergrundfeldentfernung in einem Schritt zu durchzuführen. Letzteres wurde mit etablierten Methoden und den zwei aufeinander folgenden Netzwerken für Hintergrundfeldentfernung und Dipolinversion verglichen. Dabei erzielten die aufeinander folgenden Netze etwas bessere Ergebnisse als die Methode, welche beide Schritte in einem einzigen Netz durchführt. Obwohl verschiedene Datensätze ausprobiert wurden, zeigten alle von den Netzen erzeugten Bilder unterschiedlich stark ausgeprägte Hintergrundfeldartefakte, wenn sie auf in-vivo-Daten angewendet wurden. Des Weiteren hatten die erzeugten Bilder im Vergleich zu den etablierten Methoden deutlich breiter gestreute Werte. Um die Leistungsfähigkeit von Netzten welche Hintergrundfeldentfernung beinhalten zu verbessern, sollten die Trainingsdaten zukünftig besser an die Bildeigenschaften von in-vivo-Daten angepasst werden.

Abstract

Magnetic susceptibility is an internal tissue property that describes how tissue is magnetized by an external magnetic field. Quantitative Susceptibility Mapping (QSM) is a Magnetic Resonance Imaging (MRI) technique that uses this property to create images that highlight tissue containing substances such as calcium and iron. These substances accumulate with diseases as Morbus Alzheimer, Multiple Sclerosis or Morbus Parkinson. QSM uses the phase information of MRI to measure spatial field perturbations caused by magnetic susceptibility. While it is known [1] how to obtain the field-perturbation caused by a given susceptibility distribution, the step in reverse order represents an ill-posed inverse problem for single-oriented MRI scans because a certain field perturbation can be caused by several distributions of susceptibility sources [2]. To solve this problem several algorithms were introduced that demand manual parameter adjustment or the image acquisition from different angles. The regularization techniques are mostly generic and not specific to QSM. In this thesis, following Rasmussen et al. [3] and Yoon et al. [4] a fully convolutional neural network (FCNN) similar to the U-net [5] was explored to solve the problem of dipole inversion. The network is capable of solving the dipole inversion on in-vivo MRI phase data and shows similar results as established dipole inversion techniques.

In addition to dipole inversion, QSM includes the problem of background field removal. Strong fields of susceptibility sources outside of the region of interest (ROI) or outside the measurements cover the comparable small local fields of the ROI. These background fields have to be removed before dipole inversion can be applied. In this thesis a CNN, derived from the CNN for dipole inversion, was developed to remove the background field. Furthermore, a third model to solve background field removal and dipole inversion in a single step was developed and evaluated against the sequentially application of the single models and against established techniques. Here the sequentially applied networks showed slightly better results in total. Although datasets with total fields created differently were used, the resulting images showed background field artifacts to varying degrees if tested with in-vivo data. Furthermore, the created images had a significantly wider standard deviation than the results of established techniques. To improve the performance of models for background field removal the corresponding datasets have to be improved to reproduce the properties of in-vivo MR images.

1 Introduction

Numerous diseases that lead to long-term need of care alter the tissue composition in the brain. While Alzheimer disease is characterized by calcium deposits and microbleeds [6], Multiple sclerosis is accompanied by a loss of nerve-enveloping myelin fibers and iron depositions [7,8]. Both characteristics of Alzheimer's disease [9 11], Multiple Sklerosis [7,9,12,13], Parkinson's disease [14 18] and iron in blood [19] can be well detected and distinguished by Quantitative Susceptibility Mapping (QSM).

Quantitative Susceptibility Mapping (QSM) reconstructs the local tissue magnetic susceptibility from gradient echo MRI phase [20]. When placed in strong external magnetic fields of MRI scanners, the tissue is magnetized proportionally to its magnetic susceptibility. This magnetization in turn perturbs the magnetic field leading to variations of the Larmor frequency, i.e. variations of the off-resonance field map. The resulting magnetic field of tissue is well-described by a convolution with the so-called dipole kernel [1]. However, due to the existence of a conical region along which the dipole vanishes, the inverse problem from field to susceptibility (so-called dipole inversion) is ill-conditioned for data that was acquired in only one orientation.

Next to the problem of dipole inversion, QSM includes the problem of background field removal [2]. Here, strong fields with sources outside of the region of interest (ROI) and measured field of view cover the images. These fields are called background fields while the fields created by the ROI are called local fields [2].

Over the recent years, researchers have developed a variety of different regularization approaches for both background field removal and dipole inversion, enabling the use of single-oriented data for QSM. These include MEDI [21], TKD [22], COSMOS [23], STAR-QSM [24] for dipole inversion and LBV [25], PDF [26], SHARP [27] for background field removal. However, these regularization approaches are not specific to QSM and use manual chosen parameters.

Recently, deep learning approaches like QSMnet [4] and DeepQSM [3] have been used to overcome the ill-posed problem of dipole inversion. The authors of QSMnet used brain images of 60 brain scans that were acquired by using the COSMOS method [23]. COSMOS uses different orientations for scanning to overcome the ill posed problem of dipole inversion. This data was used for training and was able to improve the state-of-the-art methods for QSM. In contrast, the authors of DeepQSM used synthetically generated data containing simple geometric objects as cuboids and spheres to train the network.

Next to the problem of dipole inversion, deep learning methods were recently used to overcome the problem of background field removal. SHARQnet [28] uses simulated background fields for

training. In this thesis, the approaches of DeepQSM and SHARQnet are evolved as for both no scans are necessary to create the training data.

Finally, yet importantly, QSM cannot only be used for the detection of the above-mentioned diseases. Further applications are imaging of cerebral microbleeds [19], deep brain stimulation [29], Chorea Huntington [30], Amyotrophic Lateral Sclerosis [31,32], oxygen metabolism [2] and iron depositions like Wilson's disease [33]. Next to the application for brain imaging, QSM could be used in other organs and to map mineralization for measuring bone strength [34].

2 Fundamentals

To understand the problem of QSM and the methods to overcome them, this chapter explains both the physics of QSM and the basics of artificial neural networks (ANNs). Chapter 2.1 introduces the phase image acquisition in magnetic resonance imaging (MRI) that is important to understand later post processing steps like phase-unwrapping. Chapter 2.2 explains the tissue property of magnetic susceptibility and how it can be used to obtain images with enhanced tissue contrast. The different processing steps to obtain a susceptibility distribution out of a phase image are explained in detail and conventional algorithms and their limitations are presented. Chapter 2.3 presents the basics of artificial neural networks (ANNs). Here, the focus lies on convolutional neural networks that are well-suited to process image data. The U-net network architecture (see Section 2.3.8) is explained that was the starting point for the architecture of DeepQSM and QSMnet.

2.1 Magnetic Resonance Imaging

Next to the fundamental insights into the physics behind MRI, this section describes phase images and the MRI sequence Gradient Recalled Echo (GRE) to acquire such images.

2.1.1 Physics

MRI is a noninvasive imaging method that creates three dimensional images with high soft tissue contrast [35]. It makes use of the spin property of hydrogen nuclei that are abundant in water, fat and amino acids. As Hydrogen has an odd number of protons and no neutrons the nucleus has a nuclear spin. A spin is a property of particles that is similar to the angular momentum in classical physics; however, it interacts with electro-magnetic fields because of its magnetic moment which is linked to spin by gyromagnetic ratio. This way, the proton strives to maintain the spatial rotation of its rotational axis but can be influenced by electro-magnetic fields [35].

In contrast to classical physics, atoms can only assume certain energy states. In the case of H protons, the spin can only assume two states: Parallel or antiparallel to the external magnetic field. Due to the thermal energy, without a strong external field both states are equally likely. No own magnetic field is measurable as both states equalize each other. Only in the presence of a strong external magnetic field B_0 (usual range of 1 3 Tesla) does a slight excess of the parallel alignment occur and their net magnetic dipole moments M_0 sum up in the direction of B_0 (longitudinal). The spins precess around the B_0 axis with different phases so the transversal net magnetization is zero. The alignment of M_0 can be manipulated by further external magnetic sources. In MRI this further source is a short radio frequency pulse B_1 that has a far weaker magnetic field (ca. 1 µTesla) but can tilt M_0 by a defined angle (so-called flip-angle) as it uses the resonance frequency of the spin to

excite it. After the B_1 RF pulse finishes the magnetic dipole will return in its original alignment preceding like a gyro due to its angular moment.

The energy that is released due to this in form of radio waves, is measured in MRI by receiver coils. The frequency of the precession and the resonance RF pulse is called Larmor (angular) frequency ω and depends on the strength of the magnetic field B_0. It can be described as:

$$\omega \quad 2\pi \cdot f \quad \gamma \cdot B_0 \tag{2.1}$$

Where γ is the gyromagnetic ratio a nuclide specific constant with a value of $2.68 \cdot \frac{10^8 rad}{s}/T$ for a H proton (and $\gamma/2\pi$ is 42.6 MHz/T). In case of an external magnetic field of 3 Tesla the measured Larmor frequencies of H protons are around 128 MHz.

2.1.2 Signal Acquisition

Inductive coils measure the signal that occurs when the spin precesses from the flip-angle deflection by the B_1 RF pulse back to the original alignment in B_0 direction. The coils are arranged perpendicular to the direction of the B_0-field (that is conventional the z-direction) as can be seen in Figure 1. In z-direction results the summed up longitudinal magnetic moment M_0. The rotations around the z-axis of the various H protons are not coherent so no transverse magnetization (in x or y direction) is measurable in the receiver coils (see Figure 1).

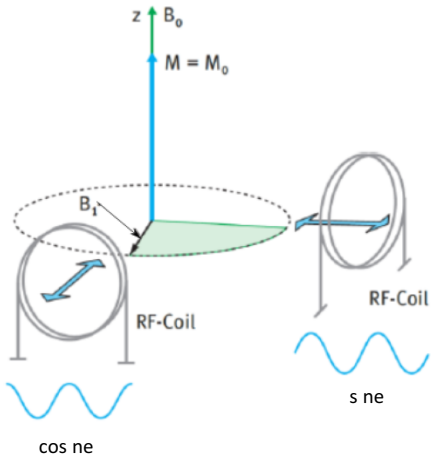

F gure 1: Two rece ver co s are arranged vert ca y to rece ve the s gna perpend cu ar. Source: [36]

Only if the B_1 RF pulse tilts M_0, M_0 can be divided into a vector of M_{xy} and M_z and the receiver coils acquire a signal (see Figure 2).

The rotation of the transverse magnetization M_{xy} can be expressed as complex signal (x stands for the real part and y stands for the imaginary component). The resulting magnitude is defined as:

$$|M_{xy}| \quad \sqrt{M_{real}^2 + M_{imaginary}^2} \tag{2.2}$$

The corresponding phase is defined as:

$$\varphi \quad \arctan\frac{M_{imaginary}}{M_{real}} \tag{2.3}$$

As the signal is complex the phase can take values in the interval of $[-\pi, \pi]$.

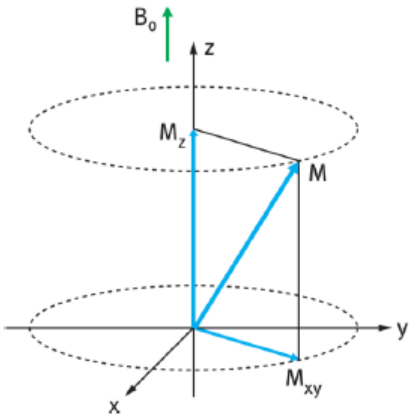

F gure 3: The magnet zat on vector M can be sp t nto a ong tud na component Mz and a ong tud na component Mxy. Source: [36]

When the B_1RF pulse finishes, M_0 will turn back in B_0 direction and M_z increases while M_{xy} decreases. The time of the B_1 RF pulse and the back precession is in the range of milliseconds and seconds.

In MRI, different B_1 pulse and field gradient settings (so-called MRI sequences) can be distinguished to acquire signals. The most common MRI sequence is the spin echo that results in $T1$ and $T2$ weighted images. To obtain additional information about susceptibility effects the MRI sequence Gradient Recalled Echo is used. It acquires $T2^*$ information and is explained in the following section.

2.1.3 Gradient Recalled Echo sequence

Gradient Recalled Echo (GRE) is an MRI sequence that can acquire phase perturbations caused by magnetic susceptibility. Susceptibility sources, chemical shift and inhomogeneities of the B_0 field (imperfect shimming) cause the field inhomogeneities ΔB. In contrast to the group of spin echo sequences, GRE does not refocus spins dephased by magnetic field inhomogeneities ΔB [37]. Due to this, the phase of the inhomogeneities accumulates over time.

Interactions between adjacent protons cause the transverse relaxation (dephasing) that is described by the T2 constant. This relaxation is not reversible until a new B_1 RF pulse occurs. However, the dephasing effects of local inhomogeneity ΔB are reversible and characterized by T'. Together, T2 and T' form T2*. GRE measures the transverse relaxation (dephasing) constant $T2^*$, that contains information about magnetic field inhomogeneity ΔB_0 [37]:

$$\frac{1}{T2^*} \quad \frac{1}{\mathrm{T2}} + \frac{1}{\mathrm{T'}} \quad \frac{1}{\mathrm{T2}} + \gamma \Delta B_0 \tag{2.4}$$

This T2* constant is measured in GRE (see Figure 4 for explanation) while it is eliminated in spin-echo by a 180° RF pulse [37].

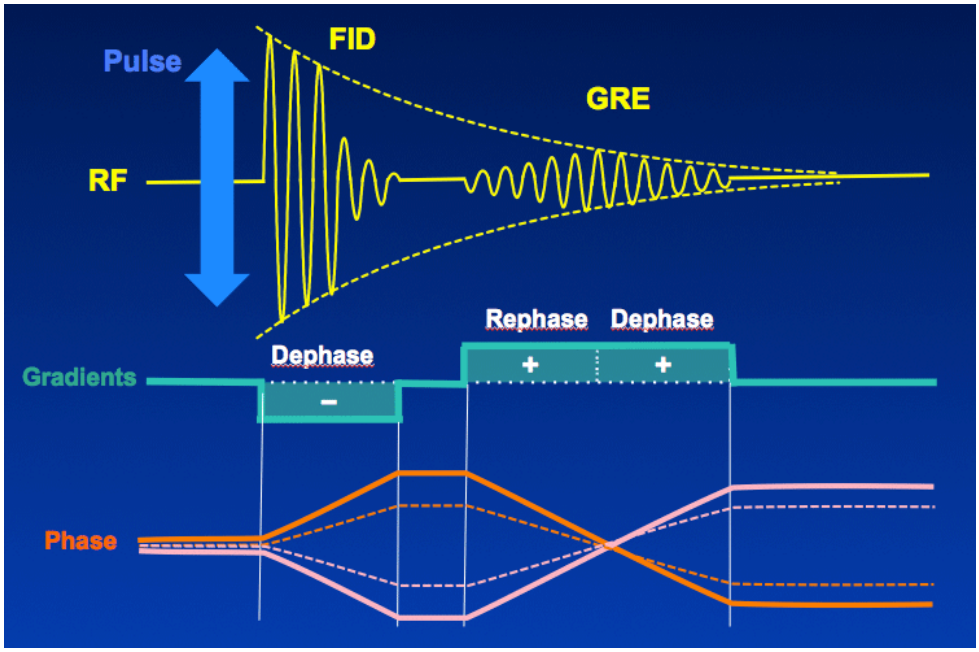

F gure 4: The negat ve grad ent acce erates the dephas ng of the sp ns so the rece ved s gna f rst van shes. Then the pos t ve grad ent rephases the sp ns aga n and a grad ent reca ed echo (GRE) becomes measurab e n the rece ver co s. The t me from RF pu se to GRE s the echo t me TE. For every ne n k-space the grad ents are adjusted d fferent so the phase sequence d ffers (v sua zed by orange, dotted and p nk nes). Source: [38]

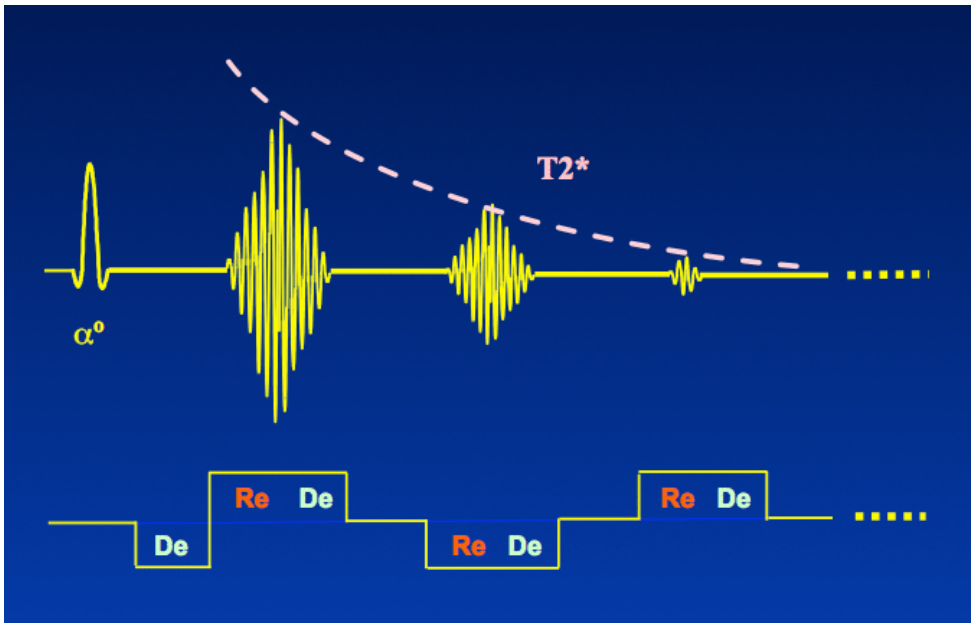

F gure 5: By repeat ng the dephas ng, one exc tat on creates severa echoes. Late echoes are used to acqu re sma f e d perturbat ons. The s gna peak of the echo s m ted by the enve ope of T2*. Source: [39]

2.2 Quantitative Susceptibility Mapping

This section focuses on the physics of magnetic susceptibility. In the first section, magnetic susceptibility and its role in MRI imaging is explained. The following sections describe the steps to reconstruct a susceptibility map out of a phase image encompassing phase unwrapping, background field removal and dipole inversion. For the processing steps of background field removal and dipole inversion, conventional methods and their limitations are explained (see Section 2.2.5, Section 2.2.6). These methods are used in Chapter 4 for comparison with results of the deep learning models developed in this thesis (see Section 3.1).

2.2.1 Magnetic Susceptibility

Magnetic susceptibility χ is a measure of the extent a material gets magnetized in a magnetic field. Materials with a positive susceptibility are called paramagnetic and align with the magnetic field while in case of a negative susceptibility they align against it and are called diamagnetic (see Table 1).

	Diamagnetic	Paramagnetic	Ferromagnetic
Susceptibility χ	$\chi < 0$	$\chi > 0$	$\chi >> 0$
Alignment to external field	anti-aligned	aligned	aligned
Total magnetic field	Decreases / disperse	Increases / concentrate	Increases / concentrate
Material examples [2]	H_2O, Myelin, oxyHb	O_2 [40], Gadolinium, deoxyHb	Fe, Co, Ni

Tab e 1: Overv ew of d amagnet c, paramagnet c and ferromagnet c propert es.

The material in the magnetic field creates an extern magnetic field in its surrounding. Due to its alignment (that depends on its susceptibility value; see Table 1) the resulting total magnetic field will increase or decrease. Further explanations about how the atomic structure of tissue determines its susceptibility can be found in [2].

As susceptibility is a tissue specific property it can be used to enhance the contrast between tissues with different susceptibility values (see Figure 6). Especially blood, calcifications and the deep gray matter nuclei can be well distinguished [2].

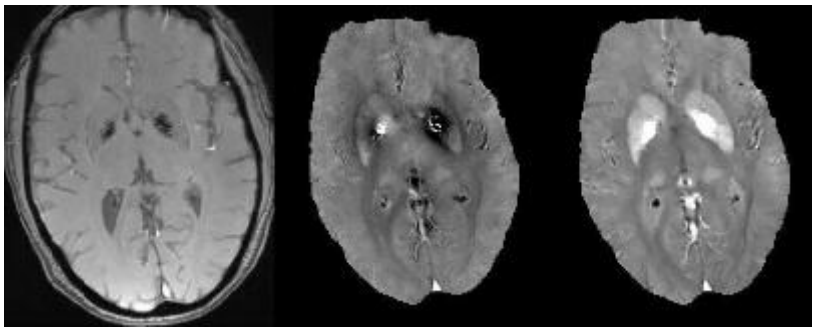

F gure 6: Magn tude, phase and QSM mage of a bra n : The magn tude shows tt e contrast, the f e d map shows d rect on dependent f e d perturbat ons caused by suscept b ty, the QSM mage shows the spec f c suscept b ty of the d fferent bra n t ssues. Source: [41]

Water has a susceptibility of -9.04 ppm [2] and is used as reference to describe relative susceptibility differences in the body. These differences (towards water) range from -0.1 ppm for myelin to +0.3 ppm for iron-rich tissue. Brain hemorrhages can have values up to 1 ppm but are pathological. Air that contains paramagnetic oxygen has a susceptibility of 0.36 ppm [42]. Due to this, the highest susceptibility changes are at air-tissue interfaces (+0.36 vs. -9.04 ppm) while the differences in tissue are comparatively small.

In MRI, these changes in the magnetic field result in susceptibility artefacts: e.g. high susceptibility differences at the paranasal sinuses interfaces lead to variations of the magnetic field in neighboring areas. In these cases, the fields superimpose and falsify the susceptibility value of the tissue. In the case of the sinuses, the Larmor frequency changes in the nearby brain tissue. Due to this, transverse dephasing is accelerated and causes signal loss [43] (see Figure 7). This loss particularly occurs in gradient echo images at long echo times. Using certain MRI sequences, these field perturbations can create new types of MR images with increased contrast. The whole process to obtain a susceptibility distribution out of phase images is called Quantitative Susceptibility Mapping.

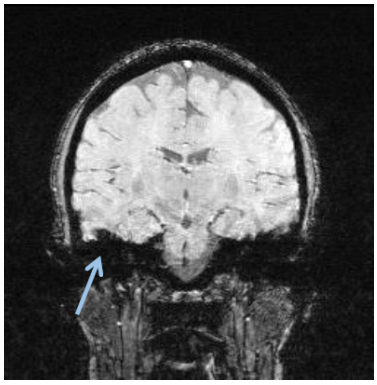

F gure 7: GRE magn tude mage. The f e d of the a r-t ssue nterface causes a fa se ndentat on n the bra n. Source: [44]

In addition to the susceptibility distribution, the measured field perturbations depend on the orientation of the object [35]. In particular, the orientation dependency is significant for objects like cylinders as shown in Figure 8. In the brain, nerve fibers and blood vessels form cylindrical objects.

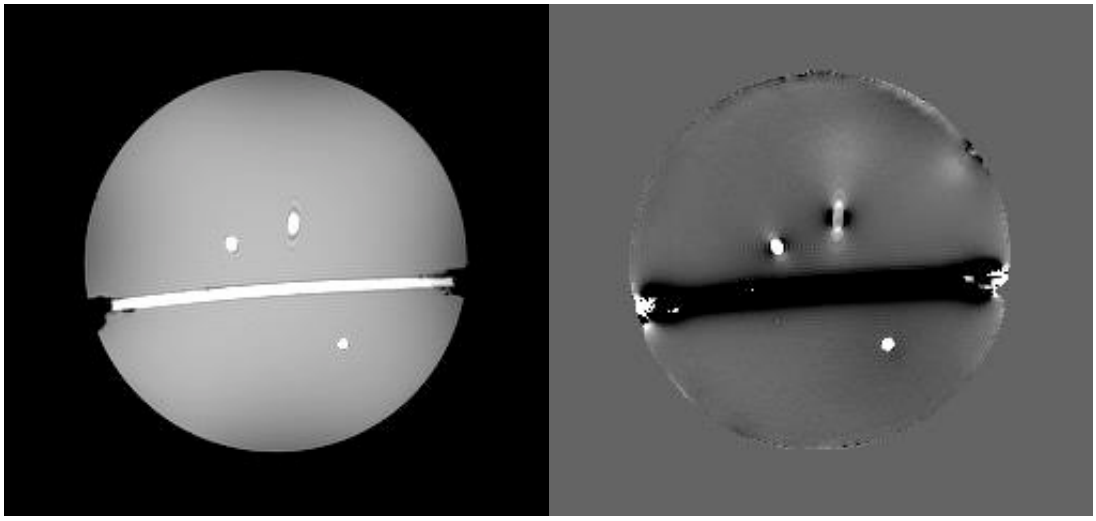

Figure 8: Phantom with cylinders in perpendicular orientations. Left: Magnitude image with no susceptibility effects. Right: Preprocessed field map image with different values depending on the orientation of the cylinders. The paramagnetic cylinder has a positive phase shift (white) while the perpendicular cylinder has a negative one (black). Source: [44]

2.2.2 Forward Solution

Due to susceptibility, materials that are exposed to a strong external magnetic field form an additional internal magnetic field. The internal field of a single susceptibility source at a distance r within an external field B_0 that points into z-direction is defined as:

$$\Delta \boldsymbol{B}(r) \quad \frac{\mu_0}{4\pi} \int d^3\boldsymbol{r}' \left(\frac{3\boldsymbol{M}(\boldsymbol{r}') \cdot (\boldsymbol{r} \quad \boldsymbol{r}')}{|\boldsymbol{r} \quad \boldsymbol{r}'|^5} (\boldsymbol{r} \quad \boldsymbol{r}') \quad \frac{\boldsymbol{M}(\boldsymbol{r}')}{|\boldsymbol{r} \quad \boldsymbol{r}'|^3} \right) if\ \boldsymbol{r} \neq \boldsymbol{r}' \tag{2.5}$$

where μ_0 is the permeability of vacuum and M is the induced magnetization.

The field induced by several susceptibility sources at a certain spot can be expressed as a sum of these several fields at this spot (superposition). For susceptibility values <<1 and isotropic material the equation can be simplified, converted (among others by the Lorentz correction), and transformed into Fourier space (also called k-space) to obtain the relative induced field perturbation δ_B (see Equation (2.6)) of a susceptibility source. Details about the transformation of the equation can be found in [1,45]. Interpreting this equation as a convolution of the susceptibility distribution χ with a kernel D in k-space, we get:

$$\begin{cases} \delta_B(\boldsymbol{k}) & D(\boldsymbol{k}) \cdot \chi(\boldsymbol{k}) \\ where, D(\boldsymbol{k}) & \frac{1}{3} \quad \frac{\boldsymbol{k}_z^2}{\boldsymbol{k}_x^2 + \boldsymbol{k}_y^2 + \boldsymbol{k}_z^2} \end{cases} \tag{2.6}$$

Where k refers to the three directions in k space. The image has to be transformed by an inverse Fourier Transform into image space to obtain a field map. However, the anisotropic characteristic of susceptibility (that is not further part of this thesis) is not included in this formula.

The appearance of the kernel for a single source is shown in Figure 12. In practice, there are many sources present and the field at a certain location is the sum of contributions from the fields of all surrounding magnetic dipole sources [2]. With equation 2.6 a field perturbation can be calculated from a given susceptibility distribution, also called 'forward-solution' [1,45].

2.2.3 Overview of Processing Steps in QSM

Quantitative Susceptibility Mapping (QSM) is the process to transform a raw phase image that was acquired by a GRE MRI scan to a susceptibility map that shows tissue-specific susceptibility values. To do so, several steps have to be performed. First, the raw phase image is 'unwrapped' to remove wrapping artefacts (see Section 2.2.4). The unwrapped phase image contains field perturbations from outside of the ROI or field of view that are removed by 'background field removal' (see Section 2.2.5). The field map shows the field perturbations caused by the susceptibility sources in the ROI. The last step is called 'dipole inversion' and reverses the field distribution to a susceptibility distribution. The processing chain is visualized in Figure 9.

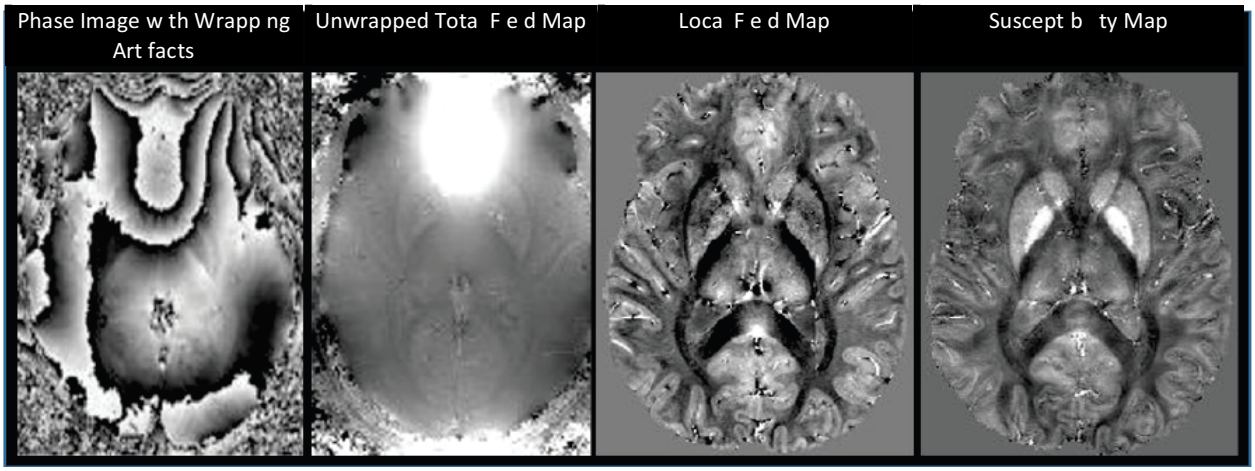

F gure 9: Steps to perform QSM: The raw phase mage has to be unwrapped f rst. Afterwards, a background f e d remova s performed to obta n a oca f e d map. D po e nvers on descr bes the step of so v ng the -posed prob em of transforming the oca f e d map to a suscept b ty map. Source: [46]

2.2.4 Phase Unwrapping

In addition to the magnetic field B_0 and gradient fields, eddy currents and tissue susceptibility cause further magnetic fields [47]. In consequence, the occurring field perturbations ΔB change the precession frequencies and ΔB accumulate phase shifts. In addition to the magnetic field B_0 and gradient fields, eddy currents and tissue susceptibility cause further magnetic fields [47]. In consequence, the occurring field perturbations ΔB change the precessing frequencies (so-called variations in the off-resonance field map) and accumulate phase shifts over the time of signal acquisition in GRE. A larger field perturbation causes a larger change in the frequency and accumulates a longer phase shift. The phase shift $\Delta\varphi$ at the echo time TE is defined as follows:

$$\Delta\varphi \quad \gamma\Delta B \cdot TE \tag{2.7}$$

The total measured phase is the sum of the original phase φ_0 at t=0 and the phase shift $\Delta\varphi$ caused by field inhomogeneities:

$$\Delta\varphi \quad \gamma\Delta B \cdot TE + \varphi_0 \tag{2.8}$$

In MRI the phase is measured as an angle of the vector M_{xy} (see Figure 10) in the range of [-π, π].

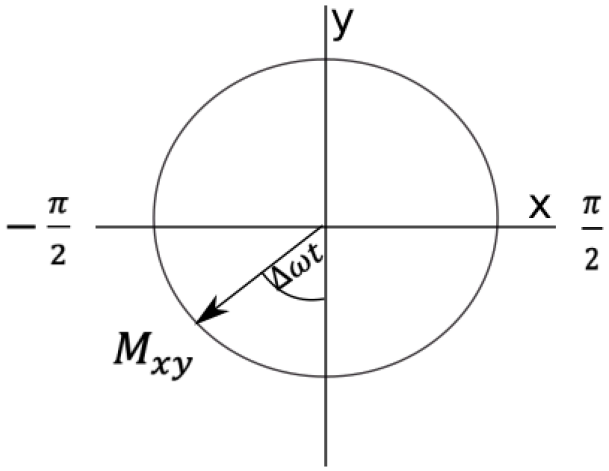

F gure 10: The transversa component of the vector M has a phase that can take on va ues between$[-\pi, \pi]$. If the vector exceed these va ues they start aga n at $-\pi$ or π and a phase wrap appears n the mage.

Phase values greater than π are wrapped and start again at $-\pi$, so the measured phase will always be in the range of $[-\pi, \pi]$.

$$\varphi_{actual} \quad \varphi_{measured} + n \cdot 2\pi \tag{2.9}$$

Consequently, in phase images at the boundaries of π to $-\pi$ phase jumps of 2π occur (see Figure 9, raw data). The process to obtain the smooth actual phase is called phase unwrapping and is ill-posed [2]: Due to noise and averaging values to define finite voxel volumes the jumps are not exactly 2π. Among others, path finding algorithms and global error minimization can be used to perform phase unwrapping [2].

2.2.5 Background Field Removal

In QSM usually the brain is the ROI that is examined. Susceptibility sources from regions where no signal is available (outside of the field of view) and from regions outside of the desired ROI create dominant field perturbations in the area of the brain (within the ROI) (see Figure 9, total field). In case of a brain examination, MRI measures the total magnetic field (B_{total}) in the ROI consisting of the magnetic field (B_{local}) caused by the brain tissue and the magnetic field caused by skull, eyes, neck and air-tissue interfaces ($B_{background}$):

$$B_{total} \quad B_{local} + B_{background} \tag{2.10}$$

Field perturbations are created only by spatial changes in the susceptibility distribution [48]. Most organic tissue varies around -9ppm while air has a susceptibility close to zero. Hence, air-tissue interfaces form the strongest field perturbations that are around two orders of magnitude higher than the local field. In addition to the surface of the skull, the paranasal sinuses form an air-tissue interface. To solve the problem of dipole inversion the background field is removed first.

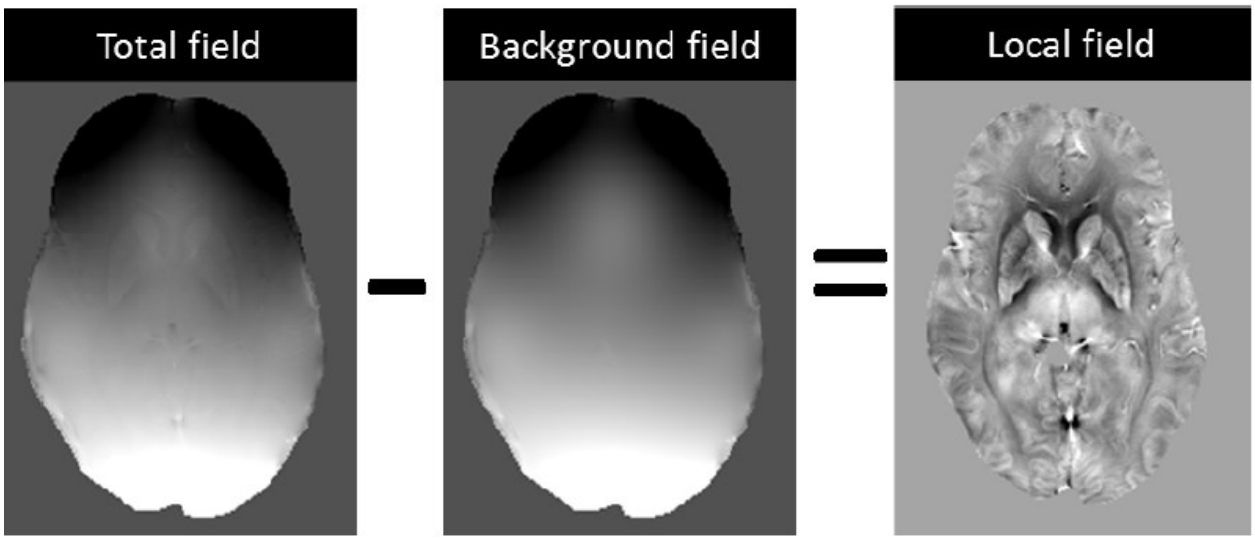

F gure 11: The Background f e d s the dom nant f e d and s removed to revea the oca f e d. Source: [47]

Several methods exist to perform background field removal. The simplest is the application of a high pass filter [49] as the background field consist mainly out of low frequencies. However, in the area of air-tissue interfaces the background field changes rapidly and is not removed. Furthermore, low frequencies of the local field are also removed. Techniques that are more effective are the optimization-based Projection onto Dipole Field (PDF) [26] and the kernel-based Sophisticated Harmonic Artifact Removal for Phase data (SHARP) [27].

2.2.5.1 Sophisticated Harmonic Artifact Reduction for Phase data (SHARP)

SHARP uses the spherical mean value (SMV) property and the division into harmonic and non-harmonic field functions to remove the background field. A static field is harmonic if it satisfies the Laplace equation (the second order partial derivative is equal to zero). In the case of susceptibility, the Laplace equation is valid for background fields inside the ROI [2]. Due to this, second order derivatives of the background field $B_{background}$ in the ROI are equal to zero [50]:

$$\nabla^2 B_{background}\big|_M \quad 0 \tag{2.11}$$

Background fields outside the ROI or internal fields inside the ROI are expressed by Poisson's equation (second order partial derivative equals another function) and are non-harmonic. With the characteristics of the background and local field inside the ROI, the B_{total} is calculated as follows [50]:

$$\nabla^2 B_{total}|_M \quad (\nabla^2 B_{local} + \nabla^2 B_{background})\big|_M \quad \nabla^2 B_{local}|_M + 0 \tag{2.12}$$

The spherical mean value property states that the average value of a function over a sphere is equal to its value in the center and is only valid for harmonic functions. Due to this, harmonic functions are preserved when convolved with non-negative, radially symmetric, normalized kernel functions. The SHARP algorithm convolves the total field with a spherical kernel, only the local field remains [48]:

$$B_{local} \quad (\delta \quad \rho) * {}^{1} (\delta \quad \rho) * B_{total} \tag{2.13}$$

Here, $(\delta - \rho)$ is the SMV kernel that consists of a unit impulse δ (Dirac distribution) at the center of a numerically rendered normalized sphere and the sphere function ρ [51]. The asterisks, $*$ and $*^{-1}$, symbolize a 3D convolution and deconvolution. A binary mask defines the ROI in that the kernel is applied. In practice the convolutions are performed in Fourier Space [52] and the equation can be solved by truncated singular value decomposition [27,47].

At the boundary of the ROI the SMV kernel incorporates non-harmonic parts from outside of the defined ROI and violates the SMV theorem [2], and creates artifacts at the boundary. An eroded mask can help to overcome this problem but leaves out the eroded space. VSHARP varies the size of the SVM kernel to alleviate this problem [53]. Small SMV kernel radius allows the kernel center to approach the ROI on the boundary and minimizes eroded spaces.

2.2.5.2 Projection onto Dipole Field (PDF)

According to Liu et al. [26] magnetic fields of a dipole outside of the ROI is approximately orthogonal to the local field. By optimization, the PDF method seeks the susceptibility distribution outside of the ROI that fits best the background field inside the ROI [47]. By doing so, the background field can be modelled and subtracted from the total field. However, PDF may not remove field perturbations that are not caused by susceptibility (e.g. eddy currents) and tends to overfitting. Furthermore, as described in Section 2.2.6 a single field perturbation can be based on many different distributions (ill-posed problem) and due to this cannot be solved unambiguously. However, an advantage towards the SHARP and VSHARP algorithms is that the whole ROI is processed without any erosion at the borders.

2.2.6 The inverse Problem of Dipole Inversion

The inverse step of calculating a susceptibility distribution χ from a given local field perturbation δ_B is referred to as dipole inversion. The inverse problem can be solved formally by rearranging equation (2.6) to:

$$\chi(k) \quad \delta_B(k)/D(k) \tag{2.14}$$

However, this step is ill-posed as:

$$D(k) \quad 0, if\ k_x^2 + k_y^2 \quad 2\,k_z^2 \tag{2.15}$$

$$D(k) \quad \frac{1}{3} \quad \frac{k_z^2}{3k_z^2} \quad \frac{1}{3} \quad \frac{1}{3} \quad 0 \tag{2.16}$$

In these cases, a division $\delta_B(k)\ /D(k)$ is not possible. These cases form two cone surfaces at the so-called magic angle of 54.7° relative to B_0 (see Figure 12, iii). On the cone surface the kernel is zero and cannot be applied. The inverse problem can also be expressed in this way: As a certain field distribution can have various susceptibility distributions (which differ in the zero-cone) the problem of finding the sought susceptibility distribution is underdetermined.

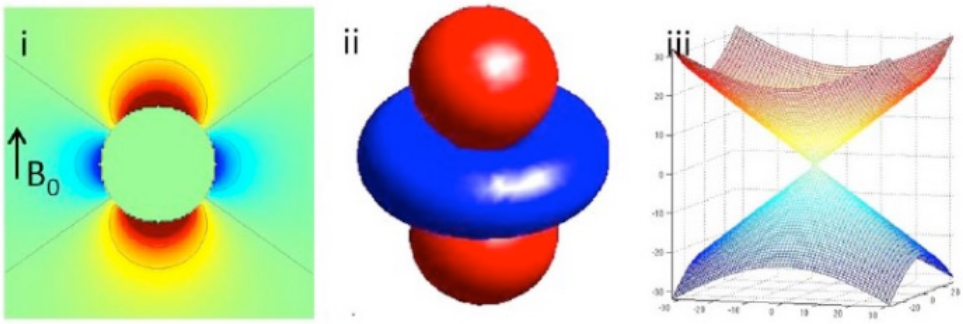

F gure 12: ( ) d po e f e d of a spher ca suscept b ty source n spat a space n 2D ( ) un t d po e kerne surface contour n spat a space ( ) -posed zero cones of the kerne n k-space. Source: [54]

To overcome the ill-conditioned dipole inversion problem, different methods are available. The following section provides a brief overview of methods and their limitations.

Calculation of Susceptibility through Multiple Orientation Sampling (COSMOS) [23] uses data of different positions of the patient's head to make the problem over-determined. However, this method requires several data acquisitions that associate with movement artifacts, extended scan time and practically difficult to realize head positions.

The truncated k-space division (TKD) [22] uses data from only one orientation during data acquisition. To calculate the susceptibility distribution $\tilde{\chi}(k)$, kernel $D(k)$ is set to $sign\big(D(k)\big) * t$ if the kernel is lower than a certain threshold t:

$$\widetilde{D}(k) \quad \begin{cases} D(k), & |D(k)| > t \\ sign\big(D(k)\big) * t, & |D(k)| < t \end{cases} \tag{2.17}$$

$$\tilde{\chi}(k) \quad \delta_B(k) \,/\widetilde{D}(k) \tag{2.18}$$

Through TKD the dipole inversion is solved but the resulting images have streaking artifacts (see Figure 13). Further methods are regularization-based and use e.g. the magnitude image information to reconstruct a susceptibility distribution. All of them need manual chosen parameters to yield a trade of between artifacts and regularization. The most common method of this type is Morphology Enabled Dipole Inversion (MEDI) [21]. The Streaking Artifact Reduction for QSM (STAR-QSM) uses two steps to reconstruct small and large susceptibilities separately and combine them afterwards [24]. STAR-QSM avoids streaking artifacts in the resulting images and preserves sharp boundaries and details. In Figure 13, the results of different approaches are compared.

Current approaches use artificial neural networks to overcome the inverse problem [3,4]. These learn an efficient regularization during training and are specific for QSM.

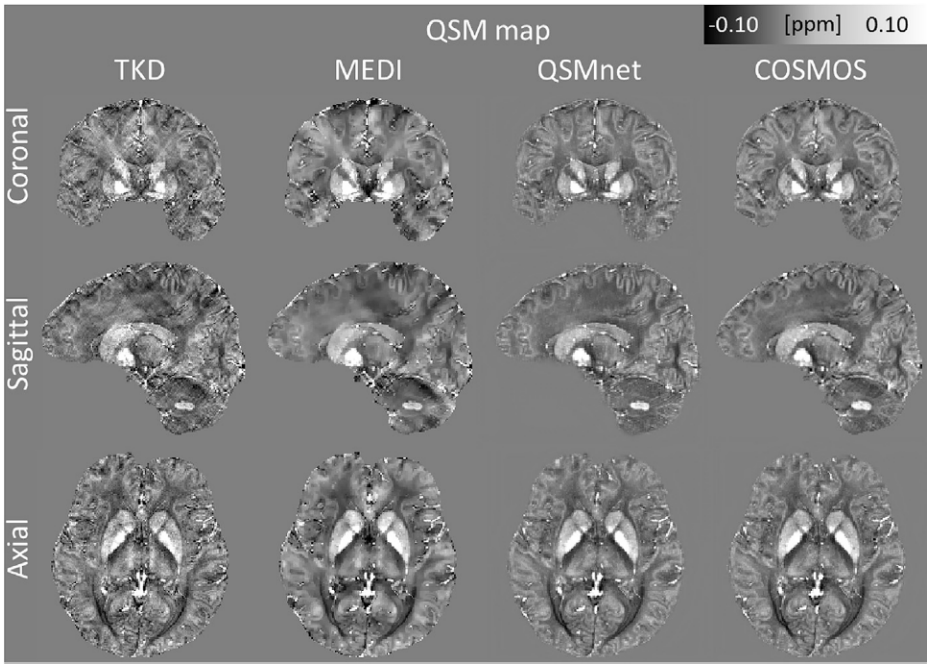

F gure 13: Compar son of d fferent methods to transfer a f e d map nto a suscept b ty d str but on. Source: QSMnet [4].

2.3 Artificial Neural Networks and Deep Learning

In this chapter, the structure and basic functionality of feedforward neural networks. In particular fully-connected (see Section 2.3.3) and convolutional neural network (CNNs) (see Section 2.3.6) are described. The focus lies on CNNs as they are widely used in Deep Learning for image processing and image recognition, following recent results [55] and implementations in this field [3,56 58]. Section 2.3.8 gives an outlook on the network structure that inspired the network architecture used in this thesis.

2.3.1 Orientation of Deep Learning in the Field of Machine Learning

In the area of artificial intelligence, machine learning subsumes a collection of algorithms categorized into unsupervised learning, supervised learning and reinforcement learning (see Figure 14) [59]. In supervised learning that is used in this thesis the algorithm trains on input output pairs and learns a function to map from input to output [59].

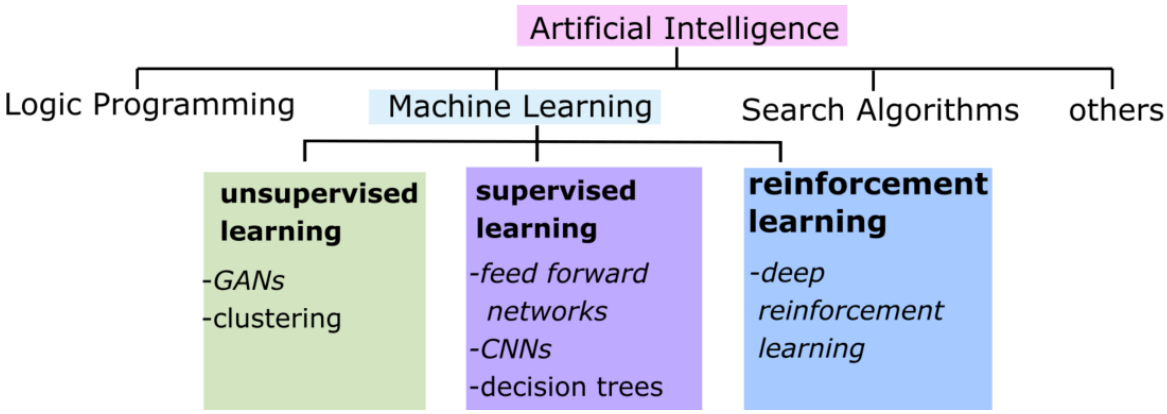

F gure 14: A br ef overv ew of Deep Learn ng a gor thms n the context of mach ne earn ng and art f c a nte gence. Deep Learn ng a gor thms are n ta c font.

Deep Learning uses complex artificial neural networks (ANN). It reaches success in areas of image or speech detection [60,61].

2.3.2 Artificial Neurons

The term artificial neuron is derived from the neurons in the brain. There, cells are connected by synapses to perform complex tasks [59]. ANNs consist of artificial neurons connected with neurons of preceding and subsequent layers (see Section 2.3.3). Figure 15 shows the structure of an artificial neuron. The neuron is connected with previous neurons which each deliver the input information x_i multiplied by a weight w_{ij}. The weights can be positive or negative and are adjusted for every neuron during learning (see Section 2.3.4). Each neuron calculates the sum of its weighted inputs $w_{ij}x_i$ and its bias b_j [59] (see Equation (2.19)).The activation function f is applied to the sum and determines the output a_j.

$$a_j \quad f\left(\sum_i (w_{ij}x_i + b_j\right) \tag{2.19}$$

The output a_j serves as input x_i for subsequent artificial neurons [59].

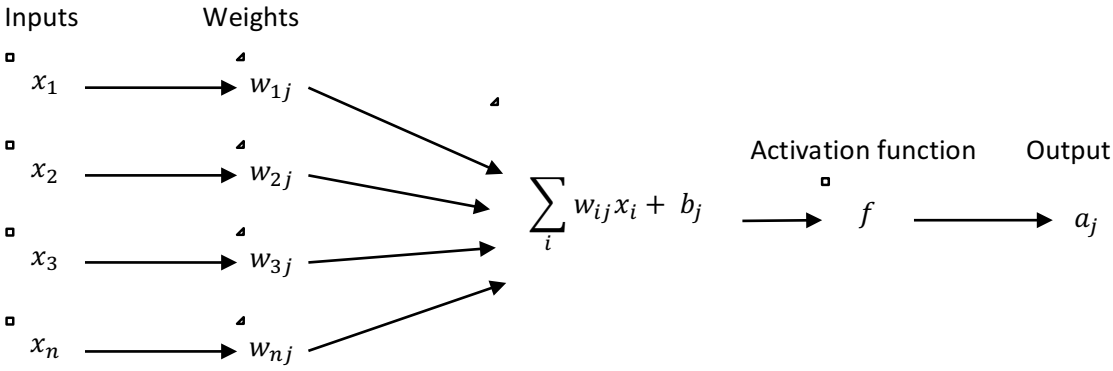

F gure 15: Art f c a neuron j w th ts nputs and output a_j.

With the non-linear property of the activation functions, ANNs consisting of at least one hidden layer are able to handle non-linearity in data (see Section 2.3.3) [59,62]. Through this, ANNS can approximate any function. The ReLu function is often used as activation function in the field of image processing as it enables CNNs to be trained more efficiently [63] compared to activation functions as sigmoid or tanh. The ReLu function thresholds the output of a neuron at zero for values below 0 and is linear for positive values [63]:

$$f(x) \quad max(0, x) \tag{2.20}$$

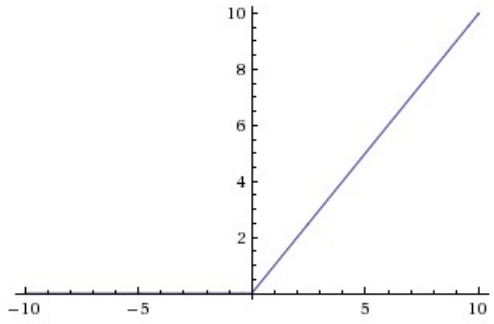

F gure 16: Rect f ed L near Un t (ReLu). Source: [64]

2.3.3 Fully-Connected Networks

In general, ANNs are organized in layers that consist of several artificial neurons. In a fully connected layer, each neuron of the layer is connected with all neurons of the previous and the subsequent layer (see Figure 17).

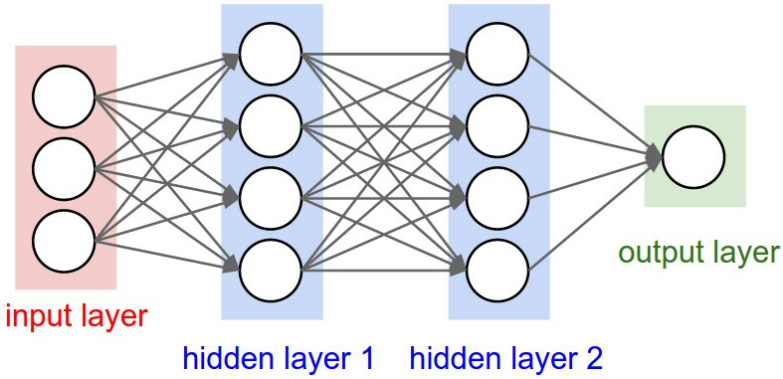

F gure 17: A fu y connected neura network w th two ayers. Source: [64]

The network in Figure 17 consists of two fully connected layers (hidden layer 1 and hidden layer 2) next to input and output. Each circle in the hidden layers and the output layer represents a neuron. The connecting arrows symbolize the weighted connections $w_{ij}x_i$. In fully connected layers (so called dense layers), each neuron is connected to all neurons of the neighboring layers and due to this has multiple learnable weights. All neurons have next to the weighted connection w a learnable bias b. In total, the network in Figure 17 consists of 32 weights and 9 biases that form together 41 learnable parameters.

The Cybenko Theorem gives mathematical proof that a network with only one hidden layer can approximate any continuous function with a sufficient number of neurons [62]. In practice, numerous layers are organized in a hierarchical structure to achieve a more efficient learning process (see Section 2.3.6).

2.3.4 Optimization

Essential parts of the iterative learning process are the calculation of a loss function (see Section 2.3.5) and the parameter optimization. Optimization adjusts the parameters (weights and biases) of the network in a way to minimize a certain loss function. For ANNs with just one learnable weight this process is visualized in Figure 18.

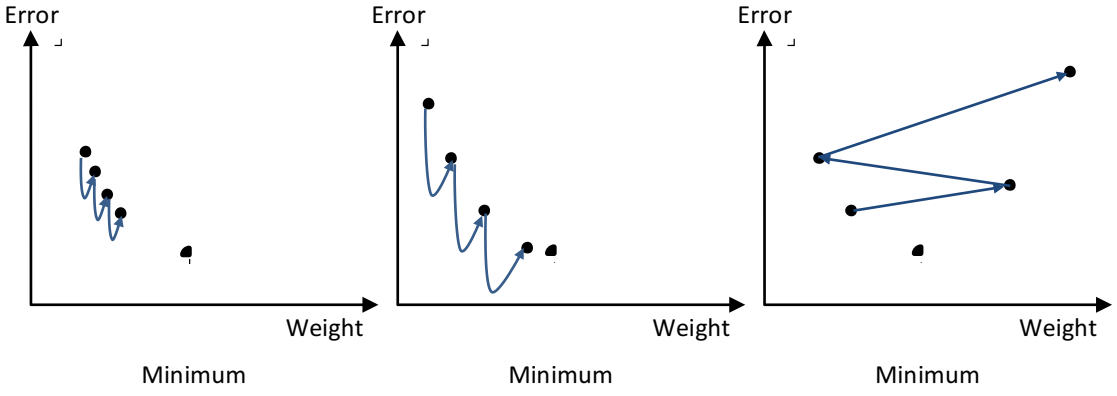

F gure 18: Opt m zat on for a one-d mens ona prob em: Each terat on the we ghts are changed by a def ned step s ze to decrease the oss. If the step s ze s too arge, the opt ma we ght can be m ssed – f the step s ze s very sma , the t me for tra n ng w ncrease. The a m of the opt m zat on s to adjust the we ght to reach the g oba m n mum. Source: [65]

While the shift on the x-axis in Figure 18 represents the learning rate, the gradient determines the shift of the error. For ANN with thousands of learnable parameters the process is a high-dimensional landscape. Stochastic Gradient Descent (SGD) is an iterative algorithm for solving the optimization with large-scale datasets [66,67]. As it uses randomly picked training samples for parameter estimation in each iteration, it is simplification to the gradient descent algorithm and is also suitable for online learning [66].

For optimization problems with high-dimensional parameter spaces and/or large datasets, the Adam algorithm shows to be robust and computationally efficient [68]. The algorithm considers the exponentially decaying average of past gradients to avoid getting stuck in local minima and to obtain a fast convergence rate [68].

Apart from the optimization algorithm, the parameter adjustment is influenced by the amount of data used. Instead of using all data at once a certain (mini) batch size determines how much data out of the available data is used to calculate the loss and the gradients in every iteration. To use gradient descent the derivatives of the loss (see Section 2.3.5) with respect to the current parameters are needed. As the loss function is calculated at the output of the network, the information has to be transferred from the output back through the whole network. This happens by using backpropagation that uses the chain rule of derivatives [69].

2.3.5 Loss Function

In supervised learning, the loss function compares in every iteration i the created output (prediction) y_i with the expected output label y'_i (also called ground truth). In regression networks (as in this thesis), a common loss function is the mean squared error (MSE) loss:

$$MSE\ loss(y, y') \quad \frac{\sum_{i=1}^{N}(y_i \quad y'_i)^2}{N} \tag{2.21}$$

In the case of images processing, N is the number of pixels of the image while y_i and y'_i are the pixel values of the output and the label image. The closer to zero the MSE, the better is the result. Classification problems use logarithmic algorithms like Cross-entropy [65].

2.3.6 Convolutional Neural Networks in Image Processing

Convolutional neural Networks (CNNs) can deal with spatial data like images and are state of the art for image recognition and processing [55]. In comparison to fully connected networks, CNNs can reduce the number of parameters and process larger images. By using a receptive field, the neurons inside a layer are connected only to a small amount of the adjacent layers, so they are arranged in depth (see Figure 19) [70].

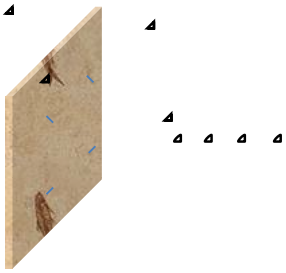

F gure 19: Neurons a ong the depth ax s of a s ng e convo ut ona ayer correspond on y to a sma excerpt of the nput mage.

These layers are convolutional layers and together with ReLu functions (see Section 2.3.2), pooling layers and fully connected layers form the base for a convolutional neural network (see Figure 20).

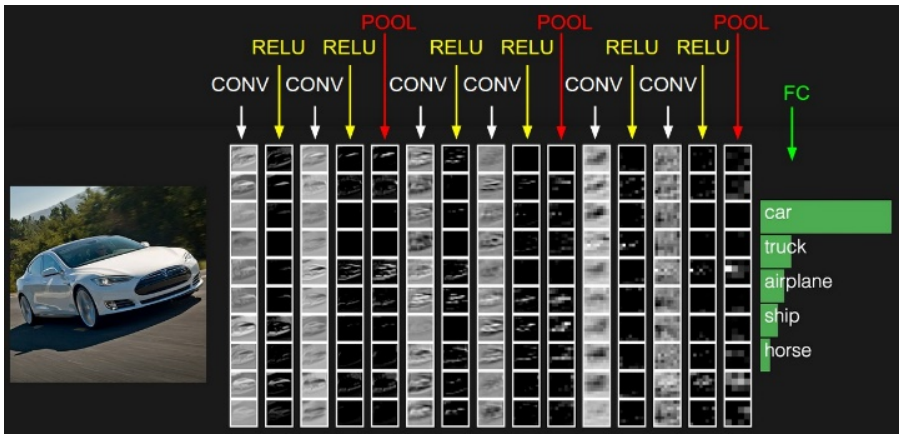

F gure 20: Shows the h gh- eve arch tecture of a CNN for mage c ass f cat on. The nput s an RGB mage w th d men- s ons he ght and w dth and 3 channe s (red, green and b ue). The nput passes severa convo ut ona ayers w th ReLu funct ons and Poo ng ayers. The ast ayer s a fu y connected ayer, that merges the data to a 1x1xn vector that can d st ngu sh n c asses and determ nes the probab ty for each c ass. Source: [64]

A convolutional layer consists of several filters that form filter matrices. The filters have a kernel size (e.g. 3^3). Each filter slides through every pixel of the input image and creates a filtered output image that is called feature channel, activation map or filter map (see Figure 21). The filter matrix consists of weights that are learned during training with images (see Section 2.3.4). This way, a network will have different filters depending on the training data.

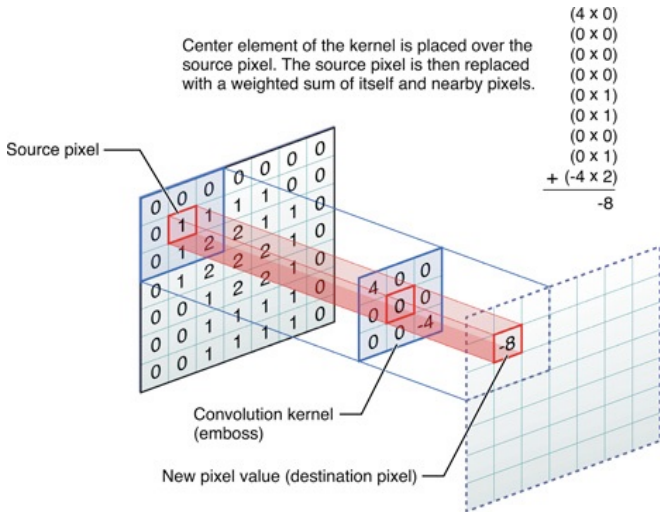

F gure 21: A f ter kerne of s ze 3x3 s des over an one-d mens ona grey-va ue mage and creates a feature map. The source p xe s and the convo ut ona kerne form dot products for each p xe . The new p xe va ue s the sum of these dot products. Source: [71]

As a single filter is applied on the whole input, so the parameters are shared. Due to its filters, the network processes small patches of the image. As the parameters are shared, the filters are not locally fixed and can recognize features if they are translated (see Figure 22).

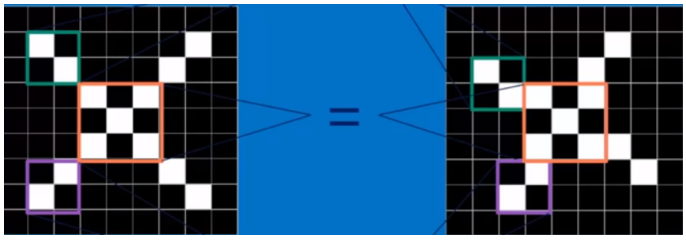

F gure 22: App y ng the shared f ters, a ows to recogn ze a cross even f not a p xe s match. Source: [72]

A layer can consist of several filter kernels and each of them produces a feature channel as output. They are stacked along the depth dimension. In the subsequent convolutional layer, again the same procedure applies. Thus, the number of feature channel outputs increases. To keep the amount of data manageable, the images are subsampled: pooling layers (see Figure 23) or a stride value of 2 for the filter decrease the size of the resulting feature channels (see Figure 24).

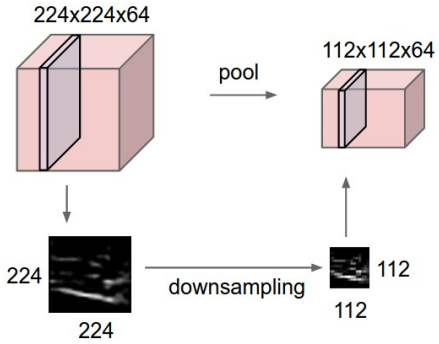

F gure 23: A poo ng ayer that s used for downsamp ng. Source: [64]

The stride determines the sliding step of the filter over the input image.

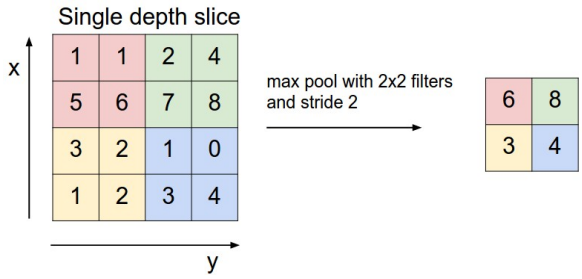

F gure 24: Max Poo ng funct on: On y the max ma va ue n the area of 2x2 s kept. Through th s, the mage s downsamp ed. Source: [64]

As shown in Figure 20 CNNs for classification tasks end with fully connected layers to output a certain class. Networks for segmentation [73] and the network mentioned in this thesis (see Section 3.1) to solve the ill-posed problem in QSM use transposed convolutional layers to create images as output.

2.3.7 Transposed Convolutional Layer

Max-pooling layers, stride values (>1) and omitting zero-padding decreases the size of the output in the network (downsampling). To increase the size of the output, in terms of upsampling, transposed convolutional layers (also called deconvolutional layers) are used. Referring to image processing, an input pixel (2-dimensional space) or voxel (3-dimensional space) is dotwise multiplied by a filter matrix to create an output (see Figure 25). Overlapping outputs of adjacent pixels are summed up.

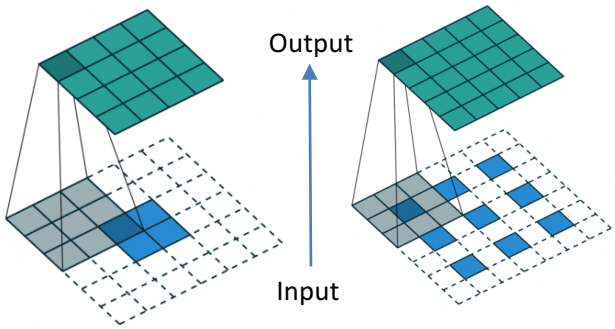

F gure 25: The eft mage shows a deconvo ut on w th f ter s ze 3x3, no padd ng and no str de. The r ght s de shows a deconvo ut on w th f ter s ze 3x3, padd ng and str des. Source: [74].

2.3.8 The U-net

The U-net is the base architecture for the network used in this thesis. Originally, it was invented to perform binary segmentation tasks on 2-dimensional image data [5]. The left side of the network consists of convolutional and max-pooling layers. While the convolutional layers extract features of the input, the max-pooling layers (red arrows in Figure 26) decrease the size of the input to keep the number of parameters (induced by the increasing number of output channels) manageable. The convolution layers use padding to keep the output size equal to the input size in every network level. The right part uses transposed convolutional layers (green arrows in Figure 26) to upsample

the data. Skip connections (grey copy and crop arrows in Figure 26) help to preserve the position of the final output pixels [5].

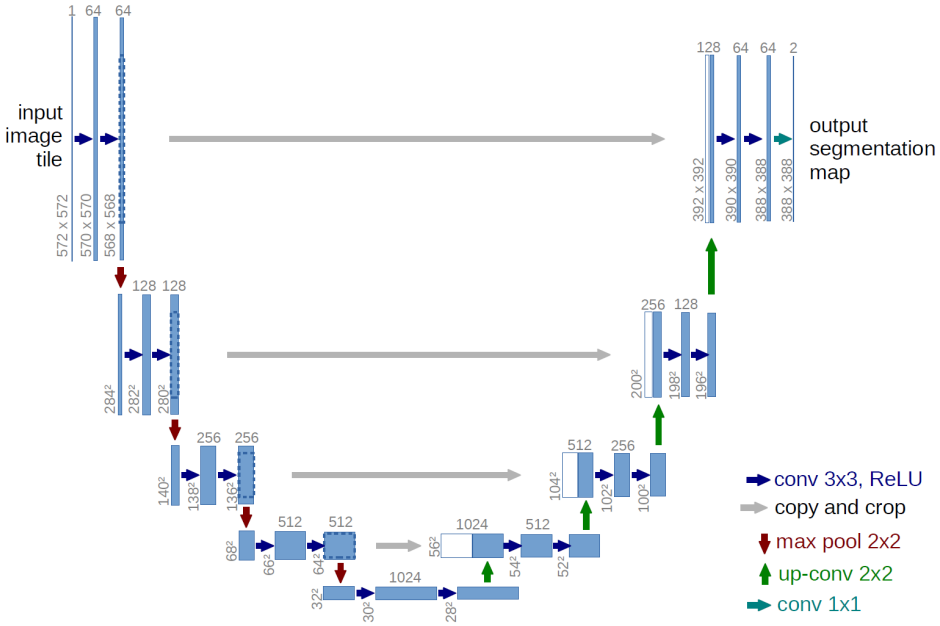

F gure 26: Arch tecture of the U-net: The arrows descr be the operat ons n the correspond ng ayers, the grey numbers on the top of each ayer descr be the number of channe s, the vert ca numbers descr be the he ght and w dth of the data. Source: [5]

Beyond the base architecture, several enhancements exist that solve further segmentation tasks [73], regression tasks [75] or can handle 3-dimensional data[76].

2.3.9 Challenges in Deep Learning

In deep learning, the collection of training data and the choice of an adequate ANN architecture and its hyperparameters are challenging tasks. A major problem is to acquire the amount and quality of required data. The data might be not suitable for the purpose to be solved in terms of noisiness or erroneous data and the usage of irrelevant data, which leads to inaccurate predictions [65]. The available data is split into train and validation data. Both are evaluated during training. However, only the loss of the train data (train loss) is used to adjust the weights of the ANN. If the model predicts with high accuracy on the train data but with poor accuracy on validation data, this is a sign that the model loses its ability to generalize, which is called overfitting (see Figure 27).

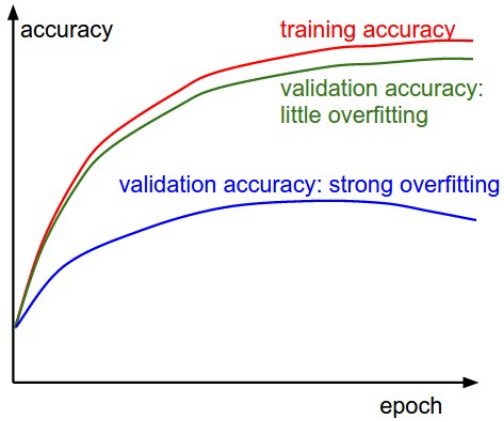

Figure 27: The accuracy is a loss function that increases while improving. In overfitting, the validation loss is worse than the training loss. Strong overfitting even shows a deteriorating validation loss. Source: [64]

The opposite of overfitting is underfitting, where the model of the ANN might be too simple to match a sought complex function. A possible way to avoid overfitting is to increase the amount of data or to adjust the dropout rate [77]. Based on the dropout rate, neurons are deactivated with a certain probability.

The dropout rate is a so-called hyperparameter. Hyperparameters are in contrast to the weight parameters fixed during training. In the case of convolutional layers these are the number of output channels (number of filters per layer), the filter size, stride size and the use of zero-padding to keep the original image size (see Section 2.3.6). For networks in general, these are among others the learning rate, dropout rate and depending on the used optimizer further parameters as momentum.

3 Material and Methods

The problem of finding the susceptibility distribution out of a given field map is an image-to-image machine learning problem. The same applies for the task of removing the background field in an image. Section 3.1 describes how the U-net architecture (see Section 2.3.8) was adapted to process 3D data and solve the image-to-image problems. In Section 3.3, the loss functions that were used for training and validation of the models are presented.

Section 3.4 and Section 3.5 describe the steps of creating datasets for the specific problems of dipole inversion, background field removal or both steps in one. To evaluate the ANNs on more complex and brain-like structures a numerical brain phantom was used (see Section 3.7). To test the model on real in-vivo data, an MRI scan of a healthy volunteer was acquired. All details to this scan can be found in Section 3.8. Finally, a brief overview of the used tools and libraries is given in Section 3.9.

3.1 DeepQSM Baseline Model

Based on the work of Rasmussen et al. [3] who created the neural network DeepQSM, the same architecture is used in this thesis for further investigations in dipole inversion and background field removal. The implemented neural network is a modification of the neural network 'U-Net-Pytorch-0.4', that is originally used for semantic segmentation purposes (see Section 2.3.8)[78].

According to Rasmussen et al. [3], the feature channels are reduced to accomplish a more efficient processing of three-dimensional data.

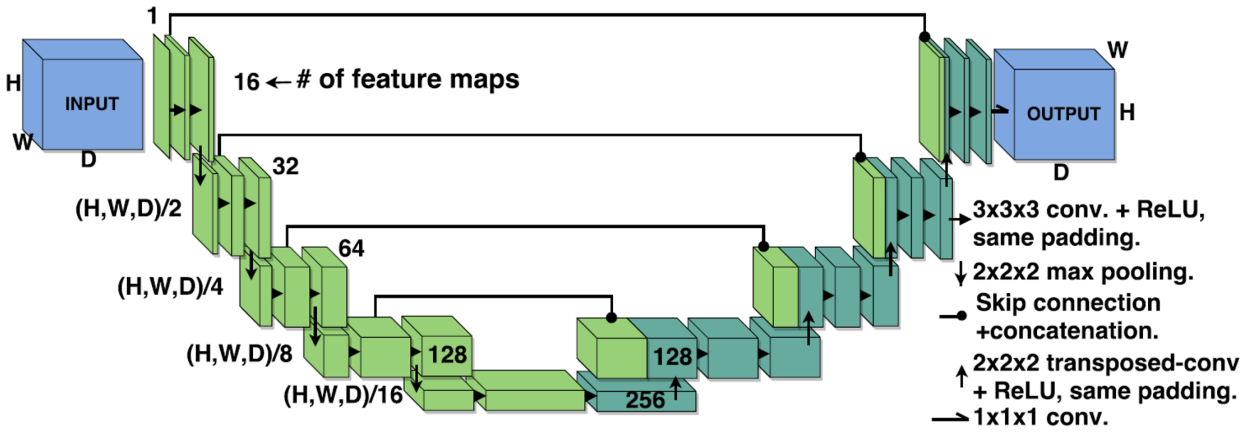

F gure 28: Arch tecture of the DeepQSM ANN w th the used ayers, act vat on funct ons and number of f ters. Source: [3]

While the 'U-Net-Pytorch-0.4' is a network for semantic segmentation, the DeepQSM network is a regression network that solves the ill-posed field-to-source inversion. Semantic segmentation can be seen as a classification problem that distinguishes if certain pixels in an image belong to a certain class or not. Due to this, it uses a Softmax function [65] at the end of its model: The function maps the output into probabilities for the different label classes and the class with the highest probability

is chosen for the respective pixel. In case of the DeepQSM network the Softmax function is not necessary and the model creates an image self-contained. Next to the Softmax function, the ReLu function (see Section 2.3.2) in the last layer was removed. This guarantees that ANN can also output negative values.

As DeepQSM does not deal with classification categories, the loss function Cross-entropy was replaced by the Mean Squared Error (MSE) loss function. During training, the function measures the average of all squared voxel differences between created network output image y_i and label image y_i'.

To optimize the weights during training the Adam optimizer (see Section 2.3.4) with default configurations (learning rate=0.001, β_1=0.9, β_2=0.99) was used. To avoid overfitting a dropout of 10% was used. The trained network can process images with an image size divisible by 16, greater/equal than 48^3 and creates output images with the same size as the input. This neural network with the described hyperparameter settings is used as benchmark for further modified versions and hyperparameter combinations (Section 4.1.2).

The ANN for dipole inversion used images with a size of 48^3 during training. In this case, a batchsize of 32 and a number of 20500 training steps was chosen according to Rasmussen et al. [3]. For the problem of background field removal and in the combination with dipole inversion, images of size 128^3 voxel were used. As the computation of larger images requires more memory, the batch size was reduced to two input and label images. Furthermore, the number of training files was set to 1000 files. The difference in the architecture for the background field removal model and the model that performs both QSM steps, was an additional input channel for mask images (see Section 3.5, Section 3.6). However, next to the DeepQSM architecture a deeper architecture was built to improve the performance of dipole inversion (see Section 3.2).

3.2 Deeper Architecture

A tested model variation in Section 4.1.2 used a network architecture with a larger receptive field. By a larger receptive field the network can take into account information of a large image section. A neuron in the first layer is connected to more neurons in the following layers and the ANN can recognize more complex visual patters in the image. The receptive field is realized by a further level of convolutions with max-pooling and deconvolution. Figure 29: Architecture of the deeper architecture and an enlarged receptive field. Adapted from [3] shows the architecture with an additional level with 16 feature maps.

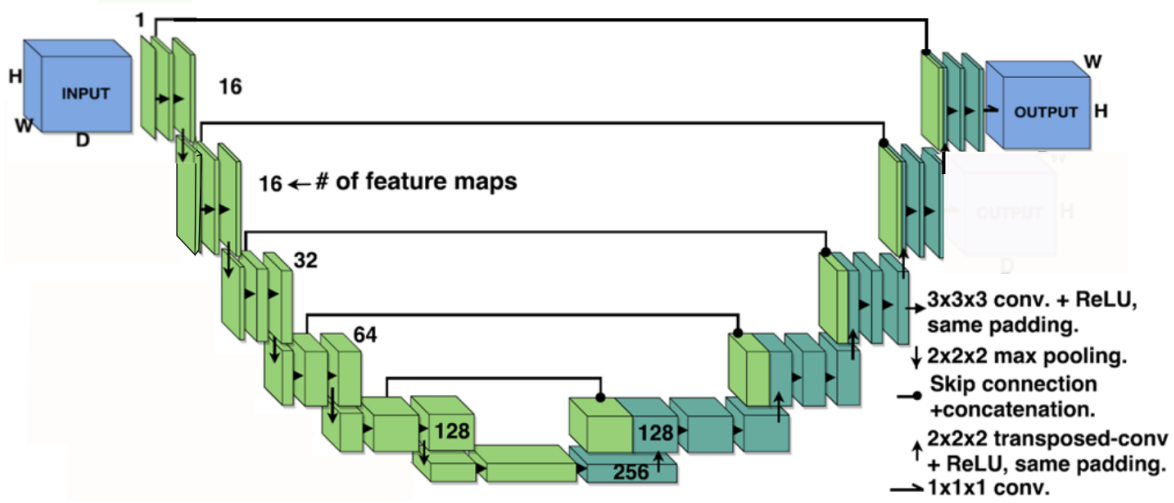

F gure 29: Arch tecture of the deeper arch tecture and an en arged recept ve f e d. Adapted from [3]

The image size is divided by two in each of the five layers. Due to this, the input image has to be dividable by 2^5 instead of 2^4. The image size must be at least 96 voxels, so the image in the lowest level can be still filtered by the 3^3 kernel.

3.3 Evaluation Criteria and Loss Functions

Inspired by QSMnet [4], for different trainings the MSE training loss (described in Section 3.3.1) was replaced by a Mean Absolute Error (MAE) combined with an image gradient loss to sharpen object edges. Furthermore, several validation losses were used to evaluate the output of the network for non-training data.

In case of masked images (see Section 4.2, Section 4.3) the sum of pixel losses was divided by the number of pixels where the mask is True instead of the number of all pixels in the image (see Section 3.5.1).

3.3.1 Weighted Image Gradient Loss

Similar to the QSMnet Mathieu et al. [79], an additional loss that measures the image gradient was added to sharpen object edges:

$$Image\ Gradient\ (y', y) \quad ||\nabla y'|_x \quad |\nabla y|_x| + + \left||\nabla y'|_y \quad |\nabla y|_y\right| + \ ||\nabla y'|_z \quad |\nabla y|_z| \tag{3.22}$$

Here, the image gradients ∇ of the output y and the label image y' are compared in x, y and z direction. In combination with the MAE loss and a constant weight, it forms the total loss that was used by different trainings:

$$Weighted\ Gradient\ Loss \quad MAE + weight \cdot Image\ Gradient\ Loss \tag{3.23}$$

The MAE is defined as follows, where $y_i - y_i'$ is the difference between output y' and label y_i:

$$MAE \quad \frac{1}{n}\sum_{i=1}^{n}|Y_i \quad Y_i'| \tag{3.24}$$

3.3.2 Linear Regression Intercept and Slope

The voxel matrixes of output and label images were flattened to obtain two one-dimensional data series. These vectors were used as data points for a least-square regression. If the images are the same, a function $\hat{y}$ with a slope of one and an intercept of zero is fitted.

The slope described the relation between output and label and if the values of the reconstructed images are in the same range as the ones of the label. Both slope and intercept were calculated but only the slope was used to compare the results:

$$\hat{y} \quad \hat{y}(x) \quad b_0 + b_1 x \quad intercept + slope \cdot x \tag{3.25}$$

3.3.3 Structural Similarity (SSIM)

The structural Similarity Index (SSIM) [80] uses patches of two digital images to compare their similarity. SSIM was invented to create a measurement that is rather comparable with the visual perception of humans than MSE is. In order to do so, patches of image x and image y are examined for their luminance (l), contrast (C) and structure (s).

$$l(x,y) \quad \frac{2\mu_x\mu_y + C_1}{\mu_x^2 + \mu_y^2 + C_1} \tag{3.26}$$

$$c(x,y) \quad \frac{2\sigma_x\sigma_y + C_2}{\sigma_x^2 + \sigma_y^2 + C_2} \tag{3.27}$$

$$s(x,y) \quad \frac{\sigma_{xy} + C_3}{\sigma_x\sigma_y + C_3} \tag{3.28}$$

Here, the luminance compares the means μ_x and μ_y, the contrast compares the standard deviations σ_x and σ_y, and the structure measures the correlation of both patches. C_1, $C_2$and C_3 are positive constants that stabilize the terms in case of a weak denominator. In this thesis $C_3 = \frac{C_2}{2}$ and luminance, contrast and structure are multiplied equally weighted, which yields the structural similarity index:

$$SSIM(x,y) \quad \frac{(2\mu_x\mu_y + C_1)(2\sigma_{xy} + C_2)}{(\mu_x^2 + \mu_y^2 + C_1)(\sigma_x^2 + \sigma_y^2 + C_2)} \tag{3.29}$$

The size of the patches is defined by the window size. For all calculations in this thesis, a window size of five was used. For $C_1$and C_2 the default settings were chosen.

3.3.4 Root-Mean-Squared Error

The root-mean squared error (RMSE) that is also called root-mean squared deviation is the root of the mean squared error.

$$RMSE\ loss(y, y') = \sqrt{\frac{\sum_{i=1}^{N}(y_i - y'_i)^2}{N}}$$

RMSE is a measure of accuracy that is always non-negative and sensitive to outliers. As it depends on the scale of the measured values, results can only be compared if they use the same underlying dataset.

3.4 Data Generation for the Dipole Inversion Model

This section describes the dataset that was used to train an ANN that converts an input image of a local field to the corresponding image of its susceptibility map. To create the required amount of training data, a data generation technique for virtual data inspired by the paper of Rasmussen et al. [3] was used. Voxel images with a size of 48^3 each containing 100 three-dimensional geometric forms like spheres, cuboids, ellipsoids and cylinders were generated. Size, voxel intensity, rotation angle and translation in space were chosen randomly for each object in the images. Table 2 gives an overview over the sizes of the objects. The probability of generation was the same for each type of geometric object.

Geometric Objects	Radius of Spheres	Length of Cuboids	Radius of Cylinders	Length of Cylinders	Radius of Ellipsoids
Lower limit	0.1	0.1	1	1	0.1
Upper limit	15	20	20	40	20

Tab e 2: S ze of the geometr c objects n the dataset for d po e nvers on w th s ze 48^3 voxe .

Affine transformations were used to rotate and shift the objects and realize different orientations. All objects were interpolated (first order spline interpolation to prevent ringing artifacts). The created images constitute the set of virtual data for training, validation and evaluation purposes. They are also referred to as ground truth in the following chapter about dipole inversion. In terms of MRI, the images represent the susceptibility map (or susceptibility distribution) that was used as label data during training. A susceptibility map shows the tissue specific values for magnetic susceptibility by its value. The objects were randomly assigned susceptibility values between -0.5 and 0.5. In case of superimposed objects, the corresponding values cumulated.

While the transformation of a measured field perturbation to the susceptibility map is an inverse problem, the susceptibility map to local field perturbation can be obtained by a simple convolution in Fourier space (see Section 2.2.2). Due to this, it is possible to create training data to overcome the ill-posed dipole inversion. As explained in Figure 30 each ground truth image was convolved with the dipole kernel in k-space to obtain the corresponding forward solution image. The forward solution symbolizes the corresponding measured local field of the susceptibility map. For training and validation, the forward solution served as input while the ground truth served as label (see Figure 30).

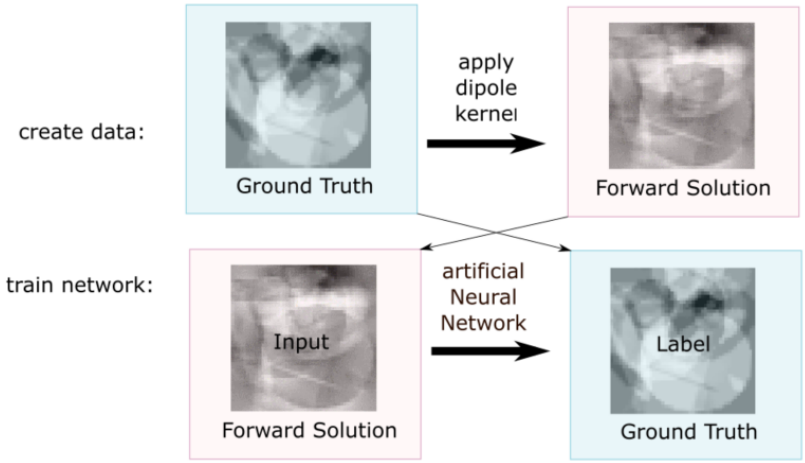

F gure 30: Overv ew of data creat on and tra n ng: The ground truth was convo ved w th the d po e kerne to obta n the forward so ut on. The ground truth – represent ng the suscept b ty map – served as abe wh e the forward so ut on – represent ng the f e d perturbat on –served as nput wh e tra n ng. Through th s, the ANN earns to overcome the - posed d po e nvers on and maps a oca f e d to ts correspond ng suscept b ty map.

Finally, the image values of the images were standardized. To do so the standard deviation of the values in the susceptibility map was calculated excluding values of zero. Zeros were excluded because they form the background of the image. The ground truth was divided by its standard deviation and multiplied with 0.2. The corresponding forward solution used the same scaling factor. Figure 31 shows an example of the final distribution of both a ground truth and a forward solution image. Due to the random generation of the data, the distribution can differ from image to image. However, all ground truth images and all forward solution images had the same standard deviation. To show optimal performance the trained ANN should only be applied to input data with values in the range of the forward solution images. Due to this, it is important that the dataset represents the values of the in-vivo data that is tested later.

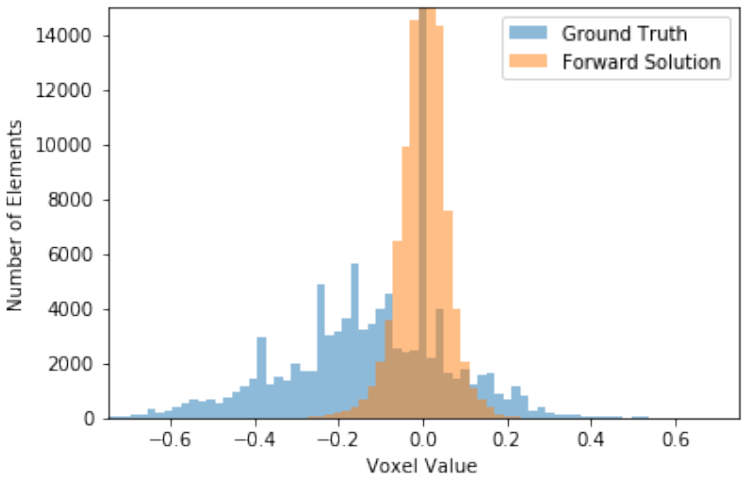

F gure 31: : H stogram of an exemp ary ground truth and ts correspond ng forward so ut on mage.

In total, 71,400 pairs of ground truth and forward solution images were created and split into train data (70,400 ground truth - forward solution pairs) and validation data (1,000 ground truth forward solution pairs).

3.5 Data Generation for the Background Field Removal Model

Background field removal (BFR) describes the process of removing field inhomogeneities caused by susceptibility sources outside of the ROI and remaining only the local field that shows field perturbations of susceptibilities inside the ROI (see Section 2.2.5). The ANN for background field removal used almost the same DeepQSM architecture as described in Section 3.1. However, the ANN for BFR used images with size of 128^3 instead of 48^3 voxel and uses two concatenated input images as input channel. By using larger images, the network could learn to remove fields of sources that are not in the receptive field of the ANN. The input are masked images containing total fields concatenated with the respective images of the applied masks. Using masked images, the ANN learned to determine the ROI of the corresponding input image. As label served the corresponding local field image. The functionality is shown in Figure 32.

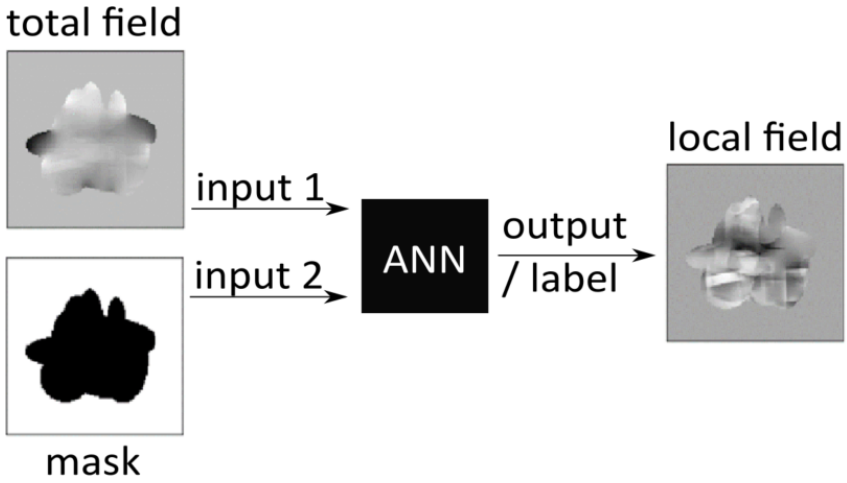

F gure 32: Overv ew of ANN for BFR. The background f e d s removed from the tota f e d. Th s way on y the oca f e d rema ns. The mask determ nes the ROI. A d po e nvers on s not part of the tra n ng.

In the following section, the creation of data for the ANNs trained for background field removal is explained. The created datasets were also used for the ANNs that perform both background field removal and dipole inversion. To optimize the results three different datasets were tested for training:

1. Dataset Offset (see Section 3.5.2)
2. Dataset External Susceptibilty sources χ (see Section 3.5.3)
3. Dataset Stronger External χ (see Section 3.5.4)

The datasets differ in the origin of their background field and due to this in their standard deviation of values. Especially the standard deviation of the total field differs as the strength of the corresponding background field varies. The creation of the three datasets is explained in the following sections.

3.5.1 Mask, Susceptibility Map and Local Field

To create random masks, the original position of random objects was limited to the area around the image center and the value set to only positive ones. Due to the number of objects, the area in the center was covered completely with objects. This area was assigned to True while the area with no objects was assigned to False (see Figure 33).

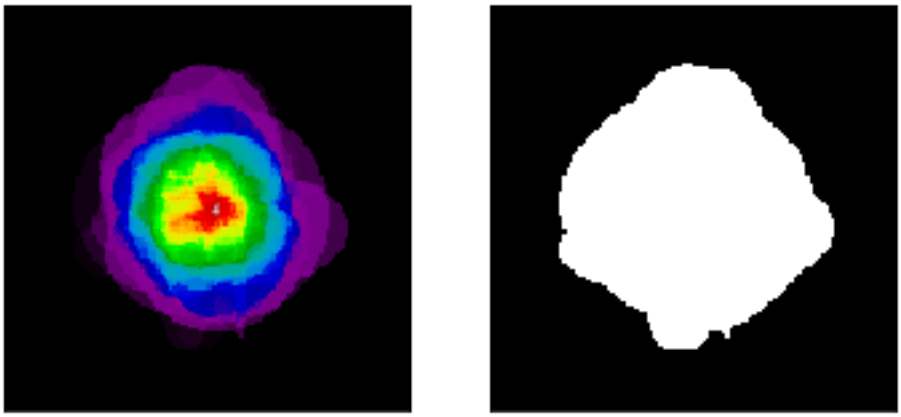

F gure 33: Exemp ary mask: Left: Var ous objects cover the mage center. A d fferent co ormap was chosen to better d fferent ate between the va ues. R ght: The resu t ng mask w th va ues of 1 (True) n the center and 0 (Fa se) n the area around.

The images were generated in the same manner as for dipole inversion with DeepQSM (see Section 3.4) but with a size of 128^3. In comparison to the images used for dipole inversion, these images contain 500 instead of 100 objects each larger in size.

Afterwards, these images were multiplied with random mask images (shown in Figure 33). The resulting images were the ground truth labels for the ANN that should perform both background field removal and dipole inversion (see Section 3.6). In the case of the dataset created solely for BFR, these susceptibility labels were convolved with the dipole kernel to obtain the local field. The local field appeared in the ROI and outside of it. Due to this, the field map was again masked so the local field outside of the ROI was erased. All steps are visualized in Figure 34 below. This masked local field was the ground truth label for the ANN that only performs background field removal.

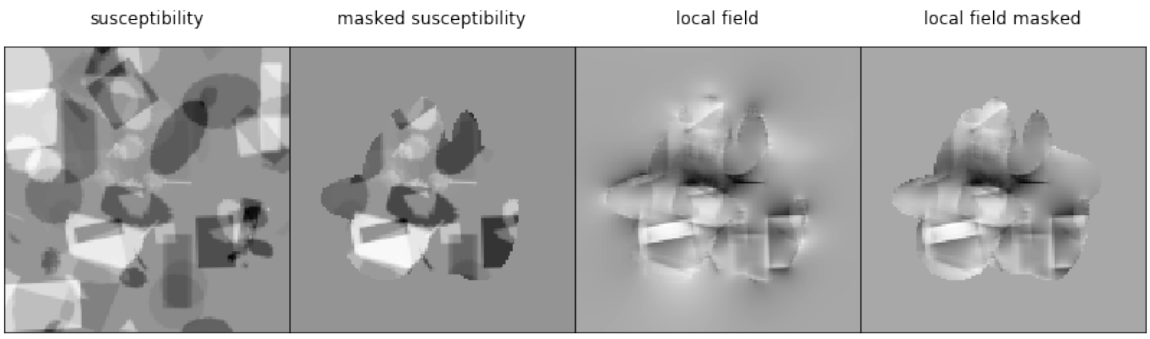

F gure 34: Steps to create a masked oca f e d map: F rst a suscept b ty map was created and masked. By a convo ut on w th the d po e kerne the oca f e d was created. F na y, the oca f e d was masked.

3.5.2 Total Field created with Offset

In this case, to the ROI of the susceptibility labels an offset of -9 was added to create the total fields. This simulated the strong susceptibility difference between tissue (susceptibilities around -9 ppm) and air (susceptibility of zero). The masked susceptibility images with an offset of -9 in the ROI towards the area outside of the ROI were convolved with the dipole kernel and were multiplied by the non-dilated masks afterwards. The created images serve as total fields with strong field perturbations produced by the high susceptibility interface between ROI and mask. The total field were the input for the training of the BFR and the BFR plus dipole inversion models (see Section 4.2, Section 4.3).

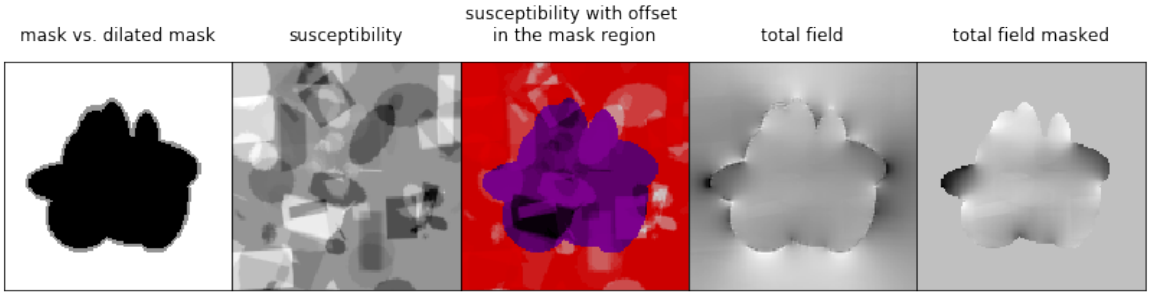

F gure 35: Creat on of tota f e d by an offset: A h gh suscept b ty change at the boundary of the ROI was s mu ated by add ng va ues of -9 to the area to the ROI n the suscept b ty map.

In total 2000 image pairs were created. 1800 were used for training and 200 for validation.

3.5.3 Total Field created with external Susceptibility Sources

While the skullcap is surrounded by air, the area below the brain is predominantly tissue with similar susceptibility. However, the paranasal sinuses form high contrasts of air-tissue interfaces. To reflect these, no offset was added to the ROI. Instead, in the area outside of the ROI strong susceptibility sources (susceptibility values of 1 5) were added to each image. For this dataset, the range of the strong external susceptibilities was between 4 ppm and 6 ppm and a radius of 5 10 voxel. The forward solution was calculated and the result was masked to keep the total field within the ROI. Furthermore, in the ROI area, cylinders with a slightly higher susceptibility (0.1 0.3) than the other objects were added. The cylinders simulated veins in the brain. In total, 1200 image pairs were created. 1000 were used for training and 200 for validation.

3.5.4 Total Field created with stronger external Susceptibility Sources

In a further dataset variation, the radius of the strong susceptibilities was enlarged to 15 20 voxel while the ROI was reduced. Furthermore, the susceptibility range was set to the range 3 ppm to 15 ppm. Thus, the created images represent strong external susceptibility sources, that cause strong fields reaching into the ROI. As they are masked afterwards, the sources are not visible and simulate a signal loss.

3.6 Data Generation for the Background Field Removal and Dipole Inversion Model

In addition to the ANN for BFR, a further model was trained that used the same architecture and input images. In contrast to the BFR model, susceptibility maps were used as labels. This way, the ANN should learn to solve BFR and dipole inversion in a single step. Figure 36 visualizes the functionality of this model.

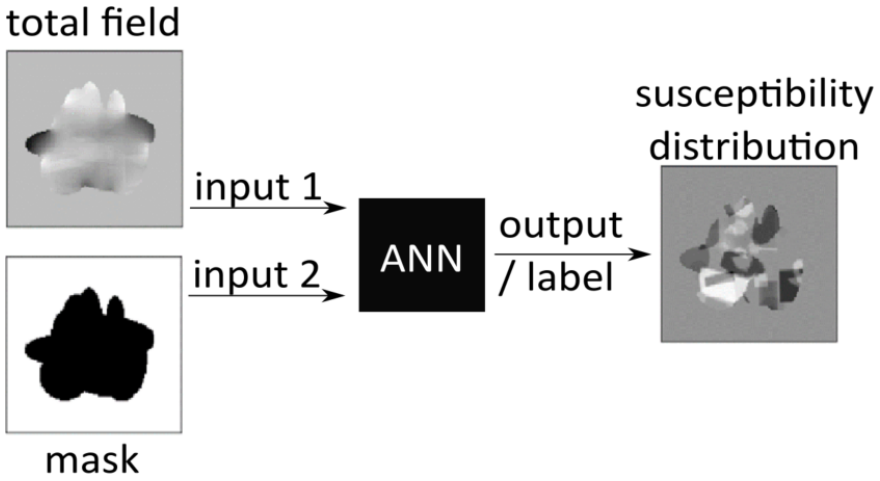

F gure 36: The ANN used the correspond ng suscept b ty map as abe . The neura network earned background f e d remova and d po e nvers on n one run Resu ts.

Similar to the BFR model, three different datasets as described in Section 3.5 were used for training.

3.7 Numerical Brain Phantom

To evaluate the model's ability to apply QSM on complex brain-like structures, a numerical brain phantom was used as input. For this, a T1-weighted MR magnitude image of a brain was acquired. Different brain regions like grey and white matter, deep matter nuclei or the corpus callosum were segmented and assigned to a theoretic susceptibility value for this region. Afterwards, the parts were added together to form a susceptibility map of a brain. The image had a size of 250x228x310 voxel. Due to the restricted memory, the image was down-sampled to a size of 128x144x176 voxel. The susceptibility map was convolved with the dipole kernel to obtain a corresponding local field map. The local field map served as input for the ANN for dipole inversion (see Section 4.1.4). To evaluate the ANN for BFR or the ANN that performs both steps in a single step, the total field images was created in a similar way as described for the synthetic data in Section 3.5. Here, the total field images were created with strong external susceptibility sources. The dataset with offset had an additional offset of 0.4 ppm. The mask that was needed for this was created by thresholding and morphologic erosion similar to the steps described in Section 3.8.

In contrast to in-vivo data, the numerical brain phantom has the advantage that the results are comparable to a ground truth. A disadvantage is that fine structures as vessels are missing and that the creation of the total field may not be comparable to the total fields in scan data. Figure 37 shows a histogram of its susceptibility map and the local field map. In contrast to the train dataset, the values of the numerical brain susceptibility map are not normally distributed.

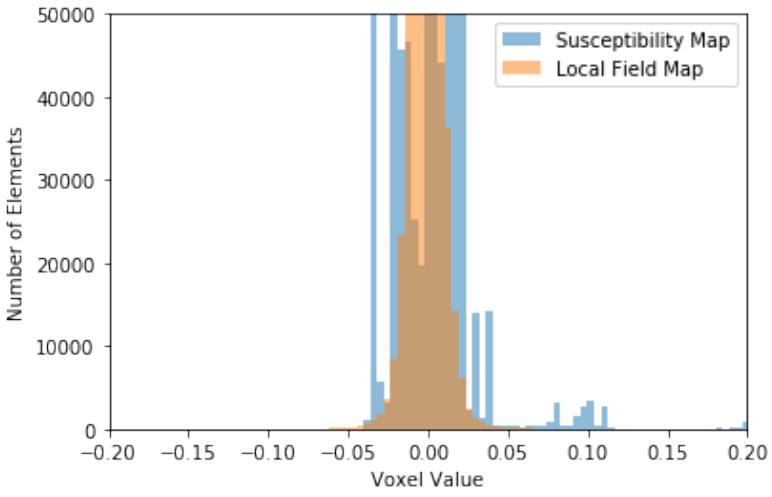

F gure 37: H stogram of suscept b ty map and oca f e d map of the numer ca bra n phantom. The suscept b ty map shows no norma d str but on.

3.8 In vivo Scan Data

A healthy volunteer was scanned using a commercial MRI scanner (Ingenia 3T, Philips, Best, The Netherlands) using a 15-channel head coil. An RF-spoiled gradient echo sequence was acquired with TR=30.5 ms, 4 echos at 3.8, 11.4, 19.0 and 26.6 ms, voxel size=1^3 mm, flip angle of 14°, transverse field direction, Compressed SENSE acceleration factor of 2.5 and scan duration of 6:25 minutes. The acquired data consists of four magnitude and phase data images at different echo times.

As GRE uses no 180° RF pulse, field perturbations cause a phase shift that changes linearly with time. As shown in Figure 5 GRE acquires several recalled echoes in a single run. Images of a higher echo time TE have more wrapping artefacts (as the phase accumulates over time) but are more precise to detect small field perturbations. The four phase images of the four echo times are used to estimate a single field map. Figure 38 shows the four phase images and the resulting field map with wrapping artifacts.

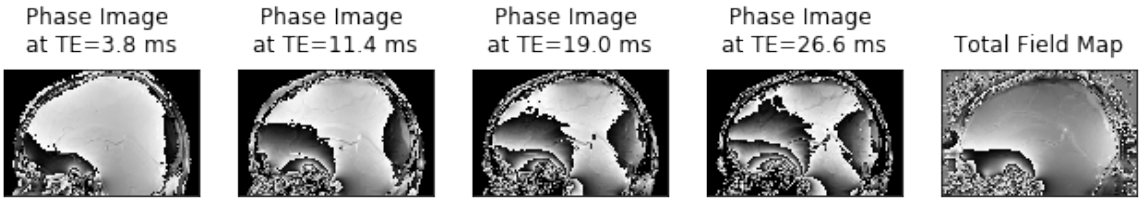

F gure 38: Phase mages and the correspond ng f e d map. A mages show wrapp ng art facts.

As the phase image values were in millirad the images were scaled to be in the range of $[-\pi, \pi]$ and phase unwrapping (using the unwrap_phase function by the skimage.restoration module) was performed afterwards (see Section 2.2.4).

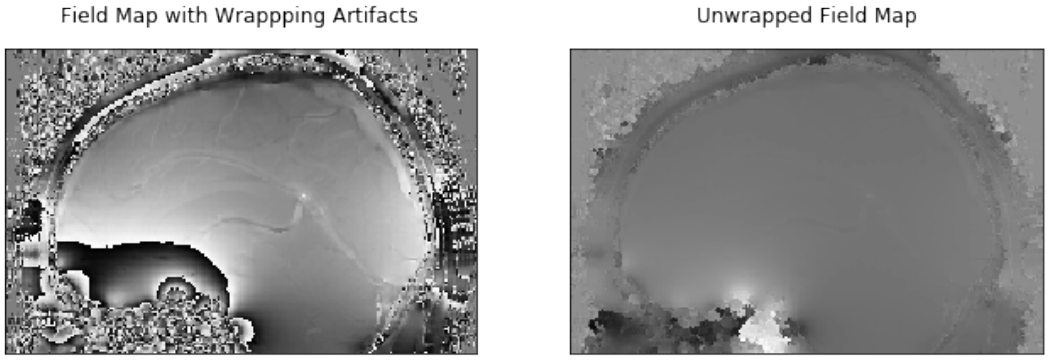

F gure 39: F e d map w th wrapp ng art facts on the eft and after unwrapp ng on the r ght. Both mages show the tota f e d.

A corresponding mask was designed using the magnitude image. To do so, thresholding and four iterations of binary closing (from the scipy.ndimage morphology module) were applied.

F gure 40: The magn tude mage on the eft was used to create the mask on the r ght for further process ng steps. In the area c ose to the s nuses a suscept b ty art fact was propagated to the mask.

To apply both mask and masked field map (total field) to the ANN, both images were cropped and the axes of them changed (so B_0 points into z-direction). To use the scan image as an input for the ANNs it had to be converted from the unit Hz to the unit ppm (parts per million) because the ANN was trained with data in ppm. Equation (3.30) describes the conversion. Parts per million is usually used to describe the field homogeneity of MRI scanners [81]. It is independent from B_0 of the scanner. In case of the field map, it describes the field perturbation caused by susceptibility towards the magnetic field B_0 and can be written as 10^{-6} in SI units.

$$Field\ map\ Hz \cdot \frac{1}{3\ T \cdot 42.6\ \frac{MHz}{T}} \quad Field\ map\ 10^{\ 6} \quad Field\ map\ ppm \tag{3.30}$$

3.9 Libraries and Tools

In the following, the technologies used in this thesis are briefly described to give an insight to the technical implementation. It focuses on the main technologies und its purposes and is not a comprehensive list.

Usage of Python and Python Libraries

The source code for data generation, data transformation, training and validation is written in the Python programming language [82]. The ANN model is built with Pytorch [78,83], a machine learning library for Python. It provides components to accelerate the implementation of layers, data-loading and further relevant tasks in training and validation. The library Nibabel is used to save and load 3D images [84]. By using the function 'seed' of the numpy and random module, the training data was reproducible.

Tools for Hyperparameter Optimization

To compare results and hyperparameters the software tool 'Sacred Python' was used [85]. In combination with 'Omniboard' results and parameters can be visualized [86].

Evaluation of different Algorithms for BFR and Dipole Inversion

To compare the results with established methods, that do not use deep learning, the Matlab Sepia tool [87] was used. Sepia builds on the Matlab FANSI [88], MEDI [89] and STI suite [90] toolboxes and facilitates to build data pipelines for phase unwrapping, background field removal and dipole inversion.

4 Results

This chapter is split into three top-level sections. Section 4.1 describes the results achieved with the DeepQSM baseline model for dipole inversion. All ANNs were evaluated with synthetic data consisting of geometric objects, a numerical brain phantom and in-vivo data. The outputs of the ANN for dipole inversion on in-vivo images were compared to the outputs of the STAR-QSM algorithm. Furthermore, the limitations of the ANN were investigated. Section 4.2 describes the results for the ANN that performs only background field removal. The performance on in-vivo images was compared to the VSHARP algorithm. Section 4.3 shows the results of an ANN that combines both background field removal and dipole inversion in one step. Again, the STAR-QSM algorithm was chosen to evaluate the model performance. The output of the one-step solution was compared to the output created using both the ANN for BFR and the ANN for dipole inversion.

4.1 ANN for Dipole Inversion

In this section, the results of the model for dipole inversion are presented. The model and its variations were tested on validation data. Furthermore, experiments were conducted to evaluate the ability to deal with features that were not included in the dataset for training. Afterwards, the model was tested on a numerical brain phantom and on preprocessed in-vivo data to evaluate its suitability for practical applications e.g. in clinics.

4.1.1 DeepQSM as Baseline for Evaluation

The DeepQSM architecture and its hyperparameters (see Section 3.1) served as baseline to evaluate the changes made. Figure 41 and Figure 42 show the learning progress during training. While the outputs of the model show fast improvements in the beginning, the improvements in later iterations are not so clearly visible. However, the logarithmic plot of the losses Figure 42 shows that the model still improves after 20000 steps. Furthermore, the decrease of train and validation loss by the same amount indicates that the model does not overfit while training.

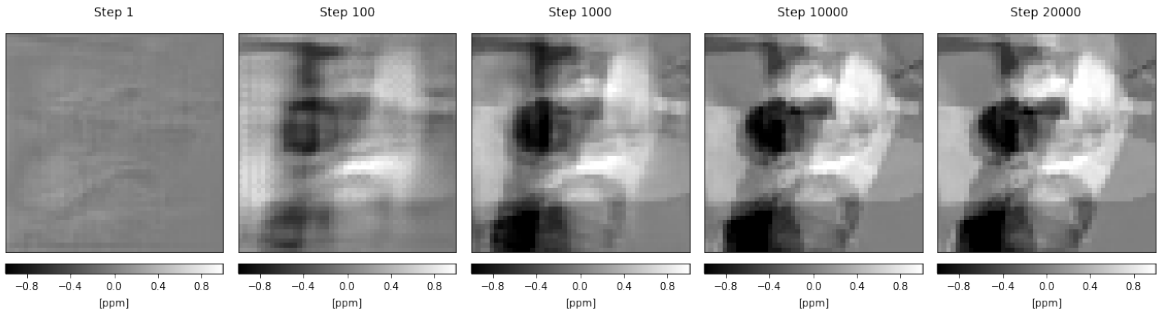

F gure 41: Progress n mage reconstruct on dur ng tra n ng.

F gure 42: Learn ng progress dur ng tra n ng. Both tra n and va dat on osses mprove.

The performance is demonstrated in Figure 43 where the output image of the ANN was compared with the corresponding ground truth image. The ANN attained a RMSE of 0.218 ppm and a SSIM of 0.948, what is slightly better than the RMSE attained in the last validation during training (see Table 3). Depending on the images used, the losses differ slightly.

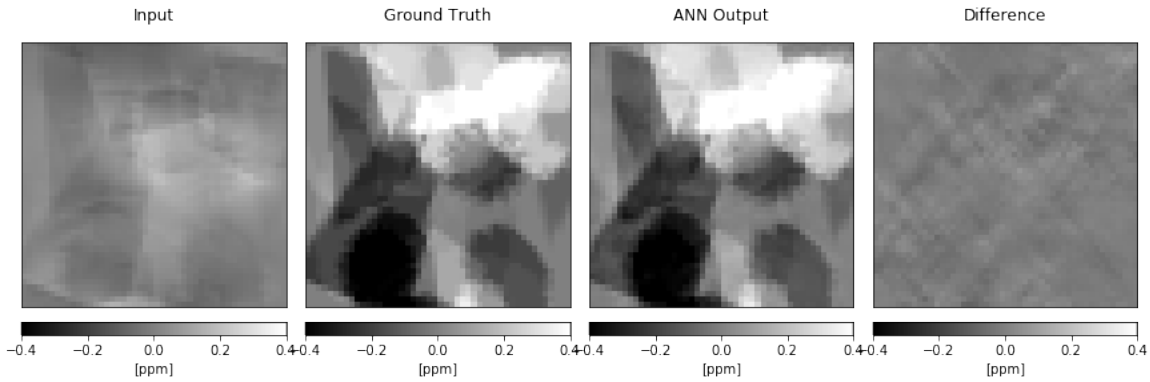

F gure 43: A 48³ voxe mage of the va dat on dataset was tested w th the DeepQSM base ne mode .

4.1.2 Improving Model Performance

To improve the performance several variations referring hyperparameters, dataset and architecture were investigated. For each training, only a single modification was changed.

Learning Rate

First, the learning rate was increased by a factor of 10 to 0.01. The idea behind was to accelerate the convergence to the minimal loss. However, the outcome showed a RMSE of 0.1734 ppm compared to 0.0236 ppm to the baseline model. The learning rate seems to be too high, so the minimum is skipped (see Figure 18). In the logarithmic training plot of the DeepQSM baseline model (see Figure 43) two peaks are visible around 14000 and 18000 steps. To avoid such peaks the learning rate was decreased. Furthermore, after 20500 training steps the DeepQSM baseline model had a higher RMSE loss of 0.0385.

Weighted Image Gradient Loss

Inspired by QSMnet [4] the weighted image gradient loss (WGL) described in Section 3.3.1 was used for optimization. The validation loss during training showed improved outcomes (0.0217 ppm). Figure 44 shows the comparison between output and ground truth. In Section 4.1.5 the model is also tested with in-vivo data input.

Kernel Size

The kernel size was changed from 3^3 to 5^3 to increase the number of learnable parameters and to increase the receptive field. However, the performance did not improve.

Number of Steps

The number of steps was increased to check if the model continues to converge. The model reached an improved loss of 0.0201. Figure 44 shows the comparison between output and ground truth.

Dataset with larger image size

The images for training were increased in size from 48^3 voxel to 128^3 voxel. This allowed the ANN to remove fields of sources from a greater distance. In total, 1700 images were used for training and 100 for validation. In contrast to the previous models, no white veil is visible in the 128^3 voxel image in Figure 44. The model was later tested with in-vivo data in Section 4.1.5.

Deeper ANN

The model architecture was changed to be able to down sample the input image by an additional layer level (see Section 3.2). Through this, the receptive field of the ANN enlarges. The dataset with 128^3 voxel was used as the model had to use input images with a size of at least 96^3 voxels. Due to this, it cannot be evaluated on 48^3 voxel images. Like the previous model that was trained with 128^3 voxel images but the same architecture as DeepQSM, there is no veil visible. In comparison, the deeper ANN shows slightly worse losses than the one using the DeepQSM architecture but larger training data.

Dataset with small strong susceptibilities

To improve the ability to detect vessels in in-vivo data a new dataset with cylinder shaped objects was created. These objects had a higher susceptibility then the surrounding objects (0.1-0.3 ppm). Afterwards, the images were scaled as described in Section 3.4. The images of this dataset had a size of 48^3 voxel. During training, the ANN had a higher loss of 0.0328 ppm than the DeepQSM baseline model.

Table 3 shows the validation losses of different model variations during their last training iteration. The values are averaged over multiple images. For the validation of the models that used 48^3 voxel data, 1000 validation images were evaluated towards their voxel wise loss and averaged. For the ANNs that used 128^3 voxel images only 100 images were used to average the losses.

Model	RMSE in ppm	slope	SSIM
DeepQSM baseline	0.0236 ± 0.0128	0.985	0.934 ± 0.018
Learning rate=0.01	0.1734 ± 0.0752	1.054	0.229 ± 0.041
Learning rate=0.0001	0.0385 ± 0.0268	1.008	0.837 ± 0.052
Weighted gradient loss	0.0217 ± 0.0116	1.016	0.946 ± 0.015
Kernel size 5^3	0.0280 ± 0.0173	1.002	0.904 ± 0.028
41000 steps	0.0201 ± 0.0120	1.013	0.952 ± 0.015
Dataset with cylinders (StD scaled)	0.0328 ± 0.0221	1.014	0.885 ± 0.040
Deeper Model $+128^3$ voxel Dataset	0.0161 ± 0.0103	0.956	0.970 ± 0.0388
Dataset 128^3 voxel	0.0177 ± 0.0113	0.959	0.968 ± 0.0387

Tab e 3: Overv ew of the va dat on osses ca cu ated n the ast tra n ng step.

Models with an improved performance were tested on two images of size 48^3 voxel and 128^3 voxel. A larger input image makes it possible to evaluate various objects (e.g. spheres and cylinders of different size) at once and to notice artifacts in the surrounding. Figure 44 shows image results of the two input images off different size and the differences towards the ground truth. Table 3 shows the corresponding losses.

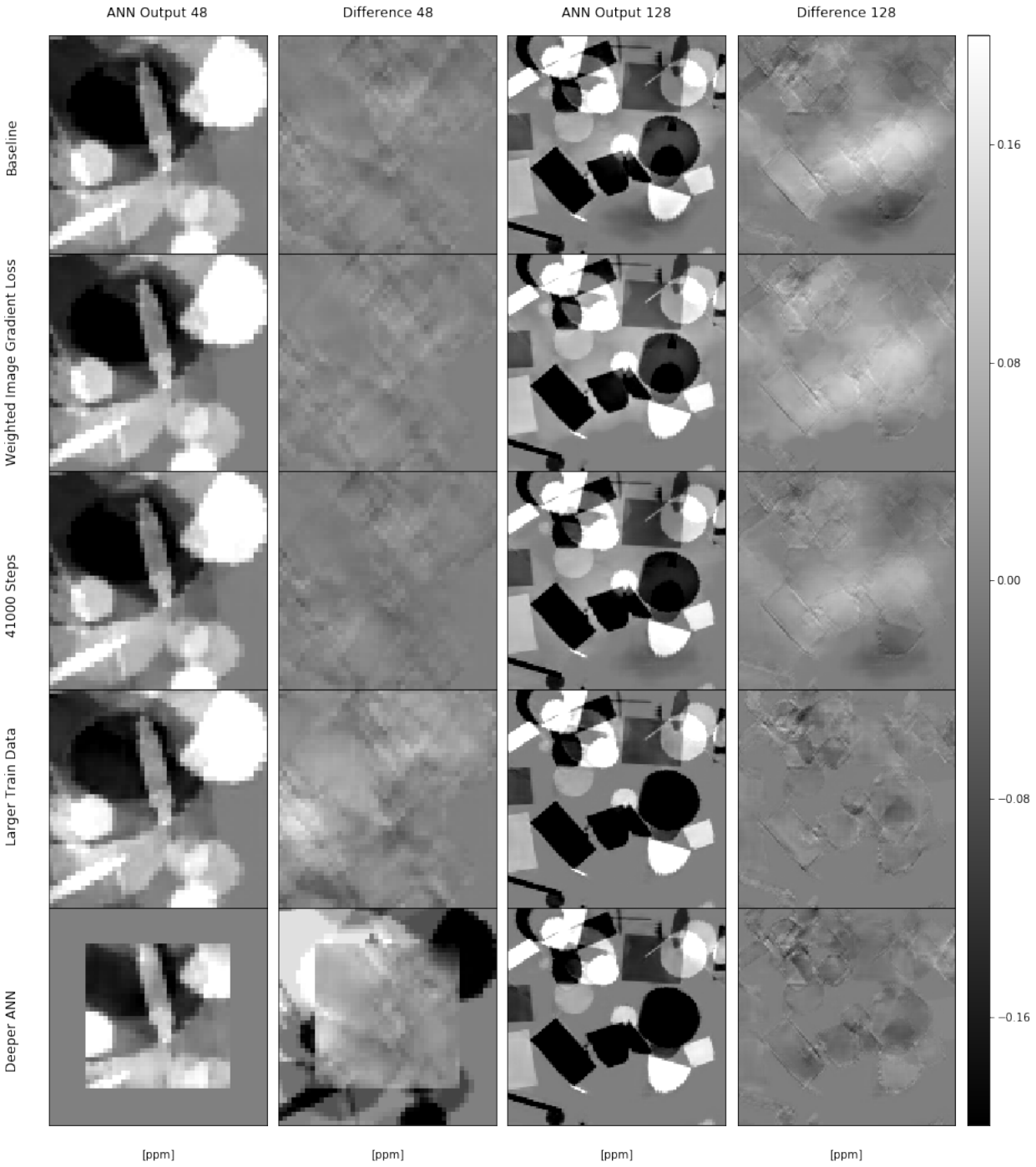

F gure 44: Eva uat on of d fferent ANNs us ng an nput mage of s ze 48³ voxe and one of 128³ voxe

All ANNs perform better on input images of the same size as their training data (see Table 3). Images that were trained on smaller images show a white veil in the output image that is not visible if they were trained with larger images. The ANN that was trained with 41000 steps shows less veil than the DeepQSM Baseline Model and the WGL Model.

	48^3 voxel Input Image			128^3 voxel Input Image		
Model	RMSE [ppm]	slope	SSIM	RMSE [ppm]	slope	SSIM
Baseline	0.0218	1.021	0.9480	0.0392	1.056	0.765
WGL	0.0189	1.014	0.9542	0.0412	1.045	0.715
41000 Steps	0.0176	1.005	0.958	0.0309	1.030	0.770
Larger Data	0.0464	1.038	0.831	0.0135	1.008	0.977
Deeper	No comparison possible as this ANN can only process images of size >= 96^3			0.01761	0.952	0.967

Tab e 4: Eva uat on of d fferent ANNs us ng an nput mage of s ze 48^3 voxe and one of 128^3 voxe .

4.1.3 Stability of DeepQSM

The performance of a trained ANN depends on the features presented during training. This section describes the ability of DeepQSM to deal with features that were not part of the dataset. This includes larger shapes and susceptibility values, noise, new patterns of field perturbations and a different scaling of the input.

4.1.3.1 Strong Susceptibilities

In the following experiment, the model was tested towards its ability to deal with strong susceptibility sources and large volumes that were not included in the training data set. As the strength of the internal field of a susceptibility source depends on its susceptibility value and its volume [35] this experiment demonstrates the correction of strong fields caused by susceptibility. In case of large volumes, the field decreases less rapidly with distance and the model can be investigated towards its ability to correct field perturbations that are far away from its origin.

The ANN was trained with susceptibility values with a standard deviation of 0.2 ppm around zero. Here, it was confronted with a much stronger susceptibility of 1 ppm (bottom left in Figure 45) in the input. In the input image, the typical dipole field (compare to Figure 45) is apparent. The strong field of the source causes artifacts in the close surrounding area.

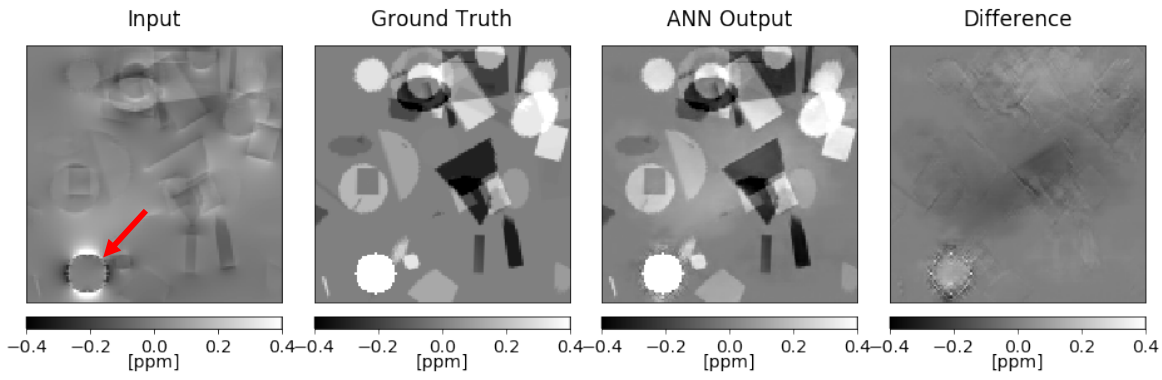

F gure 45: Added strong suscept b ty source w th χ=1ppm r=10.

Figure 46 shows the results of an experiment with an added susceptibility of 0.3 ppm. Here the differences are comparable to the other objects as added objects like the one of 0.3 ppm were part of the train dataset.

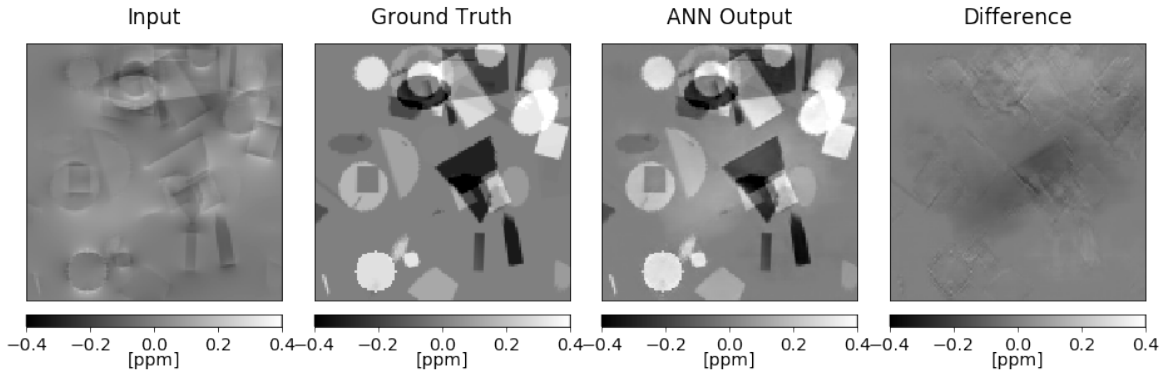

F gure 46: Added strong suscept b ty source w th χ=0.3 ppm r=10.

In the next experiment, the volume was enlarged to 32 pixels while the susceptibility was again 0.3 ppm. The strong field with wide reach was not removed. Furthermore, the susceptibility values inside of the additional source were not reconstructed correctly (see Figure 47).

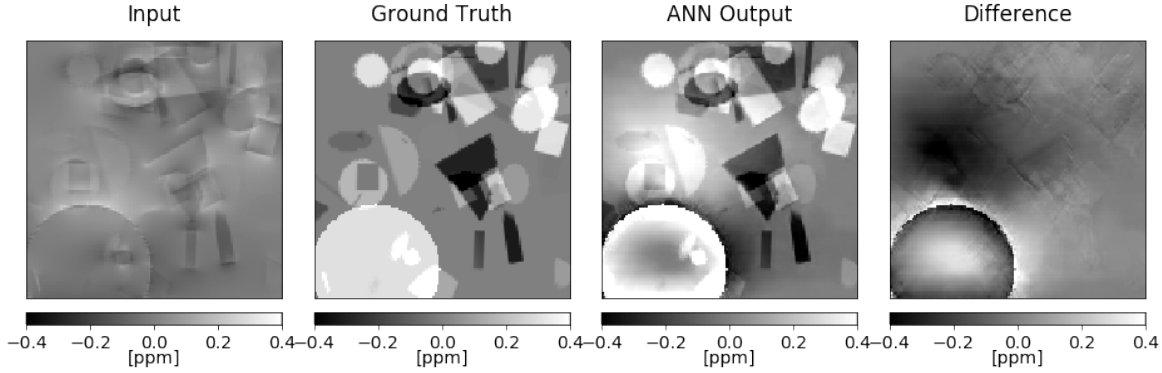

F gure 47: Added strong suscept b ty source w th χ=0.3 ppm and rad us=32p xe .

To separate the effect of the strong source from the other errors the difference image of the ANN output without and with additional strong susceptibility were subtracted from each other in Figure 48.

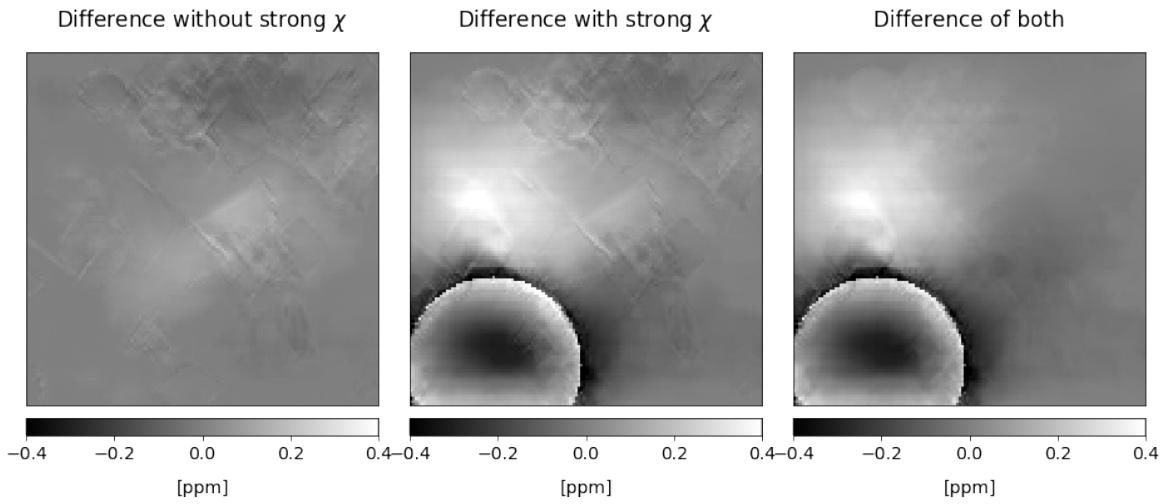

F gure 48: D fference mage of the d fference mage w th and w thout strong suscept b ty source. The resu t ng mage shows on y art facts produced by the add t ona source.

The experiment of the additional strong susceptibility with radius=32 and χ=0.3 was repeated with the deeper ANN (see Figure 48) and the ANN that was trained with larger images (see Figure 49). Both show less artifacts in the surrounding area. The Deeper ANN shows no problems to reconstruct the susceptibility values of the additional source. According to the losses in Table 5 it is not possible to say that one is better than the other. However, both perform better than the DeepQSM Baseline Model.

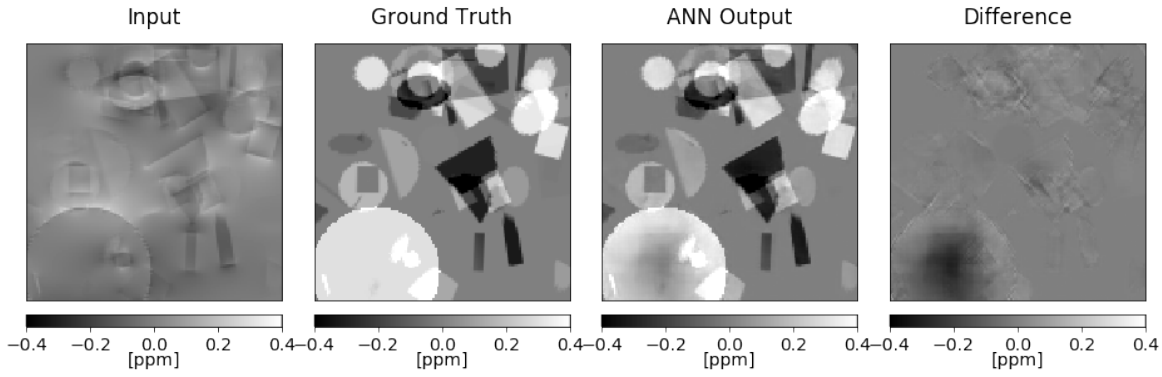

F gure 49: Added strong suscept b ty source w th χ=0.3 ppm and rad us=32 p xe eva uated w th the ANN that was tra ned w th mages of s ze 128³ voxe and the DeepQSM arch tecture.

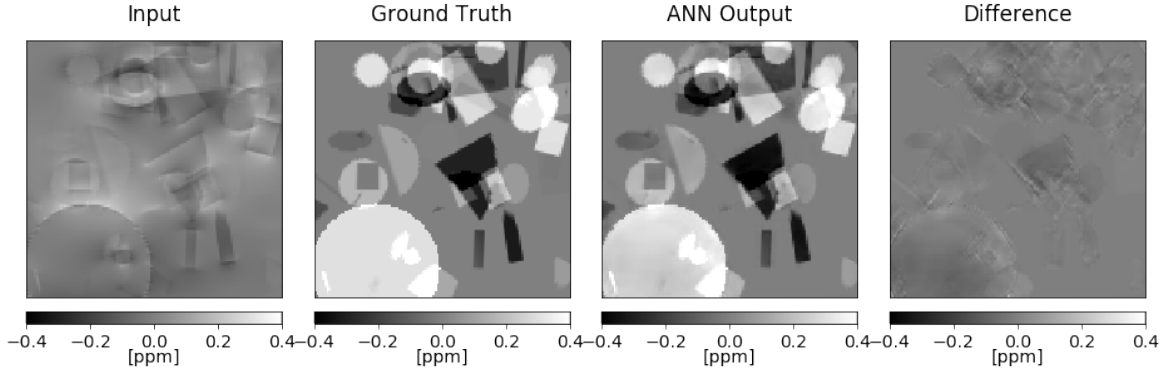

F gure 50: Added strong suscept b ty source w th χ=0.3 ppm and rad us=32 p xe eva uated w th the ANN that was tra ned w th mages of s ze 128³ voxe and deeper arch tecture.

Table 5 summarizes the results of the different experiments. The experiments show that the ANN has difficulties to process data that is not similar to the training set in objects size and susceptibility value. Furthermore, strong fields stretching far over the image are not removed completely. Furthermore, in the ANN output the susceptibility value of the new object is displayed incorrectly if it had a strong susceptibility (Figure 49 and Figure 50). However, in all images all objects are clearly distinct.

Architecture	Image size of Training Data (voxel)	Additional χ	RMSE [ppm]	slope	SSIM
DeepQSM	48^3	Baseline	0.0392	1.056	0.765
DeepQSM	48^3	Radius=10 χ =1	0.0400	0.882	0.757
DeepQSM	48^3	Radius=10 χ =0.3	0.0392	0.879	0.765
DeepQSM	48^3	Radius=20 χ =0.3	0.04118	0.871	0.750
DeepQSM	48^3	Radius=32 χ =0.3	0.1020	0.961	0.548
DeepQSM	128^3	Radius=20 χ =0.3	0.0185	0.946	0.966
DeepQSM	128^3	Radius=32 χ =0.3	0.0203	0.962	0.9616
Deeper ANN	128^3	Radius=20 χ =0.3	0.0146	0.997	0.977
Deeper ANN	128^3	Radius=32 χ =0.3	0.0231	1.018	0.969

Tab e 5: Added strong suscept b ty sources. The resu ts for the add t ona χ w th rad us=20 and χ =0.3 d sp ayed n th s tab e were not v sua zed for the Deeper ANN and the ANN tra ned w th arger mages.

4.1.3.2 Cylinders

In this experiment, the baseline model was investigated towards its ability to process additional small cylindrical susceptibility sources. Such objects simulate brain vessels in in-vivo data. Furthermore, the outcome was compared to a model that was trained with cylindrical sources.

Even if the validation loss of the baseline model was better than the validation loss of the cylinder-model, the cylinder-model was superior in this test:

Model tested with cylinder Data	RMSE [ppm]	slope	SSIM
DeepQSM Baseline	0.0402	0.878	0.761
Cylinder Dataset	0.0340	0.92044	0.814

Tab e 6: Compar son of mode s that were tra ned w th d fferent datasets. The mode s were tested w th nput dta con-ta n ng sma cy ndr ca objects w th s ght y h gher suscept b ty than the other objets. The mode that was tra ned w th such data performed better

Figure 51 and Figure 52 show the results of both ANNs. The visual analyzes of the images reveals only little differences.

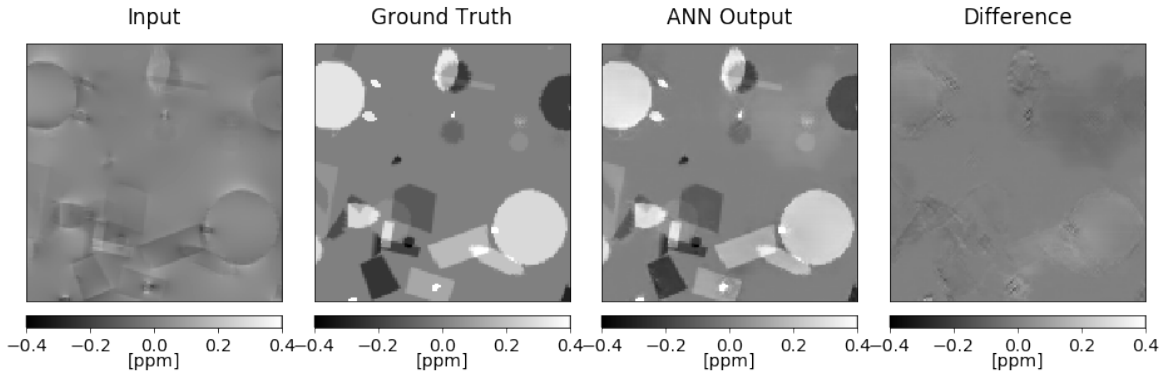

F gure 51: Resu ts of the DeepQSM Base ne mode that was tra ned w th the dataset w thout add t ona sma cy nders w th strong suscept b ty.

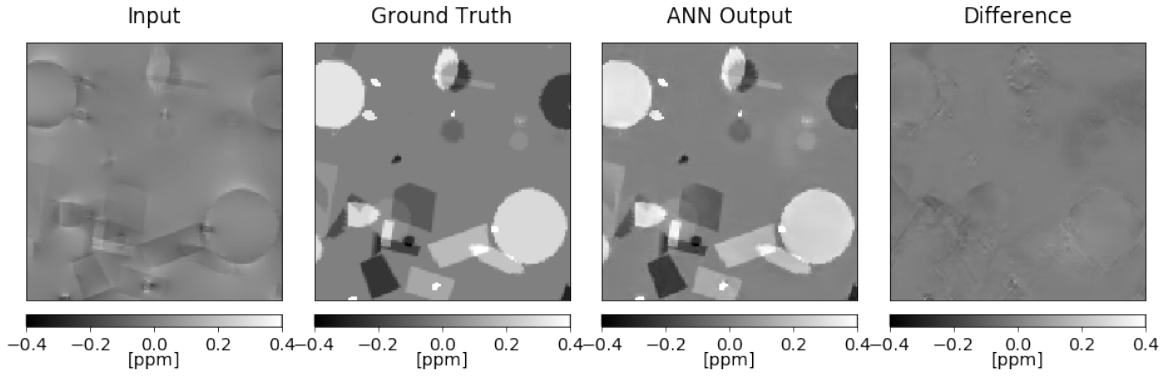

F gure 52: Resu ts of the mode that was tra ned w th the dataset conta n ng add t ona sma cy nders w th strong susceptb ty.

4.1.3.3 Scaling

In the following experiment, the model was investigated towards its stability towards different scaled inputs. Forward solution and ground truth were both scaled by different scaling factors. The forward solution served as input for the DeepQSM baseline model and the output was compared to the scaled ground truth.

Scaling Factor	RMSE / S in ppm	Slope	SSIM
S=1	0.0392	1.056	0.765
S=10	0.0548	1.181	0.316
S=100	0.0578	1.209	0.240
S=1000	0.0581	1.212	0.237

Tab e 7: Compar son of Output w th d fferent sca ed Input. The osses of the outsputs w th sca ed nput were d v ded by the sca ng factor S. The outputs were compared to a Ground Truth that was correspond ng y sca ed.

Table 7 shows that a scaling factor greater than one (>1) increased the loss of the output.

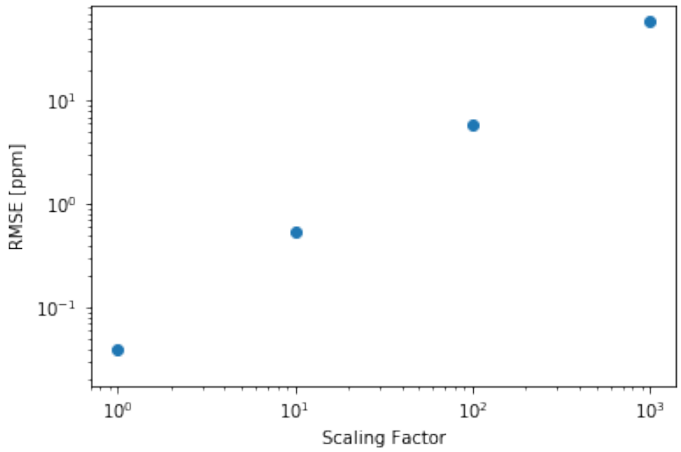

F gure 53: Dependency of RMSE oss on the sca ng of the nput

However, the corresponding outputs of the scaled inputs show no strong artifacts, the objects are clearly visible. Figure 53 and Figure 54. The model shows a high stability towards scaled inputs.

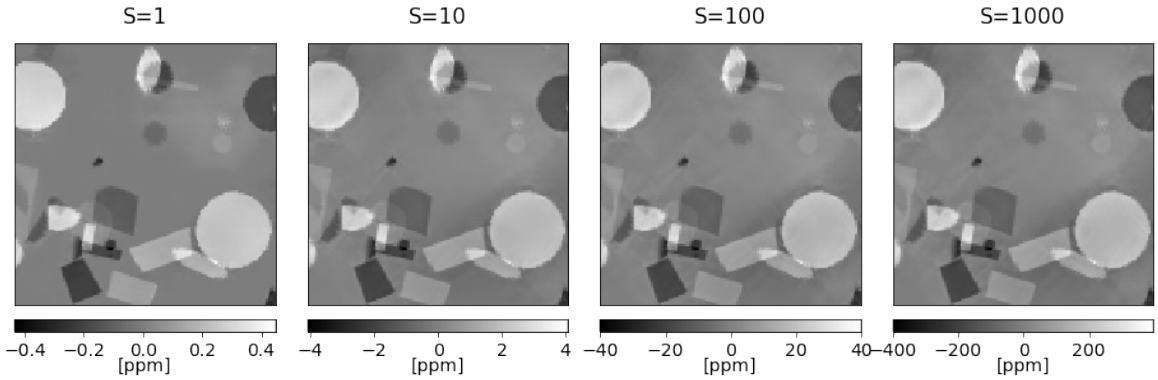

F gure 54: Outputs of the DeepQSM Base ne Mode that was fed w th sca ed nputs.

4.1.3.4 Noise

In the training phase, the input images were free of noise. The following experiment investigated the capability of the trained ANN to cope with noisy images. The test input image was intentionally distorted with Gaussian noise, while the ground truth remained unchanged for assessment. A noise distribution with a standard deviation of 0.01 around zero was chosen and added to the ANN input. Figure 55 shows the distorted input image and the results with distortions left. Table 8 compares the loss between ground truth and noisy input in comparison with the baseline.

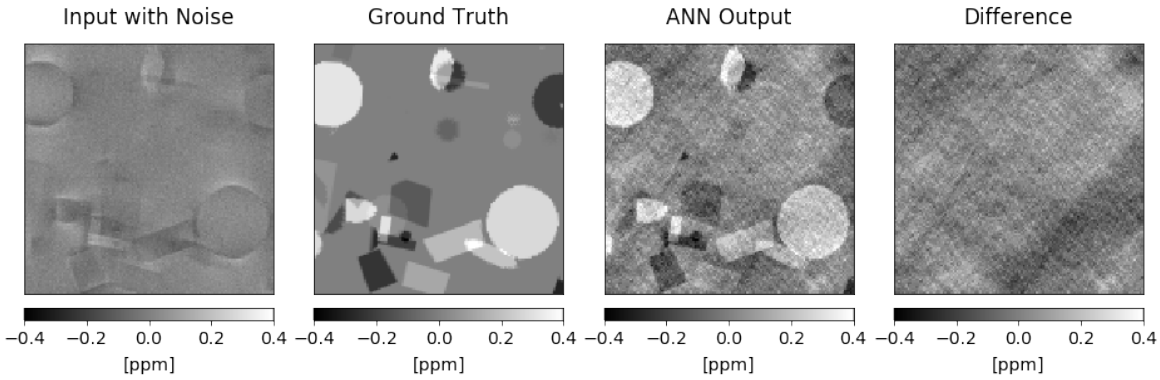

F gure 55: Gauss an no se w th a standard dev at on of 0.01 was added to the nput. The output was compared to the ground truth w thout no se.

	RMSE	Slope	SSIM
No Noise	0.0392	1.056	0.765
Noisy Input SD 0.01	0.0875	0.836	0.335

Tab e 8: The osses of the mode w thout no sy nput and w th no sy nput were compared.

The experiment was repeated with added noise and the difference between ground truth and ANN output was evaluated. The plot shows that the noise in the output increased linearly to the noise in the input Figure 56.

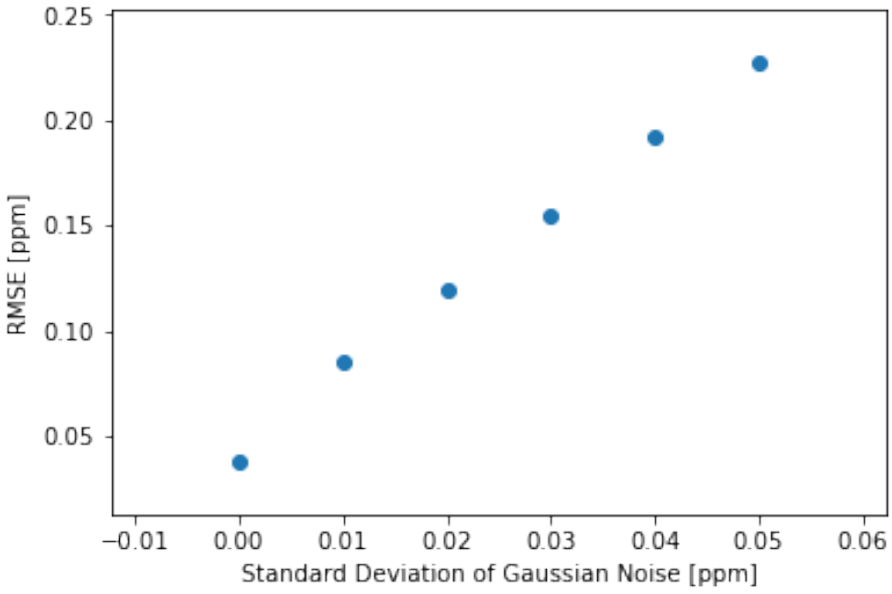

F gure 56: Dependency of the RMSE oss on the standard dev at on of no se

4.1.3.5 Propagation of non-Dipole-Kernel Sources

Field maps might contain non-dipole contributions. E.g., blood flowing along the readout direction will acquire a phase shift proportional to its velocity. This leads to patterns in the field map that cannot be well described as a superposition of elementary dipoles, leading to model errors.

The following experiment investigated the propagation of field perturbations that are not caused by the convolution of the dipole kernel with the susceptibility map (the convolution is described in

Section 2.2.2). In order to do so, a spherical object (emphasized by an arrow in Figure 57: Output of the DeepQSM Baseline Model that was fed with an added volume in the input that was not created by the convolution with the dipole kernel. The output shows strong non-local artifacts.) was added to the forward solution input of the ANN. The ANN output in Figure 57 shows strong non-local artifacts. Furthermore, the losses in Table 9 deteriorate.

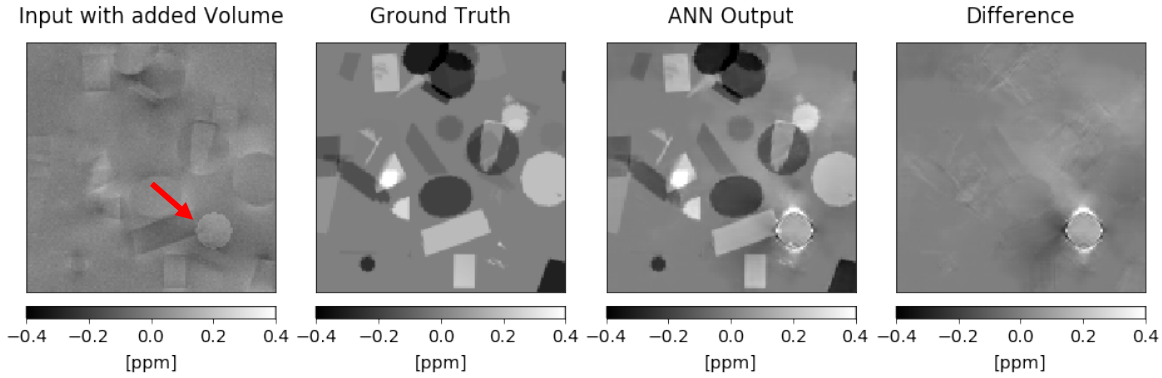

F gure 57: Output of the DeepQSM Base ne Mode that was fed w th an added vo ume n the nput that was not created by the convo ut on w th the d po e kerne . The output shows strong non- oca art facts.

	RMSE [ppm]	Slope	SSIM
No Additional Object	0.0392	1.056	0.765
Additional Object	0.0875	0.836	0.334

Tab e 9: The DeepQSM Base ne Mode was tested w th an add t ona object n the nput oca f e d map. The osses are s gn f cant y h gher than w th no such object.

4.1.4 Numerical Brain Phantom

The experiments in the previous sections used input and label images consisting of simple geometric objects for evaluation. For the following experiment, a numerical brain phantom served as ground truth and its forward solution as input. The brain phantom is not as detailed as in-vivo images and has no vessels, but it has the possibility to evaluate the model with a complex brain-like structure. The creation of the brain phantom is described in Section 3.7. Figure 58 shows that all structures were reconstructed. However, some areas like the cerebellum are overestimated while other parts were underestimated.

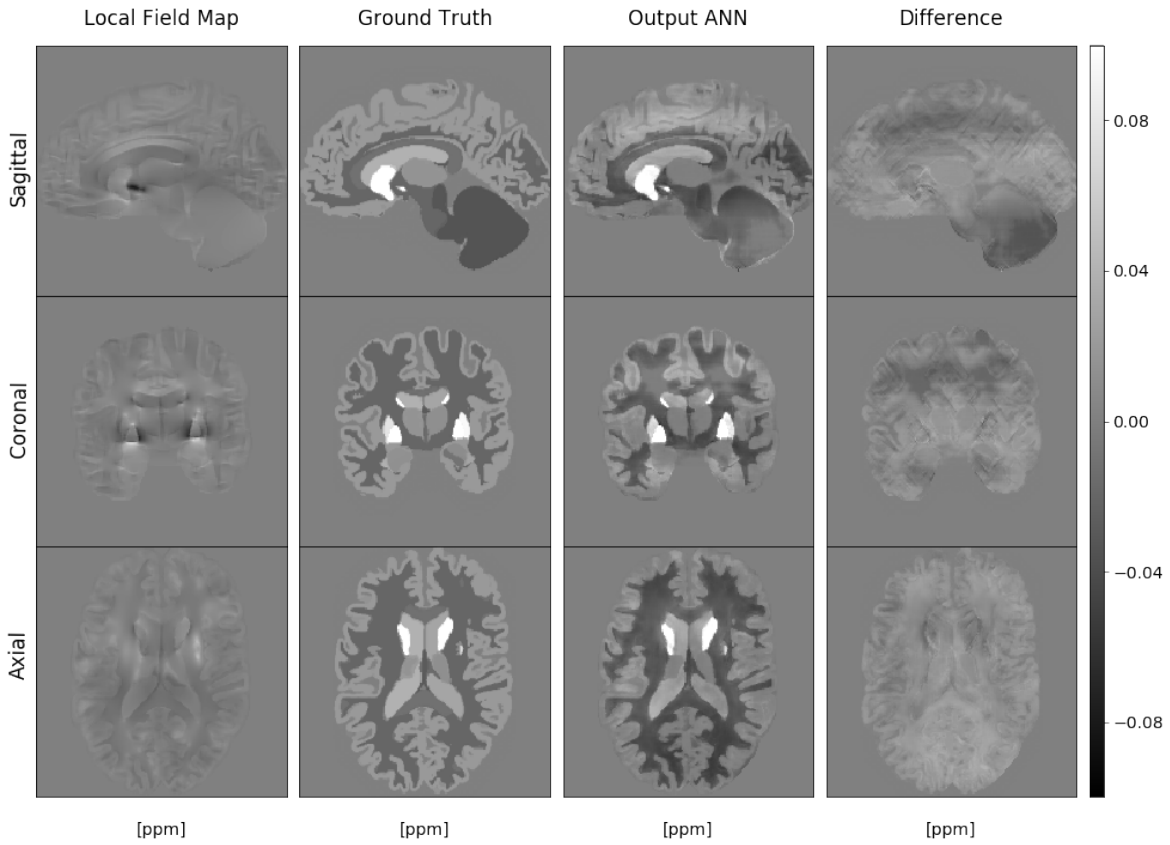

F gure 58: Compar son of the DeepQSM Base ne Mode output w th the ground truth. As nput served a numer ca bra n phantom that was convo ved w th the d po e kerne .

Next to the DeepQSM Baseline Model the ANN trained with 128^3 voxel train images was evaluated on the numerical phantom Figure 59.

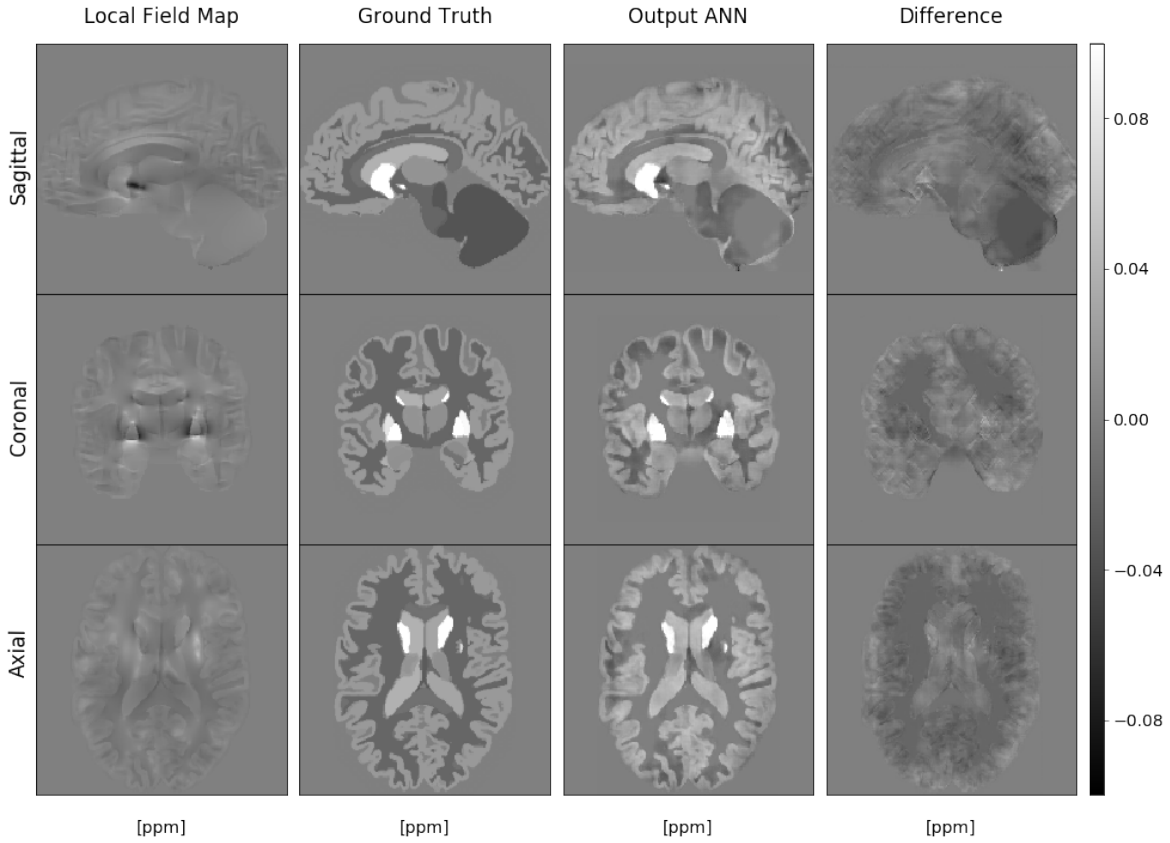

F gure 59: Compar son of the resu ts from DeepQSM arch tecture us ng tra n ng data w th a s ze of 128³ voxe per mage.

Table 10 shows that the resulting RMSE and SSIM are better compared to the losses of the model evaluated with geometric objects.

Model	Data Input	RMSE [ppm]	Slope	SSIM
DeepQSM Baseline	Geometric objects	0.0392	1.056	0.765
DeepQSM Baseline	Numerical Brain Phantom	0.0101	0.774	0.899
Larger Data	Numerical Brain Phantom	0.0088	0.787	0.928

Tab e 10: Losses severa ANNs tested w th the numer ca bra n phantom

4.1.5 In-vivo Data

To assess the quality of the ANN to process in-vivo data of real MRI scans, a scan as described in Section 3.8 was performed. The phase data was field mapped and unwrapped. Afterwards, the sepia toolbox was used to perform a background field removal. In order to do so, several algorithms were tested (see Section 4.2, Figure 69) for background field removal. The local field of the VSHARP algorithm served as input for different algorithms for dipole inversion. The results are visualized in Figure 60.

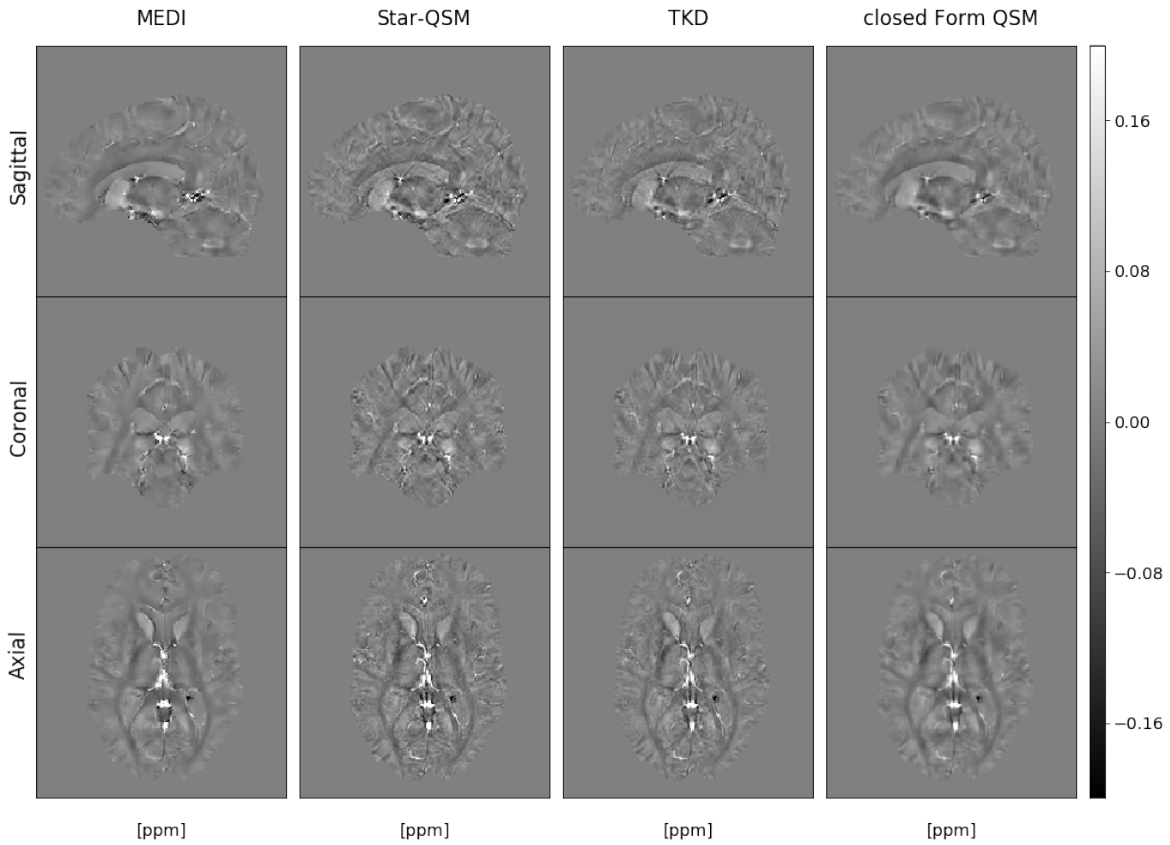

F gure 60: Compar son of the ava ab e a gor thms for d po e nvers on n the sep a too box.

In contrast to the experiments with synthetic data no ground truth exists to compare with. Due to the visual impression, the STAR-QSM output was chosen for further comparisons. Figure 61 compares the output of the DeepQSM Baseline Model with the output of STAR-QSM. The output of the ANN seems to have less noise than the STAR-QSM output. Furthermore, the susceptibility values differ slightly. Figure 62 shows a scatter plot of both images.

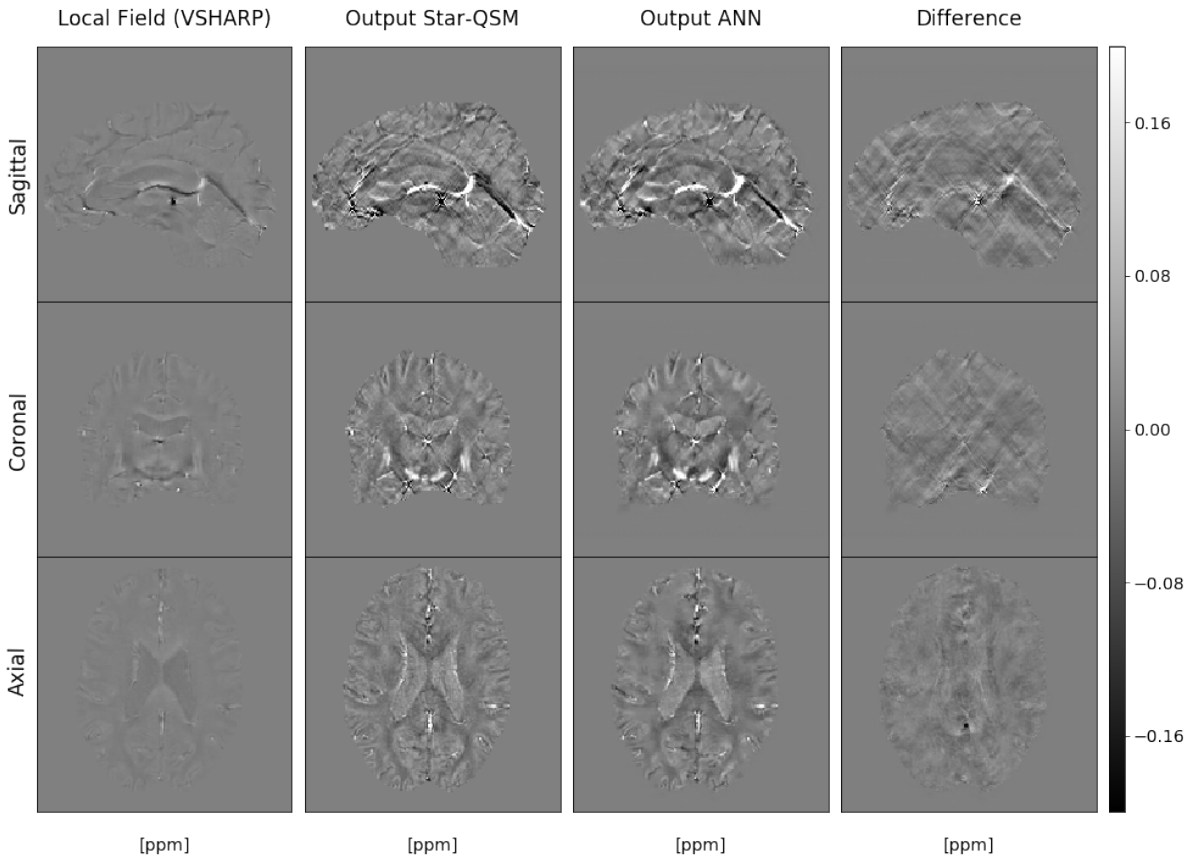

F gure 61: Compar son between the STAR-QSM output and the output of the DeepQSM Base ne Mode .

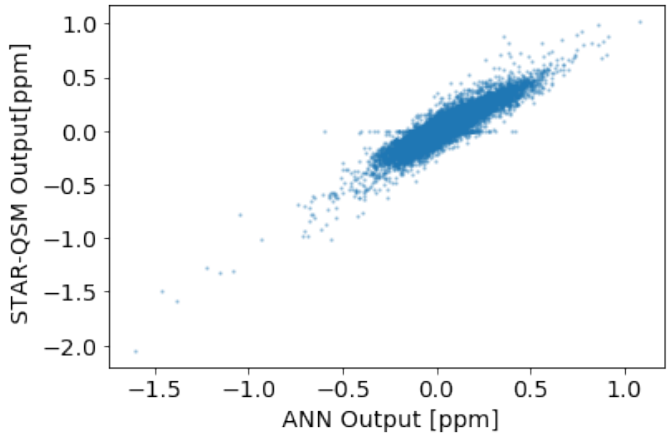

F gure 62: Scatter p ot of the STAR-QSM output and the output of the DeepQSM Base ne Mode .

Figure 63 shows the outputs of further models that were used for dipole inversion. The left column shows the output of the model that used the weighted image gradient loss during training. In the middle is the output of the model trained with additional small cylinders with strong susceptibility in the dataset. Both outputs look very similar. The former seems to create slightly stronger values. The right column shows the output of the ANN that was trained with images of size 128^3 voxel. Here, the tissue looks rather spotty.

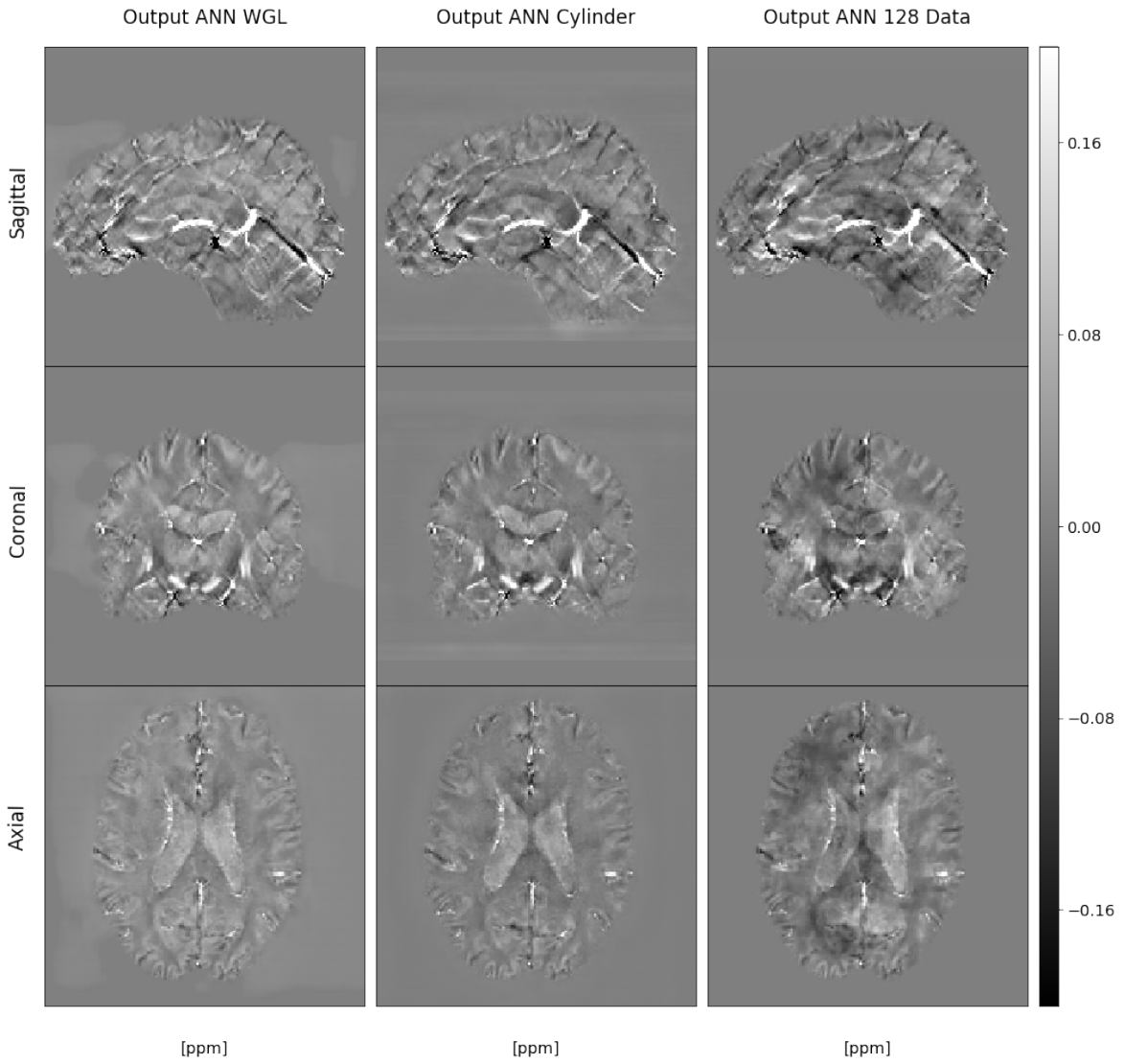

F gure 63: Further mode s that were used for d po e nvers on. The eft co umn shows the output of the ANN that used the we ghted mage grad ent oss dur ng tra n ng. In the m dd e s the output of the ANN tra ned w th add t ona sma cy nders w th strong suscept b ty n the dataset. The r ght co umn shows the output of the ANN that was tra ned w th mages of s ze 128³ voxe .

4.1.6 Discussion

The DeepQSM ANN shows very good results in dipole inversion for synthetic data (RMSE=0.0236 ppm, slope=0.985, SSIM=0.934), for the numerical brain phantom (RMSE=0.0101 ppm, slope=0.774, SSIM=0.899) and for in-vivo data. Due to the lack of a ground truth for in-vivo data, the ANN output was compared to the established dipole inversion technique STAR-QSM (see Figure 61). Here, the ANN output shows superior results visually, as the output is less noisy.

Variations in the dataset or architecture led to an improved validation loss (see Table 3). The ANN using the weighted image gradient loss achieved a SSIM of 0.946. The ANN with 41000 training steps achieved a SSIM of 0.952. The ANN that was trained with larger images of size 128³ voxel instead of 48³ voxel achieved a SSIM of 0.968 and the ANN that used a deeper architecture a SSIM

of 0.970. As the latter two ANNs used larger images for training and validation, the losses are not fully comparable by SSIM or RMSE (see Section 3.3.4). ANNs that were trained with images of size 48^3 voxel performed worse when tested on images of size 128^3 voxel and the other way around. The ANN trained with larger data and the DeepQSM architecture performed better in case of the numerical brain phantom (RSME=0.0088, slope=0.787, SSIM 0.928, see Table 10) but shows spotty irregularities if tested with in-vivo data (see Figure 63). The dataset with size 48^3 voxel consisted of 70400 image pairs for training while the one with images of size 128^3 voxel used only 1700 image pairs for training. Even though a larger image contains nineteen $(128/48)^3$ times the amount features per image, the amount of data was not balanced and the ANNs using larger images was at a disadvantage.

Experiments with additional strong susceptibility sources and the evaluation with input images of size 128^3 voxel showed the ability to remove dipole fields decaying over a large distance (see Section 4.1.3.1, Section 4.1.2). Here, ANNs trained with larger images were superior to ANNs trained with 48^3 voxel data that left a veil of remaining local field in the image. As the receptive field of DeepQSM is of size 48^3 voxel, the ANN only learnt to remove fields within this area. The ANN trained with larger images seemed to also remove fields that were caused by sources outside of the receptive field. The ANN trained with weighted image gradient loss was superior to the DeepQSM Baseline Model if tested with small images but showed worse results if tested with larger input images (see Table 4). This could mean that the network learns less to generalize.

Next to the experiment with additional strong susceptibility sources (Section 4.1.3.1), the evaluation with images of other sizes (see Table 4) or scaling (Section 4.1.3.3) and the evaluation with input images containing additional cylinders with strong susceptibility (see Section 4.1.3.2) showed that small changes compared to the used dataset deteriorate the performance of the corresponding ANN. However, artifacts were not strong, so all objects were recognizable. The strongest artifacts were created in the experiment Propagation of non-Dipole-Kernel Sources: Here strong non-local artifacts appeared if the input image contained field perturbations that were not caused by a convolution with the dipole kernel.

The experiment about noise propagation showed that noise is amplified linearly. By adding noise to the input training data, the ANNs could potentially also learn to remove the contained noise [91].

Briefly, the DeepQSM showed promising results for dipole inversion compared to the established dipole inversion technique STAR-QSM. The size of training dataset and test data, as well as distribution have a large impact on performance. However, since there are no labels available for in-vivo images, it can not be concluded with certainty that the improvements can be transferred from synthetic data to in-vivo data.

4.2 ANN for Background Field Removal

As described in Section 3.5 different datasets were used for training. These datasets differ in structure and standard deviation of their values. Several experiments were performed to investigate the performance of the models trained with the various datasets. For evaluation, synthetic data with geometric objects, a numerical brain phantom and scan data served as model input.

4.2.1 Evaluation on Synthetic Data

The trained models that used different datasets for training were evaluated. They were tested with data similar to their training data and with data that corresponds to the training data of the other models. As described in Section 3.5, the different datasets differed in their standard deviation (especially in the total field) and in the (non-)presence of an offset. Due to this, the models show different results for the three different data inputs shown in Figure 64.

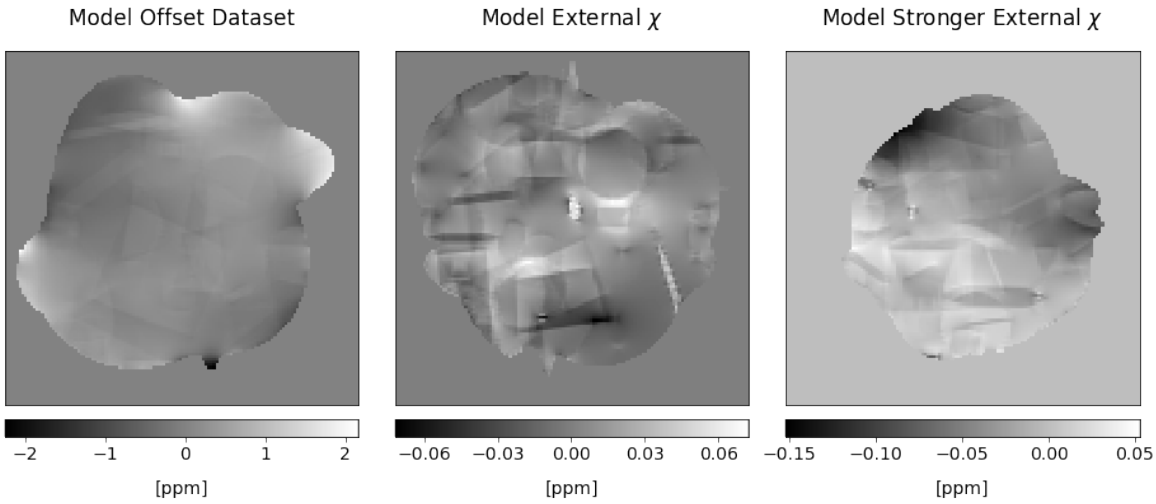

F gure 64: The three tota f e d nputs that were used for eva uat on of the ANNs. The mage on the eft used an offset n the ROI to create the background f e d and has a h gh standard dev at on. The mage n the m dd e and on the one on the r ght s de were created w th externa suscept b ty sources and d d not use an offset. The standard dev at on of the r ght mage s h gher than the one n the m dd e but sma er than the one of the mage on the eft s de.

The results of the three ANNs are displayed in Figure 65. Here, the results of the three different inputs for one ANN are displayed in one column. Table 11 contains the losses.

	Output ANN Offset Dataset	Output ANN External χ Dataset	Output ANN Stronger External χ Dataset
Input Offset Dataset	RMSE: 0.0034 slope: 1.187 SSIM: 0.984	RMSE: 0.0231 slope: 0.164 SSIM: 0.818	RMSE:0.02958 slope: 0.178 SSIM: 0.834
Input External χ Dataset	RMSE: 0.0121 slope: 0.072 SSIM: 0.867	RMSE: 0.0012 slope: 1.007 SSIM: 0.998	RMSE: 0.0030 slope: 0.981 SSIM: 0.986
Input Stronger External χ Dataset	RMSE: 0.0077 slope: -0.000 SSIM: 0.937	RMSE: 0.0076 slope: 0.321 SSIM: 0.940	RMSE: 0.0018 slope: 0.922 SSIM: 0.995

Tab e 11: Losses of the three ANNs compared to the three d fferent ground truth abe s. Output ANN Offset Dataset shows a s ope of zero n case of the Input Stronger Externa χ Dataset because the va ues n the output are a c ose to zero.

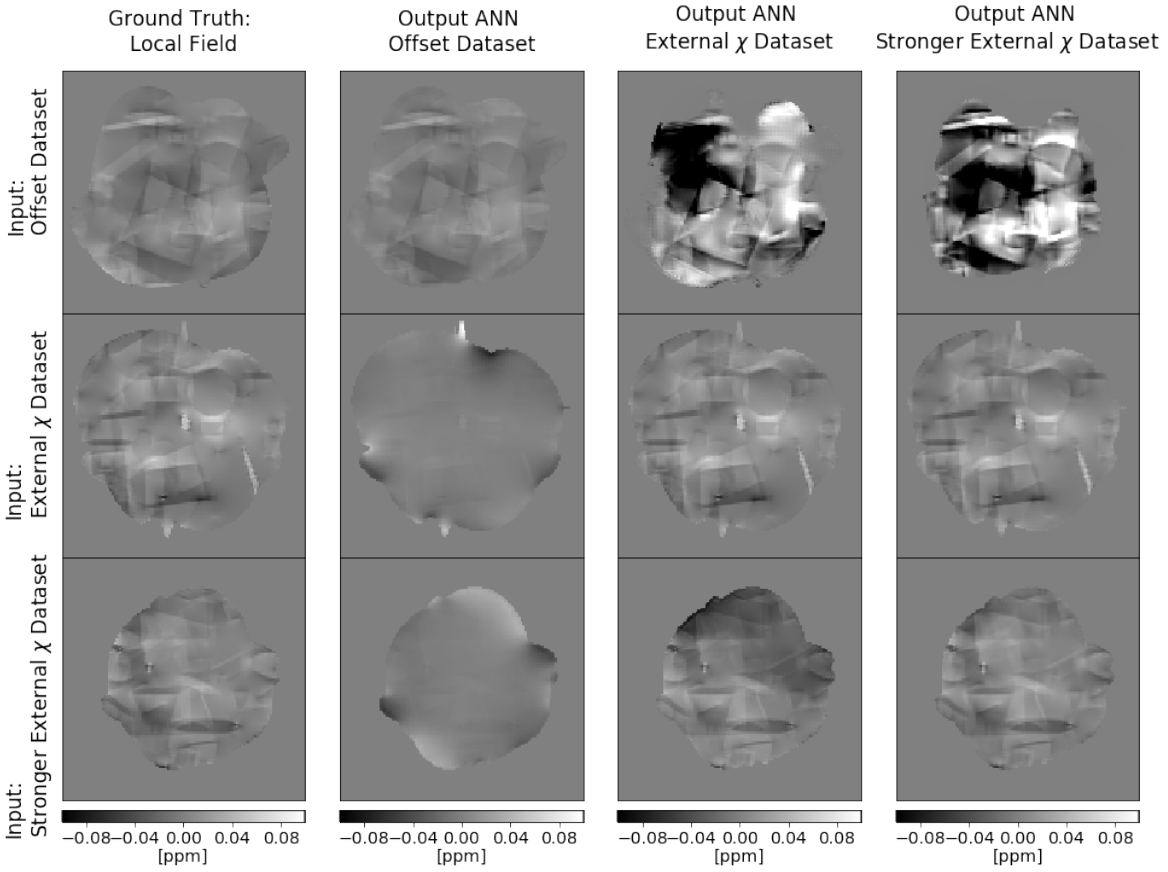

F gure 65: Compar son of performance of three d fferent ANNs that were eva uated w th three d fferent mode nputs.

In the first row, the model input is a validation image of the Dataset Offset. The ANN that was trained with corresponding training data performs well (SSIM of 0.984) and shows only small deviations at the boundaries. ANN External χ Dataset and Model Stronger External χ produce outputs with a higher standard deviation. Through this, the values differ a lot from the ground truth label (SSIM of 0.818 and 0.834). For the input images of the External χ Dataset, the ANN Offset Dataset creates images with too low values. Except from variations close to the boundaries, no objects are

visible. The performance of ANN External χ and Stronger External χ are similar but each Model performs a bit better on the corresponding validation data (see Table 11). For the input image of the Stronger External χ image the corresponding ANN performs better than the ANN External χ. The latter leaves parts of the background field (visible in the Difference Figure 66).

Summarized, each ANN performs best on the corresponding validation data. The differences between Model External χ and Model Stronger External χ are smaller compared to the Model Offset Data. ANN Stronger External χ performs better on the data input of Dataset External χ than the other way around. All differences to the local field ground truth are visible in Figure 66.

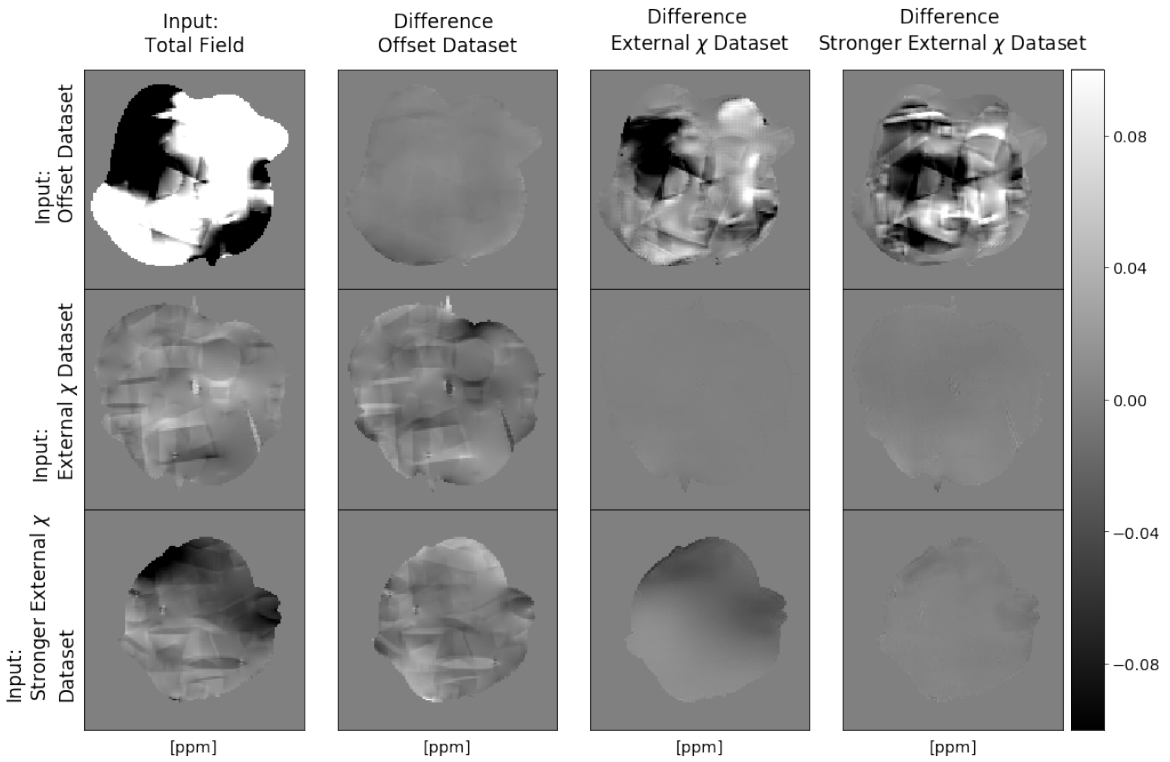

F gure 66: The ANNs show d fferences toward the oca f e d ground truth for the three d fferent nputs n F gure 65.

4.2.2 Evaluation with Numerical Brain Phantom

In this section, the three ANNs were tested with a brain phantom. As described in Section 3.7 the brain phantom was covered with a local field and a background field. In one case, the background field was created by an offset of 0.4 ppm and external susceptibilities, in the other one only by external susceptibility sources. Figure 67 visualizes the results for the three ANNs. In the upper row, the results for the input without offset are shown. In the bottom row the results for the input without offset. As the offset was small compared to the one for synthetic data the ANN Offset Dataset show worse results for the input with offset. This ANN did not remove the background field in both cases. ANN External χ and ANN Stronger External χ reveal brain structures but show strong background field artifacts close to the boundaries. The artifacts are more pronounced in the first mentioned ANN. In Figure 68 the difference between ground truths and ANN outputs are shown.

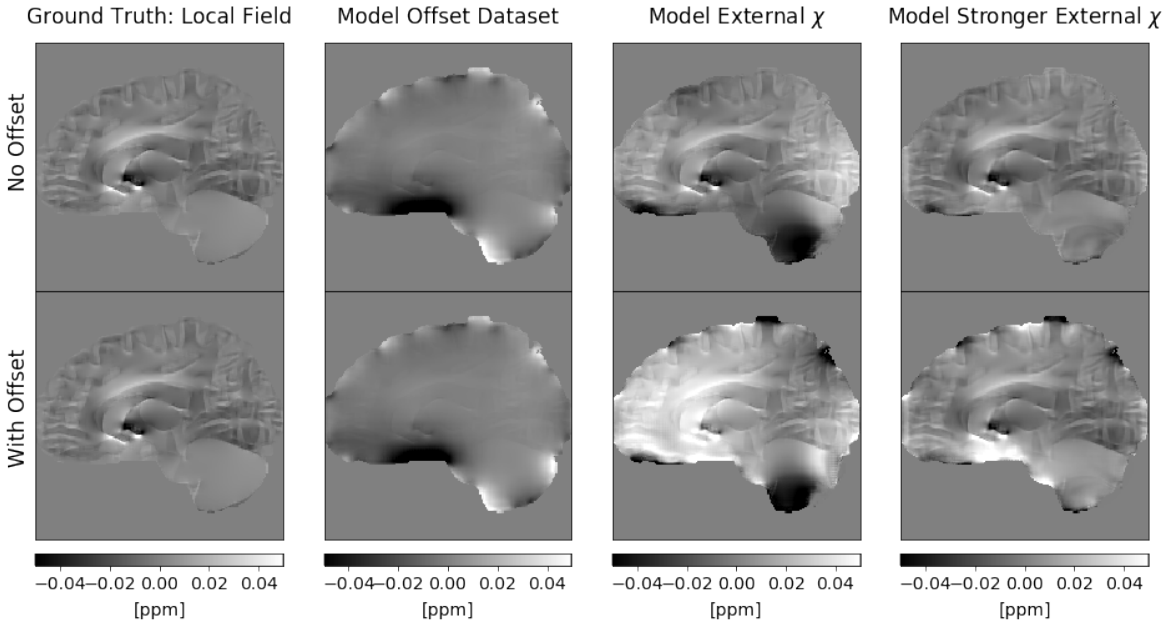

F gure 67: Output of the three d fferent ANNs. The f rst row shows the resu ts for the data nput that had no offset. Here, the background f e d was created on y by externa suscept b ty sources. The second row shows the resu ts of the nput where the background f e d was created by both a sma offset and externa suscept b t es.

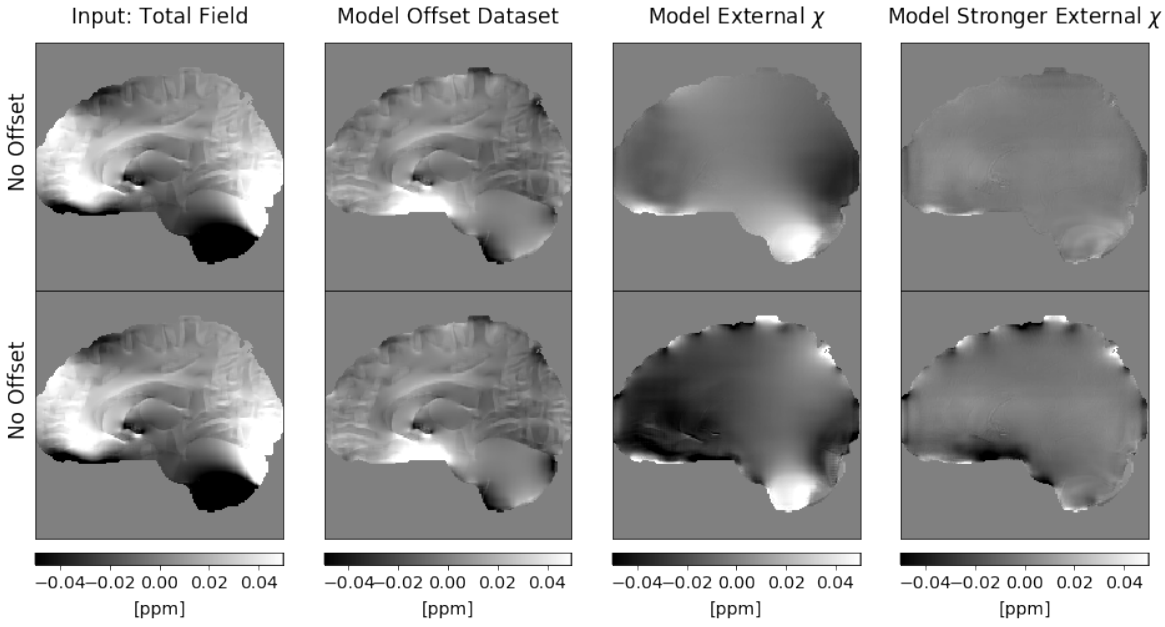

F gure 68: D fference of the ANN outputs n F gure 67 towards the r correspond ng ground truths

Table 12 summarizes the corresponding losses. Here, Model Dataset Offset and Model External χ have similar losses for the input without offset although Model External χ reveals more brain structures. Figure 68 shows that Model Dataset Offset did not remove the background field and Model External χ removes it only partially. Model Stronger External χ shows errors at the boundary and in the area of the cerebellum. The errors are less pronounced in case of the input without offset.

	Model	RMSE	Slope	SSIM
No Offset	Dataset Offset	0.0118	0.215	0.888
	External χ	0.0114	0.474	0.882
	Stronger External χ	0.0031	0.962	0.983
With Off-set	Dataset Offset	0.0109	0.2131	0.895
	External χ	0.0167	0.587	0.782
	Stronger External χ	0.0089	1.061	0.925

Tab e 12: Compar son of the osses for the three d fferent ANNs that were tested w th a numer ca bra n phantom w th added background f e d

ANN Stronger External χ shows the best losses referring RMSE, Slope and SSIM for both inputs.

4.2.3 In-vivo Scan Data

To compare the ANN with the quality of other methods for background field removal, the sepia toolbox (see Section 3.9) was used. Figure 74 shows the results of various algorithms available in sepia that perform background field removal on a given total field input.

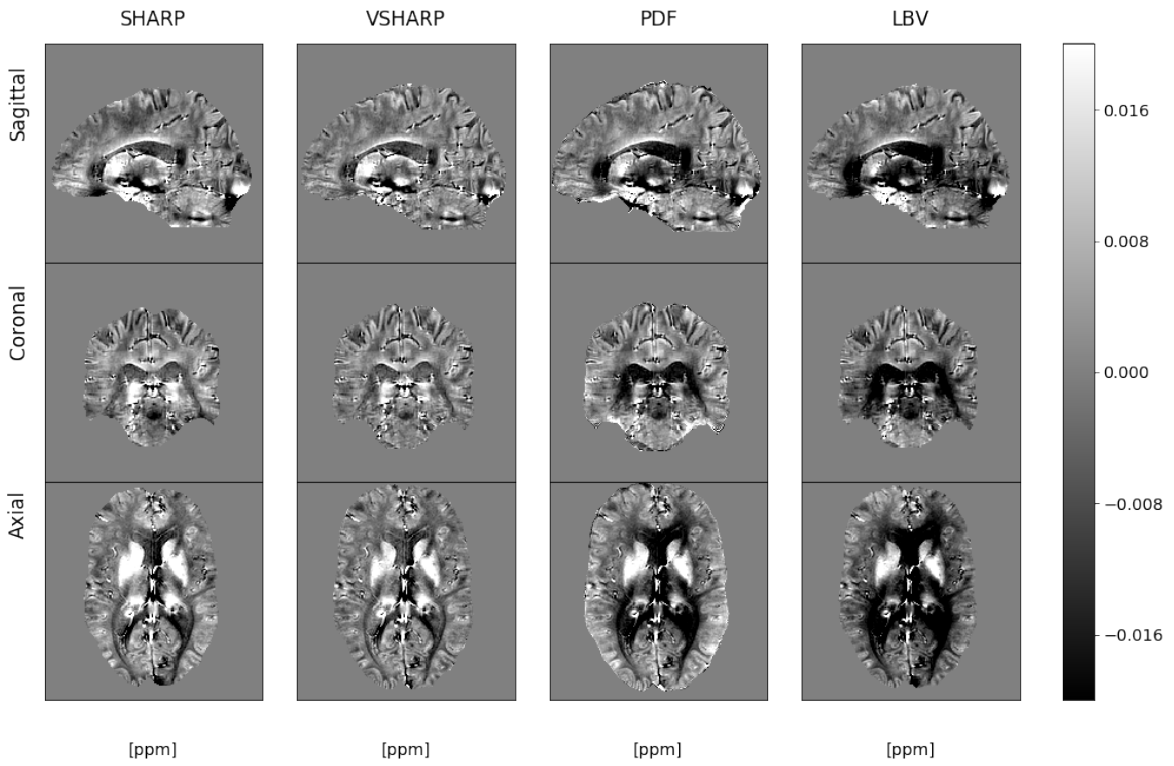

F gure 69: Compar son of d fferent a gor thms for BFR w th the sep a too box.

As expected, the output of SHARP is a bit smaller than the one of VSHARP due to the morphologic erosion at the boundaries. PDF and LBV show high field perturbations in the inner part of the brain. Due to this, the VSHARP algorithm was chosen for further comparisons.

The three models with the same architecture but different datasets for training were compared in Figure 70. Model Offset Dataset still has a strong background field that covers the brain structures. Model External χ still shows background field artifacts but brain structures are visible. Due to this,

the dynamic range differs between the images. Only Model Stronger External χ seems to remove the background field largely and was compared to the results of the VSHARP algorithm.

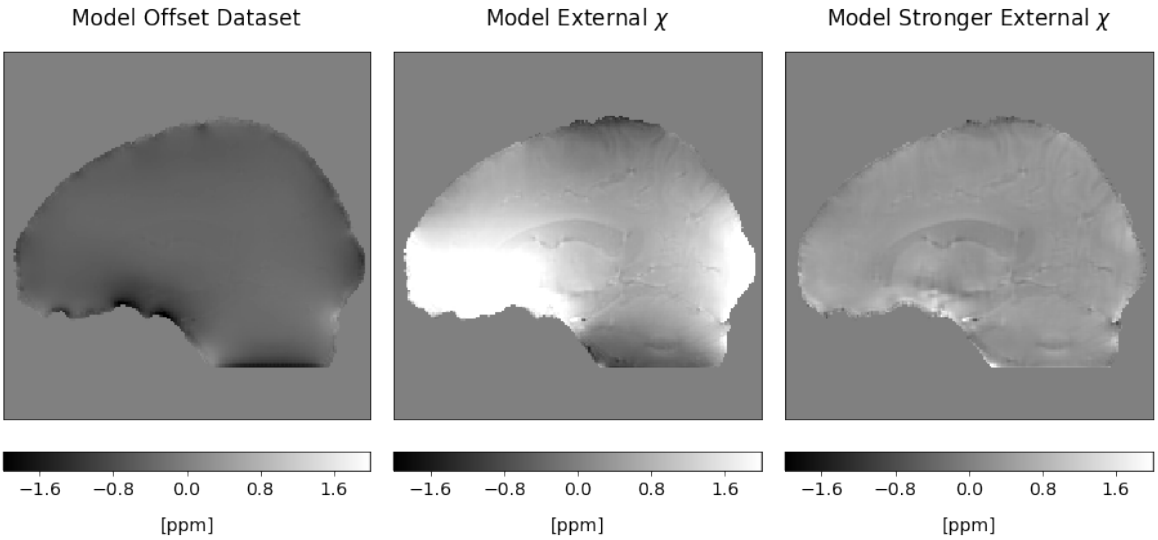

F gure 70: Compar son of the three mode s tra ned w th d fferent datasets and n-v vo tota f e d nput.

Model	RMSE [ppm]	Slope	SSIM
Stroger External χ	0.2142	7.380	0.735

The resulting losses are high compared to the previous ones. The histogram Figure 71 shows that ANN input, ANN output and the created image using VSHARP have a different range of voxel values. While the VSHARP algorithm maps the total field to a tight range around zero, the ANN seems to shift the values, so its mean is at 0.37 ppm.

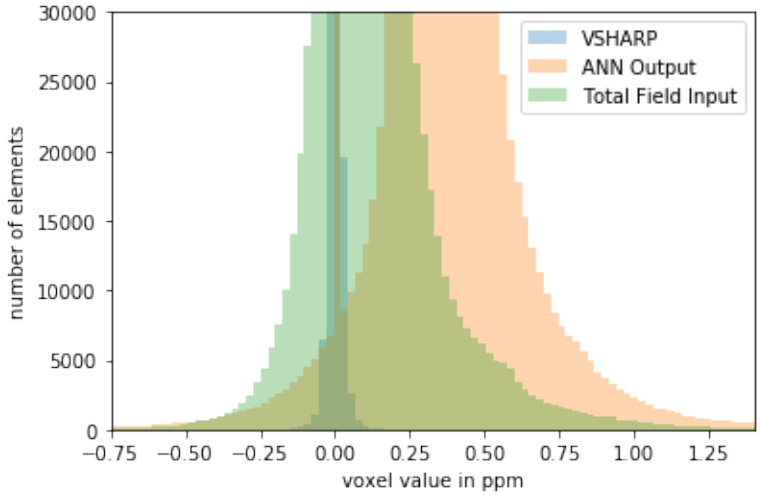

F gure 71: H stogram of ANN nput, ANN output and the output us ng VSHARP. The ANN output s sh fted and has a w der standard dev at on than the VSHARP mage.

For further visual comparisons the ANN output was shifted by -0.37 and scaled with 1/6 while the VSHARP image was multiplied with 10 (displayed in the resulting histogram Figure 72)to make the images comparable.

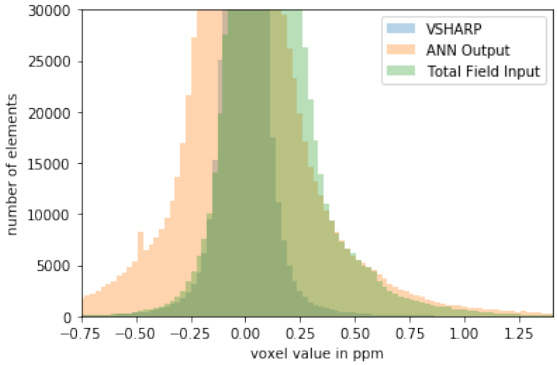

F gure 72: H stogram of sca ed and sh fted ANN output, sca ed VSHARP output and the tota f e d nput.

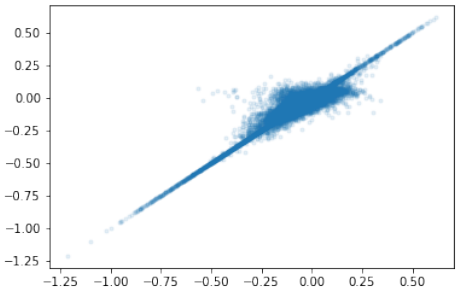

F gure 73: Scatter p ot of sca ed VSHARP and sca d and sh fted ANN output.

Figure 72 shows the results of the scaled and shifted ANN output compared with VSHARP. In the ANN output, brain structures are visible, but parts of the background field remained.

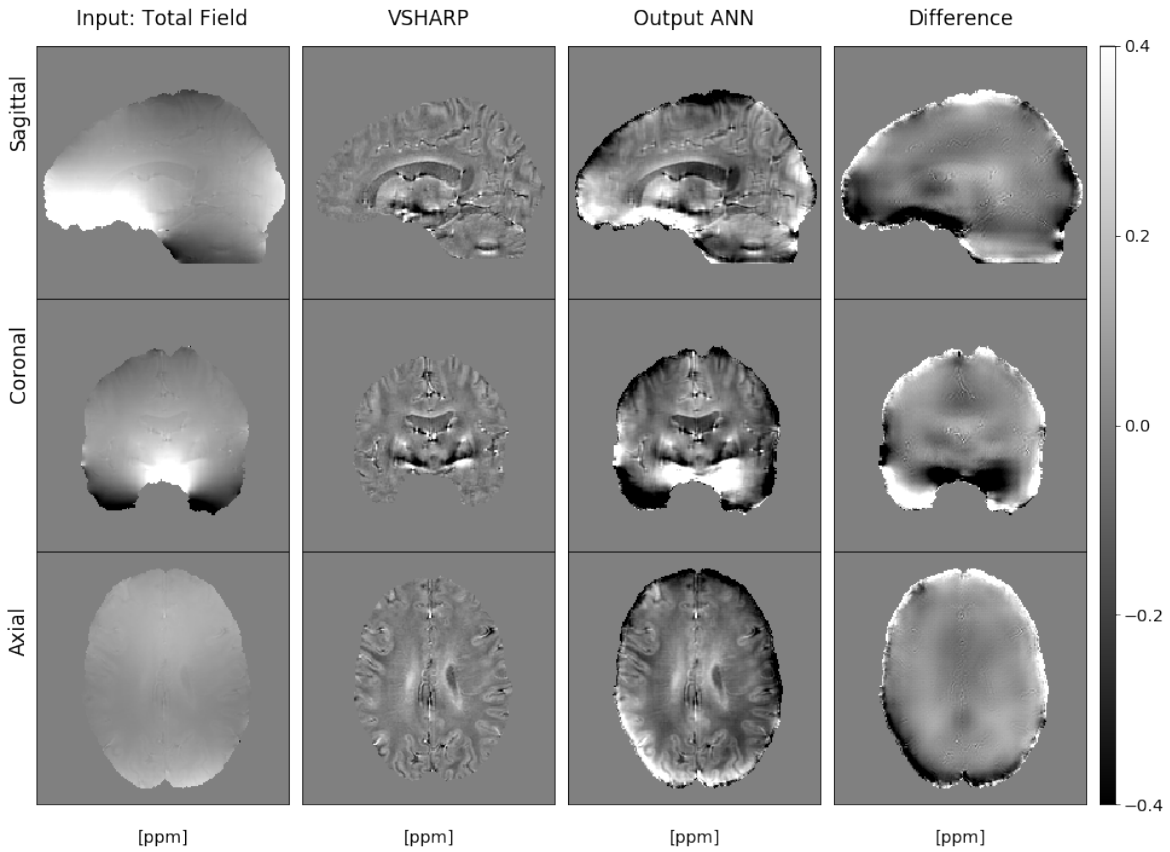

F gure 74: Compar son between VSHARP and ANN output. The mages were sca ed and sh fted before to make them v sua y comparab e. The ANN output shows dev at ons espec a y at the boundar es.

4.2.4 Discussion

The ANNs trained for background field removal were not able to remove background fields in in-vivo data. The dataset that used stronger external susceptibility sources to create the background field showed the best results evaluated with the numerical brain phantom and in-vivo data. However, the ANN output values are shifted and spread compared to the results of the VSHARP algorithm. All three ANNs that were trained with one of the three datasets performed very good if tested with the corresponding validation data. ANN Offset Dataset achieved a SSIM of 0.984, ANN External χ Dataset a SSIM of 0.998 and ANN Stronger External χ Dataset a SSIM of 0.995 (see Table 11). However, the datasets seem not to represent images of in-vivo images. The results of in-vivo inputs show remaining background field artifacts (see Figure 74) and an offset (see Figure 71).

To improve the model performance the datasets should be further fitted to the distributions of in-vivo total fields and in-vivo local field maps (e.g. calculated with VSHARP). The evaluation with input images (see Table 11) showed that ANN Stronger External χ Dataset achieves a SSIM of 0.986 and a RMSE of 0.0030 ppm if tested with validation data of Dataset External χ. In comparison ANN External χ Dataset achieves only a SSIM of 0.940 and a RMSE of 0.0076 ppm if evaluated with Dataset Stronger External χ. The reason could be that the range of external susceptibilities used in Dataset External χ is included in the Dataset Stronger External χ. From this, it can be deduced that the dataset should use both external susceptibility sources and an offset to create background fields with higher variability. Furthermore, both parameters should vary in a wider range.

Another approach would be to preprocess the total field and decrease the dynamic range that the ANN has to learn. This reduction of the background field could be achieved by subtraction with spherical harmonic functions, applying one or two iterations of PDF [26] or by simulating and subtracting it. For the latter case, the strongest sources for background fields (the air-tissue interface of the head and the sinuses) could be reconstructed. By using the dipole kernel, a strong field would be created which could then be subtracted from the total field.

4.3 Results ANN for both Background Field Removal and Dipole Inversion

The previous section focused on BFR with three ANNs trained on different datasets. The input images were the same as in Section 4.2. However, the ANNs tried to map the input total field to a susceptibility map instead of to a local field map. The ANNs were tested on synthetic data, numerical brain phantom and in-vivo scan data.

4.3.1 Synthetic Validation Data

The three ANNs that were trained with the three different datasets were each tested with validation images of the datasets. Figure 75 shows the results while Figure 76 shows the differences to the ground truth labels and Table 13 the corresponding losses.

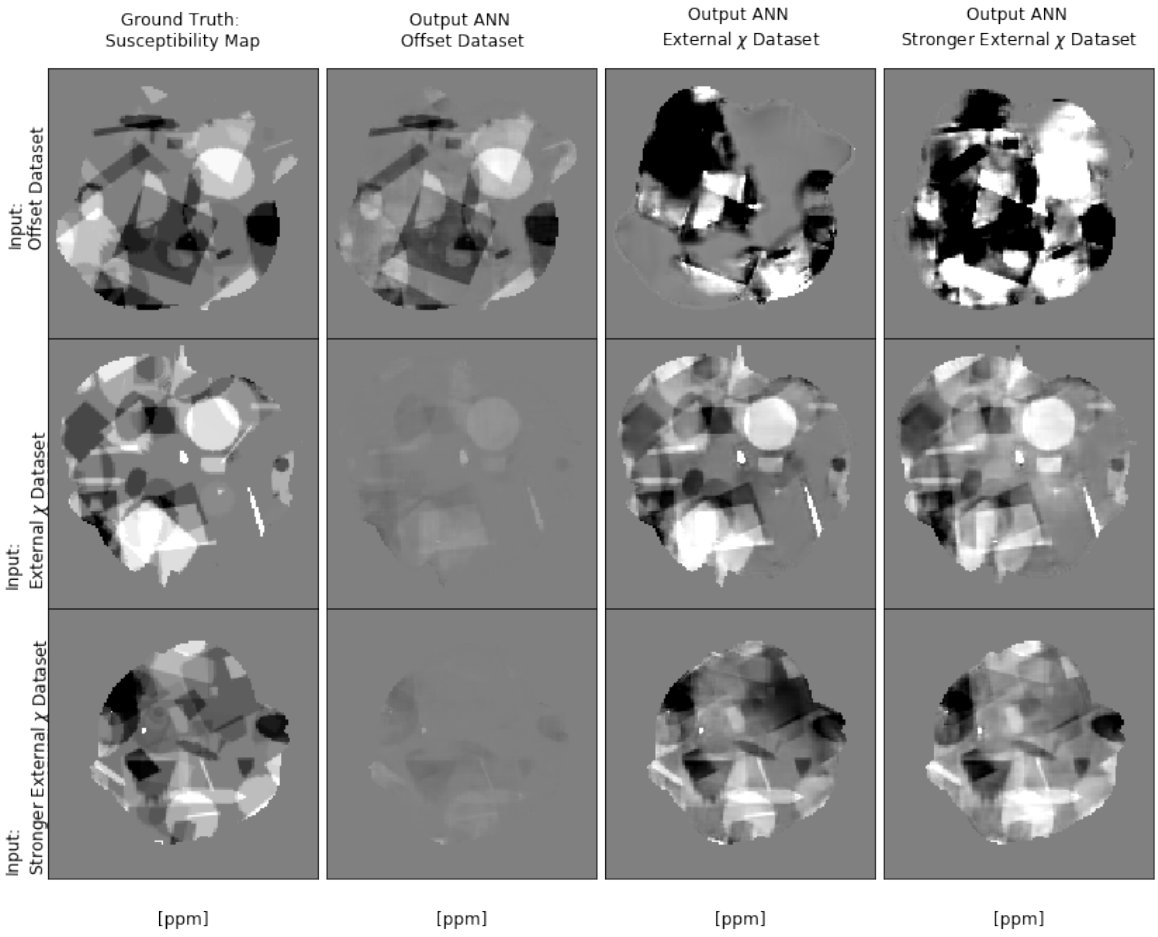

F gure 75: Compar son of performance toward BFR and d po e nvers on n one step of three d fferent ANNs that were eva uated w th three d fferent mode nputs.

The performance between the ANN that was trained with total fields created by an offset differs from the two ANNs that were trained with total fields created by external susceptibilities. The ANN trained with the Offset Dataset performs well on this validation data. It seems be able to remove the background field in the case of the input images that used external susceptibility sources to create the total field. However, the values in the output are smaller than in the ground truth and thereby create high losses (see Table 13). Both ANNs that were trained with (Stronger) External χ

data perform well on the corresponding validation data. However, the losses are worse than in Chapter 4.2, Table 11 and Table 12 where the ANNs had to learn only BFR. Both ANNs show problems when confronted with Offset Dataset inputs: Here the resulting images has a higher standard deviation than the ground truth. The output of ANN External χ Dataset shows problems confronted with the input Offset Dataset. Here, areas where the total field is very negative show values around zero and no structure is visible.

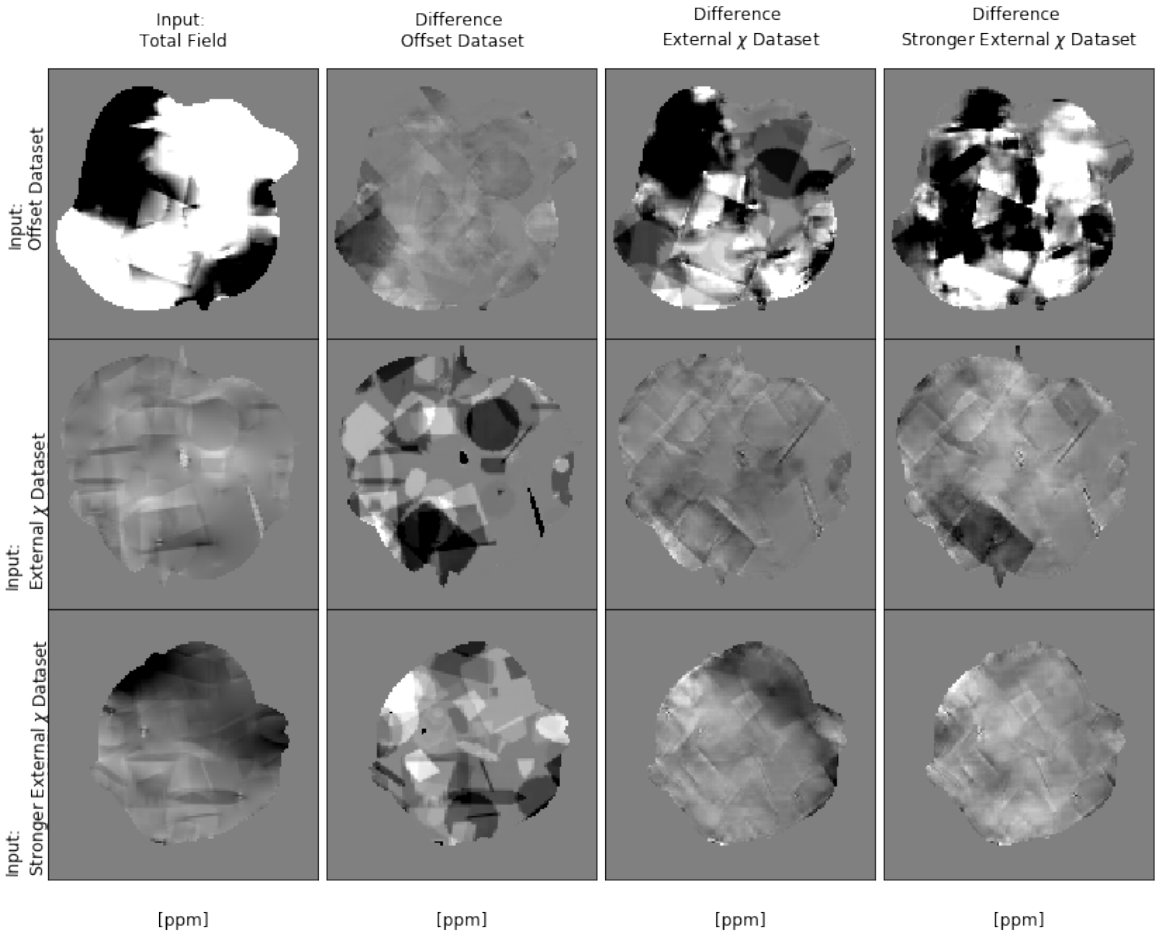

F gure 76: Correspond ng d fferences between mages n F gure 75 and the r suscept b ty ground truth.

	Output ANN Offset Dataset	Output ANN External χ Dataset	Output ANN Stronger External χ Dataset
Input Offset Dataset	RMSE: 0.0111 slope: 1.137 SSIM: 0.949	RMSE: 0.0680 Slope: 0.110 SSIM: 0.702	RMSE: 0.0872 slope: 0.183 SSIM: 0.675
Input External χ Dataset	RMSE: 0.0299 slope: 6.437 SSIM: 0.794	RMSE: 0.0098 slope: 0.989 SSIM: 0.956	RMSE: 0.0135 slope: 0.931 SSIM: 0.924
Input Stronger External χ Dataset	RMSE: 0.0197 slope: 7.083 SSIM: 0.895	RMSE: 0.0164 slope: 0.700 SSIM: 0.937	RMSE: 0.0097 Slope: 0.930 SSIM: 0.953

Tab e 13: Compar son of osses for the var ous ANNs that performed both BFR and d po e nvers on.

4.3.2 Numerical Brain Phantom

The total field of the numerical brain was used as input and converted by the ANNs to a susceptibility distribution. Two total field variations were used for this.

For the upper input in Figure 77, a total field was created using external susceptibilities without adding an offset to the ROI. Model Stronger External χ showed the lowest errors. The other two Models were both a bit worse. However, Figure 78 shows that the losses of both differ spatially. Model Offset Dataset shows very low voxel values with little contrast between the structures. Model External χ shows a higher contrast between the structures but on the other hand has strong background field artifacts. The artifacts of Model Stronger External χ are similar to Model External χ but less pronounced. Both show background artifacts at the boundary of the ROI. None of the Models was able to reconstruct the cerebellum correctly.

In case of the input that used an additional offset to create the total field, no conclusion can be drawn which model performed best because all three losses show a different ranking (see Table 14).

Figure 77, shows the created ANN outputs, Figure 78 the differences towards the ground truth susceptibility map and Table 14 the corresponding losses. Due to the low values of the ANN Output Model Offset Dataset the difference to the ground truth looks like the ground truth itself.

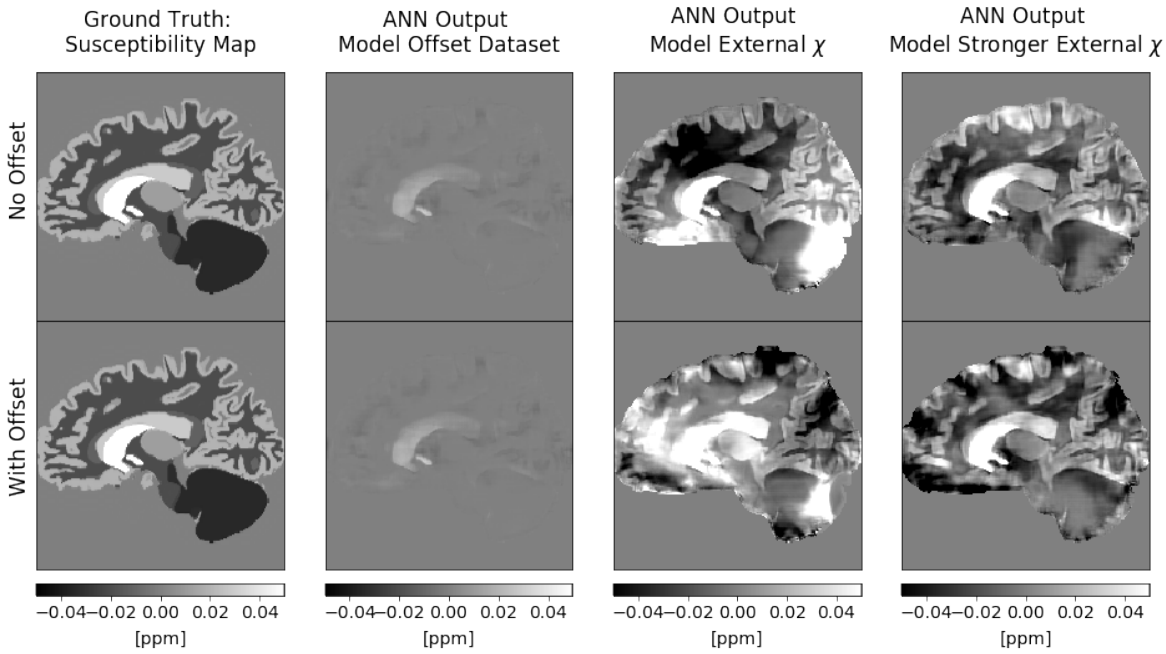

F gure 77: Compar son of performance toward BFR and d po e nvers on n one step of three d fferent ANNs that were eva uated w th two d fferent numer ca bra n phantoms.

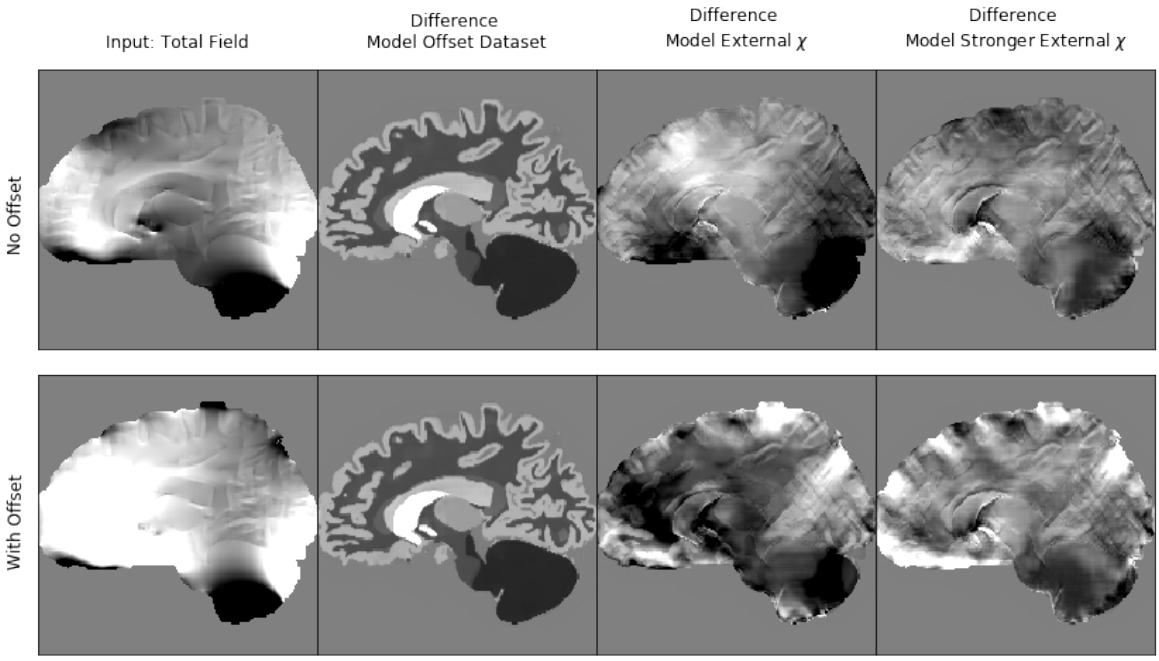

F gure 78: Correspond ng d fferences between mages n F gure 77 and the r suscept b ty ground truth.

	Model	RMSE	Slope	SSIM
No Offset	Dataset Offset	0.0156	0.068	0.833
	External χ	0.0179	0.656	0.840
	Stronger External χ	0.0116	0.784	0.895
With Off-set	Dataset Offset	0.0156	0.068	0.833
	External χ	0.0232	0.683	0.744
	Stronger External χ	0.0201	0.725	0.789

Tab e 14: Correspond ng osses between mages n F gure 77and the r suscept b ty ground truth. In case of the nput w th offset no conc us on can be drawn wh ch mode performed best because a three osses show a d fferent rank ng.

4.3.3 In-vivo Scan Data

Three ANNs that were trained with the different datasets were tested to perform background field removal and dipole in one step on in-vivo data (see Figure 79).

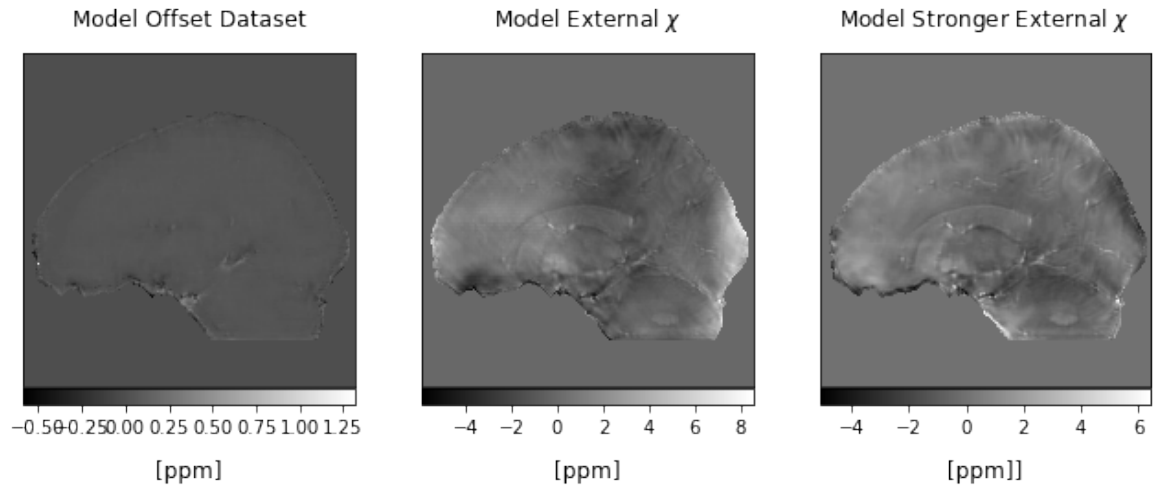

F gure 79: Output of ANNS that map a g ven tota f e d to a suscept b ty d str but on. The three ANNS were tra ned w th d fferent datasets.

The model that was trained with the background field created by an offset was not able to perform both steps of background field removal and dipole inversion. As described in Section 4.3 this dataset was also not suited to perform only background field removal. The two models that used data with external susceptibility sources to create a background field show similar results. However, the Model External χ shows leftovers of background field. For the following evaluations, only Model Stronger External χ was used. The output was compared to two other images: One the one hand, with the susceptibility map created with the VSHARP and STAR-QSM algorithms of the sepia toolbox. One the other hand, with the output of the DeepQSM model that took the output of the model for background field removal as input. The model that was trained for background field removal also used the dataset with strong external susceptibilities. As described in Section 4.3 it showed the best results for background field removal.

Figure 82 compares the results of the VSHARP and STAR-QSM algorithm, the result that used both an ANN for BFR and one for dipole inversion and the result of a single ANN that learn both BFR and dipole. For the two-step solution, the output of the ANN for BFR was used as input for the ANN for dipole inversion. The both output images that used ANNs show susceptibility values with a higher standard deviation than the STAR-QSM algorithm (Figure 80). The histogram shows that the values of the two-step solution are shifted. Due to the shift, the output of the two-step solution was shifted by its mean and evaluated as further comparison (Figure 81). Table 15 shows the losses of both ANN solutions compared to the STAR-QSM algorithm. If the two-step solution was shifted the performance is superior to the one step solution. The one-step solution shows more background field artifacts. However, both ANN outputs look blurred.

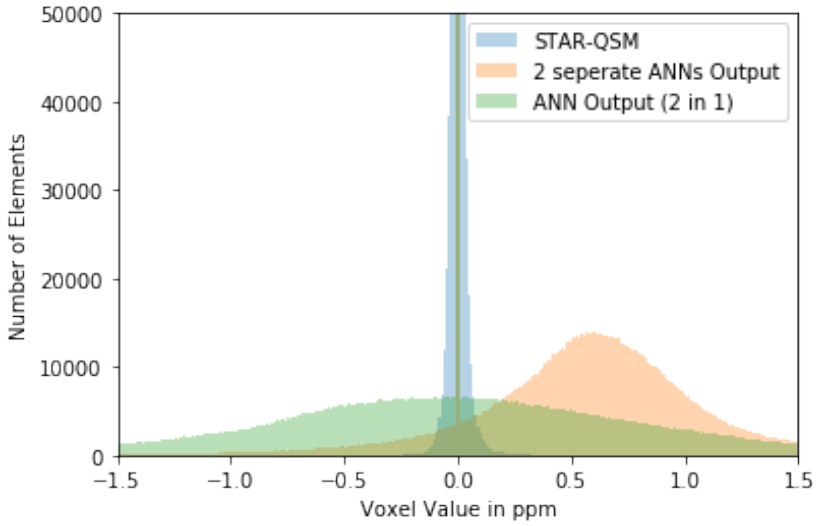

F gure 80: H stogram of STAR-QSM output, output of ANN that performs both BFR and d po e nvers on n one-step and output of the ANN for d po e nvers on that took the output of the ANN for BFR as nput.

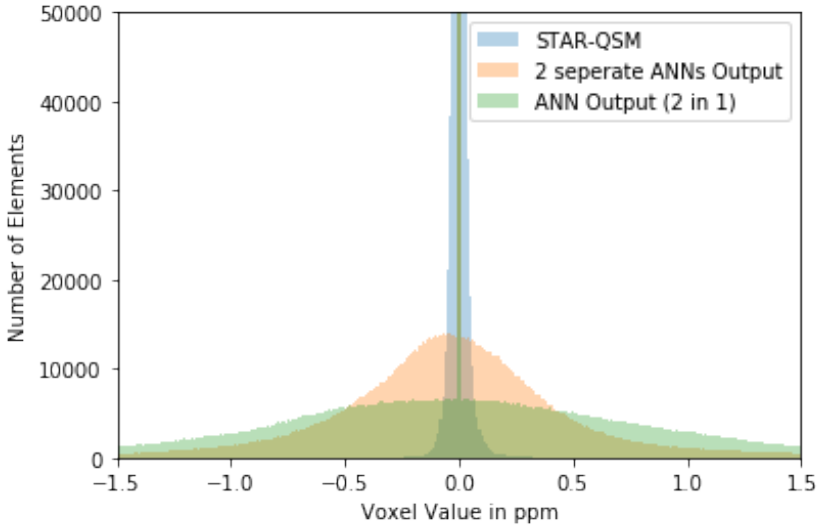

F gure 81: H stogram of STAR-QSM output, sh fted output of ANN that performs both BFR and d po e nvers on n one step and output of the ANN for d po e nvers on that took the output of the ANN for BFR as nput.

	RMSE	slope	SSIM
2 Step Solution: Output ANN 2 Steps	0.4549	0.007	0.732
2 Step Solution Shifted: Output ANN 2 Steps	0.3298	0.012	0.739
1 Step Solution: Output ANN 1 Step	0.5016	0.007	0.733

Tab e 15: Compar son of 1 step and two step so ut on of the ANN outputs compared to STAR-QSM. The two-step so u- t on s eva uated tw ce: Once w thout sh ft ng, once w th sh ft ng.

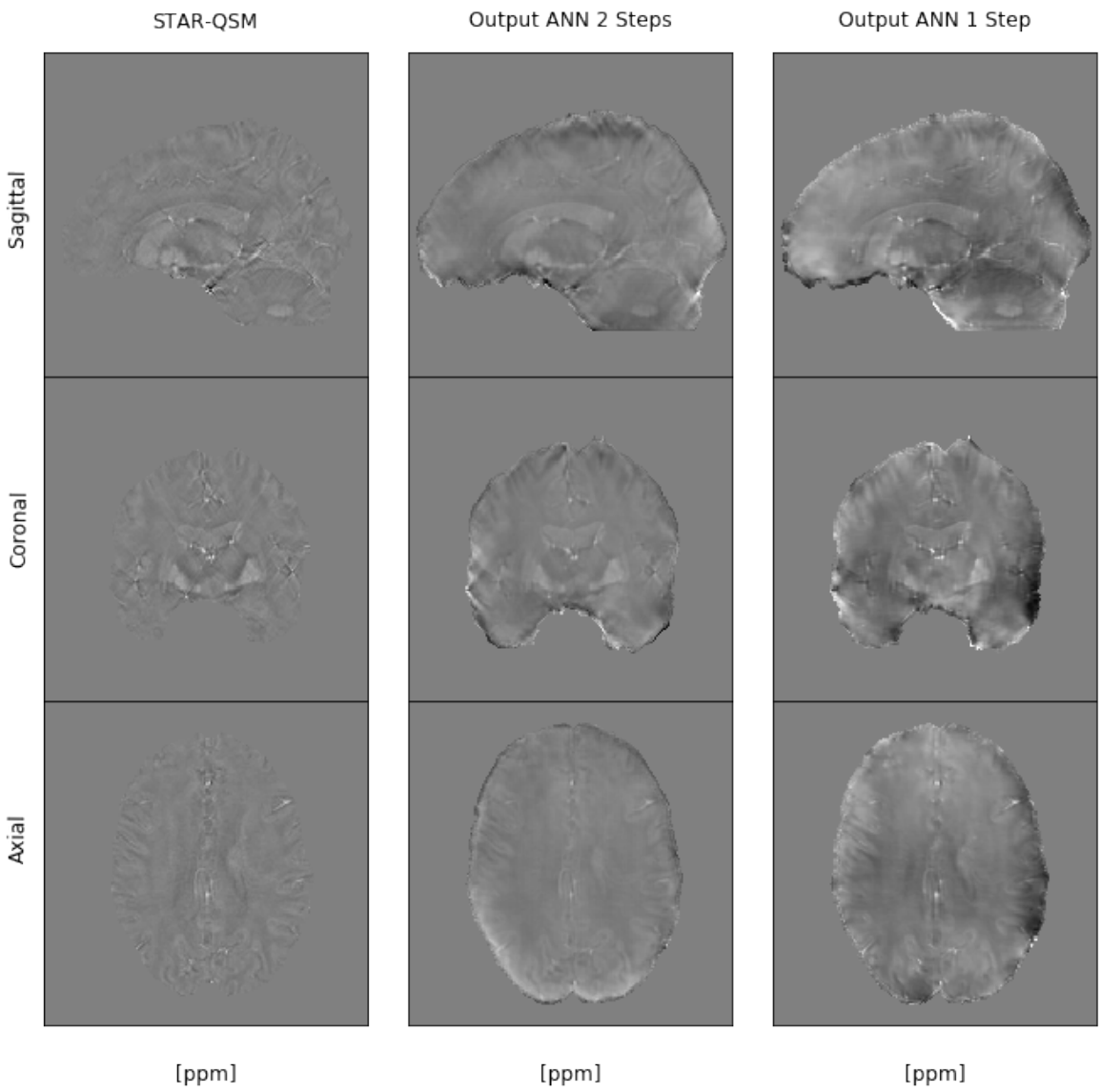

F gure 82: Compar son of the ANN that performs both BFR and d po e nvers on towards the output of the ANN for d - po e nvers on that used the output of the ANN for BFR as nput. The Output ANN two-steps was sh fted to substract the offset n the output.

4.3.4 Discussion

The modified DeepQSM architecture with two input channels was evaluated towards its ability to map a given total field to the corresponding susceptibility distribution. Due to the same ANN input, the results are similarly to the results of Section 4.2.

All three ANNs that were trained with one of the three datasets described in Section 3.5 (data creation for BFR) performed very good if tested with the corresponding validation data. The results were worse if tested with validation data of the other datasets (Table 13). The ANN that used Dataset Stronger External χ performed best if tested with the numerical brain phantom. Testing with in-vivo data, all ANNs showed effects of incompletely removed background fields (Figure 79). Here, the dataset that used stronger external susceptibility sources to create the background field showed the best results (Figure 75, Figure 76, Table 13). Tested with in-vivo data, the resulting ANN

output values had a larger standard deviation compared to the results of the VSHARP algorithm combined with STAR-QSM (see Figure 80). As described in the discussion of Section 4.2, the dataset has to be adjusted to better reflect the distribution of in-vivo data.

Finally, the ANN that performs both BFR and dipole inversion in one-step was compared with a two-step solution that uses two separate ANNs for BFR and dipole inversion. Here, the two-step ANN created an offset that was subtracted. The subtracted image version showed slightly superior results towards the one-step solution referring the RMSE (0.5016 ppm vs. 0.4549 ppm) and SSIM (0.732 vs 0.733, see Table 15). Furthermore, less background field artifacts were visible than in the image of the one-step solution (see Figure 80). In the two-step solution, the ANN for dipole inversion did not gain the remaining artifacts. Instead, it could be possible that the ANN for dipole inversion improved the result by removing leftovers of the background field. As the differences between the losses were small, it cannot be excluded that a one-step solution might be better if trained with other data. The results suggest that the network has sufficient parameters to internalize both steps; otherwise the differences in the losses between one and two-step solution should be higher.

5 Conclusion

In this thesis, fully convolutional neural networks were investigated towards their ability to solve the inverse problems of dipole inversion and background field removal. The excellent performance in dipole inversion of the DeepQSM architecture on in-vivo data demonstrates the potential of convolutional neural networks for QSM. The ANN seems visually comparable to established algorithms for dipole inversion like QSM-STAR (see Section 4.1.5, see Figure 61). However, the use of different datasets for training has influences on the created output values of the ANN. Datasets that consisted of geometric objects with the same standard deviation but of different sizes and in presence of additional small objects led to slightly different susceptibility values in the ANN output, although the same input images were used (see Figure 44). Compared to the investigated changes of the cost function, the dataset had more influence on the resulting images (see Figure 44). As in case of in-vivo data no ground truth label exists, further investigations are necessary to determine which dataset for training creates the most realistic susceptibility values.

In case of the ANNs for background field removal, the results showed distinct leftovers of the background field (see Figure 74, Figure 82). The intensity of artifacts depended on the used dataset. Thus, one can conclude that the dataset should be further improved. The distribution of image values should be adjusted to the values in MR images of total fields, local fields or susceptibility maps. Furthermore, it is important to include images showing pathological values. Otherwise, the trained ANN would under or overestimate such values later [92]. Furthermore, more variations in creating the background field should be used. Instead of using a fixed offset or strong external susceptibilities in a certain range to create an external field, both approaches should be represented in the used dataset. Additionally, the values of both offset and external susceptibility sources should vary in a wider range.

To make it easier for the ANN to learn the BFR, a pre-processing of the total field image would be conceivable. This would bring the order of magnitude of the total field closer to those of the local field. Possible methods to solve this problem would be spherical harmonic function [48], projection into dipole field [26] or the reconstruction and subtraction of an approximated total field produced by the convolution of the dipole kernel with a given air-tissue interfaces.

Another way to improve the performance of ANNs for BFR and/or dipole inversion could be the use of a second ANN input channel for the magnitude images. Like the dipole inversion method MEDI [21], the ANN could use the information of the magnitude image to regularize the corresponding phase image.

In the last chapter, the performance of an ANN that executes BFR and dipole inversion in one step was compared to the performance of two separate ANNs for this. Here, the two-step ANN was

superior, as remaining background field artifacts were not intensified in the following ANN but rather attenuated.

The dataset in this thesis was adapted to susceptibility values in the brain, an isotropic resolution and a direction of the magnetic field B_0 in z-direction. The trained ANNs cannot process phase images that do not fulfill these properties. However, as the use of synthetic data enables an unlimited amount of training data these restrictions can be overcome by creating corresponding data.

In summary, the reconstructed DeepQSM for dipole inversion shows promising results that are comparable to established methods. Further experiments should compare the created susceptibility values with real ones that are known by experiments or theoretical calculations. The dataset that creates images that comes closest to these values should be chosen. The tested ANNs for BFR or BFR and dipole inversion showed strong remaining background field artifacts. To improve the performance, the dataset should be adjusted to better match in-vivo data. If the ANN for BFR shows good results, the ANN can be extended to perform both BFR and dipole inversion in a single step.

Bibliography

1. Marques JP, Bowtell R. Application of a Fourier-based method for rapid calculation of field inhomogeneity due to spatial variation of magnetic susceptibility. Concepts Magn Reson Part B Magn Reson Eng. 2005;25B(1):65 78.
2. Wang Y. Quantitative Susceptibility Mapping: Magnetic Resonance Imaging of Tissue Magnetism. Createspace Independent Pub; 2013.
3. Rasmussen KGB, Kristensen M, Blendal RG, Østergaard LR, Plocharski M, O'Brien K, et al. DeepQSM - Using Deep Learning to Solve the Dipole Inversion for MRI Susceptibility Mapping. bioRxiv. 2018 Mar 7;278036.
4. Yoon J, Gong E, Chatnuntawech I, Bilgic B, Lee J, Jung W, et al. Quantitative susceptibility mapping using deep neural network: QSMnet. NeuroImage. 2018 01;179:199 206.
5. Ronneberger O, Fischer P, Brox T. U-Net: Convolutional Networks for Biomedical Image Segmentation. In: Navab N, Hornegger J, Wells WM, Frangi AF, editors. Medical Image Computing and Computer-Assisted Intervention MICCAI 2015. Springer International Publishing; 2015. p. 234 41. (Lecture Notes in Computer Science).
6. Klohs J, Deistung A, Schweser F, Grandjean J, Dominietto M, Waschkies C, et al. Detection of cerebral microbleeds with quantitative susceptibility mapping in the ArcAbeta mouse model of cerebral amyloidosis. J Cereb Blood Flow Metab. 2011 Dec;31(12):2282 92.
7. Zhang Y, Gauthier SA, Gupta A, Comunale J, Chia-Yi Chiang G, Zhou D, et al. Longitudinal change in magnetic susceptibility of new enhanced multiple sclerosis (MS) lesions measured on serial quantitative susceptibility mapping (QSM). J Magn Reson Imaging JMRI. 2016 Aug;44(2):426 32.
8. Wisnieff C, Ramanan S, Olesik J, Gauthier S, Wang Y, Pitt D. Quantitative susceptibility mapping (QSM) of white matter multiple sclerosis lesions: interpreting positive susceptibility and the presence of iron. Magn Reson Med. 2015 Aug;74(2):564 70.
9. Acosta-Cabronero J, Williams GB, Cardenas-Blanco A, Arnold RJ, Lupson V, Nestor PJ. In vivo quantitative susceptibility mapping (QSM) in Alzheimer's disease. PloS One. 2013 Nov 21;8(11):e81093 e81093.
10. O'Callaghan J, Holmes H, Powell N, Wells J, Ismail O, Harrison I, et al. Tissue magnetic susceptibility mapping as a marker of tau pathology in Alzheimer's disease. NeuroImage. 2017 Aug 1;159.
11. Moon Y, Han S-H, Moon W-J. Patterns of Brain Iron Accumulation in Vascular Dementia and Alzheimer's Dementia Using Quantitative Susceptibility Mapping Imaging. J Alzheimers Dis JAD. 2016 Feb 18;51.

12. Eskreis-Winkler S, Deh K, Gupta A, Liu T, Wisnieff C, Jin M, et al. Multiple sclerosis lesion geometry in quantitative susceptibility mapping (QSM) and phase imaging. J Magn Reson Imaging JMRI. 2015 Jul;42(1):224 9.
13. Wiggermann V, Hametner S, Hernández-Torres E, Kames C, Endmayr V, Kasprian G, et al. Susceptibility-sensitive MRI of multiple sclerosis lesions and the impact of normal-appearing white matter changes. NMR Biomed. 2017 Aug;30(8).
14. Acosta-Cabronero J, Cardenas-Blanco A, Betts MJ, Butryn M, Valdes-Herrera JP, Galazky I, et al. The whole-brain pattern of magnetic susceptibility perturbations in Parkinson's disease. Brain J Neurol. 2017;140(1):118 31.
15. Langkammer C, Pirpamer L, Seiler S, Deistung A, Schweser F, Franthal S, et al. Quantitative Susceptibility Mapping in Parkinson's Disease. PloS One. 2016;11(9):e0162460.
16. Du G, Liu T, Lewis MM, Kong L, Wang Y, Connor J, et al. Quantitative Susceptibility Mapping of the Midbrain in Parkinson's Disease. Mov Disord Off J Mov Disord Soc. 2016 Mar;31(3):317 24.
17. Alkemade A, de Hollander G, Keuken MC, Schäfer A, Ott DVM, Schwarz J, et al. Comparison of T2*-weighted and QSM contrasts in Parkinson's disease to visualize the STN with MRI. PLoS ONE [Internet]. 2017 Apr 19 [cited 2019 Jul 3];12(4). Available from: https://www.ncbi.nlm.nih.gov/pmc/articles/PMC5397046/
18. Guan X, Xu X, Zhang M. Region-Specific Iron Measured by MRI as a Biomarker for Parkinson's Disease. Neurosci Bull. 2017 May 17;33(5):561 7.
19. Liu T, Surapaneni K, Lou M, Cheng L, Spincemaille P, Wang Y. Cerebral microbleeds: burden assessment by using quantitative susceptibility mapping. Radiology. 2012 Jan;262(1):269 78.
20. Shmueli K, de Zwart JA, van Gelderen P, Li T-Q, Dodd SJ, Duyn JH. Magnetic Susceptibility Mapping of Brain Tissue In Vivo Using MRI Phase Data. Magn Reson Med Off J Soc Magn Reson Med Soc Magn Reson Med. 2009 Dec;62(6):1510 22.
21. Liu Z, Spincemaille P, Yao Y, Zhang Y, Wang Y. MEDI+0: Morphology enabled dipole inversion with automatic uniform cerebrospinal fluid zero reference for quantitative susceptibility mapping. Magn Reson Med. 2018;79(5):2795 803.
22. Wharton S, Schäfer A, Bowtell R. Susceptibility mapping in the human brain using threshold-based k-space division. Magn Reson Med. 2010 May;63(5):1292 304.
23. Liu T, Spincemaille P, de Rochefort L, Kressler B, Wang Y. Calculation of susceptibility through multiple orientation sampling (COSMOS): a method for conditioning the inverse problem from measured magnetic field map to susceptibility source image in MRI. Magn Reson Med. 2009 Jan;61(1):196 204.
24. Wei H, Dibb R, Zhou Y, Sun Y, Xu J, Wang N, et al. Streaking artifact reduction for quantitative

susceptibility mapping of sources with large dynamic range. NMR Biomed. 2015 Oct;28(10):1294–303.

25. Zhou D, Liu T, Spincemaille P, Wang Y. Background field removal by solving the Laplacian boundary value problem. NMR Biomed. 2014;27(3):312–9.
26. Liu T, Khalidov I, de Rochefort L, Spincemaille P, Liu J, Tsiouris AJ, et al. A novel background field removal method for MRI using projection onto dipole fields (PDF). NMR Biomed. 2011 Nov;24(9):1129–36.
27. Schweser F, Deistung A, Lehr BW, Reichenbach JR. Quantitative imaging of intrinsic magnetic tissue properties using MRI signal phase: an approach to in vivo brain iron metabolism? NeuroImage. 2011 Feb 14;54(4):2789–807.
28. Bollmann S, Kristensen MH, Larsen MS, Olsen MV, Pedersen MJ, Østergaard LR, et al. SHARQnet—Sophisticated harmonic artifact reduction in quantitative susceptibility mapping using a deep convolutional neural network. Z Für Med Phys. 2019 May 1;29(2):139–49.
29. Rasouli J, Ramdhani R, Panov FE, Dimov A, Zhang Y, Cho C, et al. Utilization of Quantitative Susceptibility Mapping for Direct Targeting of the Subthalamic Nucleus During Deep Brain Stimulation Surgery. Oper Neurosurg. 2018 Apr 1;14(4):412–9.
30. van Bergen JMG, Hua J, Unschuld PG, Lim I a. L, Jones CK, Margolis RL, et al. Quantitative Susceptibility Mapping Suggests Altered Brain Iron in Premanifest Huntington Disease. AJNR Am J Neuroradiol. 2016 May;37(5):789–96.
31. Costagli M, Donatelli G, Biagi L, Caldarazzo Ienco E, Siciliano G, Tosetti M, et al. Magnetic susceptibility in the deep layers of the primary motor cortex in Amyotrophic Lateral Sclerosis. NeuroImage Clin. 2016 May 2;12:965–9.
32. Oshiro S, Morioka MS, Kikuchi M. Dysregulation of iron metabolism in Alzheimer's disease, Parkinson's disease, and amyotrophic lateral sclerosis. Adv Pharmacol Sci. 2011;2011:378278.
33. Fritzsch D, Reiss-Zimmermann M, Trampel R, Turner R, Hoffmann K-T, Schäfer A. Seven-tesla magnetic resonance imaging in Wilson disease using quantitative susceptibility mapping for measurement of copper accumulation. Invest Radiol. 2014 May;49(5):299–306.
34. Wang Y, Spincemaille P, Liu Z, Dimov A, Deh K, Li J, et al. Clinical quantitative susceptibility mapping (QSM): Biometal imaging and its emerging roles in patient care. J Magn Reson Imaging JMRI. 2017;46(4):951–71.
35. Brown RW, Cheng Y-CN, Haacke EM, Thompson MR, Venkatesan R. Magnetic Resonance Imaging: Physical Principles and Sequence Design. John Wiley & Sons; 2014. 1790 p.
36. Dössel O, Buzug TM. Band 7 Medizinische Bildgebung. Berlin, Boston: De Gruyter; 2014.
37. Chavhan GB, Babyn PS, Thomas B, Shroff MM, Haacke EM. Principles, techniques, and applications of T2*-based MR imaging and its special applications. Radiogr Rev Publ Radiol Soc N Am

Inc. 2009 Oct;29(5):1433 49.

38. Gradient Echo (GRE) [Internet]. Questions and Answers in MRI. [cited 2019 Jul 4]. Available from: http://mriquestions.com/gradient-echo.html
39. Multi-echo GRE [Internet]. Questions and Answers in MRI. [cited 2019 Jul 4]. Available from: http://mriquestions.com/multi-echo-gre.html
40. Glick RE. ON THE DIAMAGNETIC SUSCEPTIBILITY OF GASES1. J Phys Chem. 1961 Sep 1;65(9):1552 5.
41. Quantitative susceptibility mapping. In: Wikipedia [Internet]. 2018 [cited 2019 Jul 2]. Available from: https://en.wikipedia.org/wiki/Quantitative_susceptibility_mapping
42. Schenck JF. The role of magnetic susceptibility in magnetic resonance imaging: MRI magnetic compatibility of the first and second kinds. Med Phys. 1996 Jun;23(6):815 50.
43. Özbay PS. Quantitative susceptibility mapping (QSM): progress and brain applications [Internet] [Doctoral Thesis]. ETH Zurich; 2016 [cited 2019 Jul 2]. Available from: https://doi.org/10.3929/ethz-a-010802279
44. Olsson E. MRI-based quantification of magnetic susceptibility: Assessment of measurement and calculation accuracy. 2016 [cited 2019 Jul 2]; Available from: http://lup.lub.lu.se/student-papers/record/8897910
45. Salomir R, Senneville BD de, Moonen CT. A fast calculation method for magnetic field inhomogeneity due to an arbitrary distribution of bulk susceptibility. Concepts Magn Reson Part B Magn Reson Eng. 2003;19B(1):26 34.
46. Khabipova D. Quantitative Susceptibility Mapping in the Human Brain [Internet]. 2016 [cited 2019 Jul 2]. Available from: http://dx.doi.org/10.5075/epfl-thesis-7050
47. Sun H. Quantitative Susceptibility Mapping in Human Brain: Methods Development and Applications [Internet]. 2015 [cited 2019 Jul 2]. Available from: https://era.library.ualberta.ca/items/9fca9424-2918-4b65-a4f6-07d30bf99e0c
48. Schweser F, Robinson SD, de Rochefort L, Li W, Bredies K. An illustrated comparison of processing methods for phase MRI and QSM: removal of background field contributions from sources outside the region of interest. NMR Biomed. 2017 Apr;30(4).
49. Haacke EM, Xu Y, Cheng Y-CN, Reichenbach JR. Susceptibility weighted imaging (SWI). Magn Reson Med. 2004 Sep;52(3):612 8.
50. Finnerty E. The implementation and application of quantitative susceptibility mapping in the pre-clinical liver [Internet] [Doctoral]. UCL (University College London); 2018 [cited 2019 Jul 3]. Available from: http://discovery.ucl.ac.uk/10045958/
51. Feng X. Development and evaluation of a novel framework for subcortical gray matter segmentation using quantitative magnetic susceptibility and R2* mapping [Internet]. 2018 [cited

2019 Jul 3]. Available from: https://doi.org/10.22032/dbt.34558

52. Sun H, Wilman AH. Background field removal using spherical mean value filtering and Tikhonov regularization. Magn Reson Med. 2014 Mar;71(3):1151 7.
53. Li W, Wu B, Liu C. Quantitative susceptibility mapping of human brain reflects spatial variation in tissue composition. NeuroImage. 2011 Apr 15;55(4):1645 56.
54. Wang Y, Liu T. Quantitative susceptibility mapping (QSM): Decoding MRI data for a tissue magnetic biomarker. Magn Reson Med. 2015 Jan;73(1):82 101.
55. Russakovsky O, Deng J, Su H, Krause J, Satheesh S, Ma S, et al. ImageNet Large Scale Visual Recognition Challenge. Int J Comput Vis. 2015 Dec 1;115(3):211 52.
56. Szegedy C, Wei Liu, Yangqing Jia, Sermanet P, Reed S, Anguelov D, et al. Going deeper with convolutions. In: 2015 IEEE Conference on Computer Vision and Pattern Recognition (CVPR). 2015. p. 1 9.
57. He K, Zhang X, Ren S, Sun J. Deep Residual Learning for Image Recognition. In: 2016 IEEE Conference on Computer Vision and Pattern Recognition (CVPR). 2016. p. 770 8.
58. Lecun Y, Bottou L, Bengio Y, Haffner P. Gradient-based learning applied to document recognition. Proc IEEE. 1998 Nov;86(11):2278 324.
59. Russell SJ, Norvig P, Davis E. Artificial intelligence: a modern approach. 2010.
60. ILSVRC2017 [Internet]. [cited 2019 Jul 3]. Available from: http://image-net.org/challenges/LSVRC/2017/index
61. Sainath TN, Vinyals O, Senior A, Sak H. Convolutional, Long Short-Term Memory, fully connected Deep Neural Networks. In: 2015 IEEE International Conference on Acoustics, Speech and Signal Processing (ICASSP). 2015. p. 4580 4.
62. Cybenko G. Approximation by Superpositions of a Sigmoidal Function. 1989.
63. Krizhevsky A, Sutskever I, Hinton GE. Imagenet classification with deep convolutional neural networks. In: Advances in Neural Information Processing Systems. p. 2012.
64. CS231n Convolutional Neural Networks for Visual Recognition [Internet]. [cited 2019 Jul 3]. Available from: http://cs231n.github.io/neural-networks-1/
65. Gron A. Hands-On Machine Learning with Scikit-Learn and TensorFlow: Concepts, Tools, and Techniques to Build Intelligent Systems. 1st ed. O'Reilly Media, Inc.; 2017.
66. Bottou L. Large-scale machine learning with stochastic gradient descent. In: in COMPSTAT. 2010.
67. Mei S, Montanari A, Nguyen P-M. A mean field view of the landscape of two-layer neural networks. Proc Natl Acad Sci U S A. 2018 Aug 14;115(33):E7665 71.
68. Kingma DP, Ba J. Adam: A Method for Stochastic Optimization. ArXiv14126980 Cs [Internet]. 2014 Dec 22 [cited 2019 Jul 3]; Available from: http://arxiv.org/abs/1412.6980

69. LeCun YA, Bottou L, Orr GB, Müller K-R. Efficient BackProp. In: Montavon G, Orr GB, Müller K-R, editors. Neural Networks: Tricks of the Trade: Second Edition [Internet]. Berlin, Heidelberg: Springer Berlin Heidelberg; 2012 [cited 2019 Jul 3]. p. 9 48. (Lecture Notes in Computer Science). Available from: https://doi.org/10.1007/978-3-642-35289-8_3
70. Lindeberg T. A computational theory of visual receptive fields. Biol Cybern. 2013 Dec 1;107(6):589 635.
71. neural networks - About CNN, kernels and scale/rotation invariance [Internet]. Cross Validated. [cited 2019 Jul 4]. Available from: https://stats.stackexchange.com/questions/239076/about-cnn-kernels-and-scale-rotation-invariance
72. How do Convolutional Neural Networks work? [Internet]. [cited 2019 Jul 4]. Available from: https://brohrer.github.io/how_convolutional_neural_networks_work.html
73. Long J, Shelhamer E, Darrell T. Fully Convolutional Networks for Semantic Segmentation. ArXiv14114038 Cs [Internet]. 2014 Nov 14 [cited 2019 Jul 3]; Available from: http://arxiv.org/abs/1411.4038
74. vdumoulin. A technical report on convolution arithmetic in the context of deep learning: vdumoulin/conv_arithmetic [Internet]. 2019 [cited 2019 Jul 3]. Available from: https://github.com/vdumoulin/conv_arithmetic
75. Isola P, Zhu J-Y, Zhou T, Efros AA. Image-to-Image Translation with Conditional Adversarial Networks. ArXiv161107004 Cs [Internet]. 2016 Nov 21 [cited 2019 Jul 4]; Available from: http://arxiv.org/abs/1611.07004
76. Milletari F, Navab N, Ahmadi S-A. V-Net: Fully Convolutional Neural Networks for Volumetric Medical Image Segmentation. ArXiv160604797 Cs [Internet]. 2016 Jun 15 [cited 2019 Jul 4]; Available from: http://arxiv.org/abs/1606.04797
77. Srivastava N, Hinton G, Krizhevsky A, Sutskever I, Salakhutdinov R. Dropout: A Simple Way to Prevent Neural Networks from Overfitting. J Mach Learn Res. 2014 Jan;15(1):1929 1958.
78. Manuel. Pytorch 0.41 implementation of the U-Net for image semantic segmentation + Dataloader for ISBI 2012 Challenge: Mastercorp/U-Net-Pytorch-0.4 [Internet]. 2019 [cited 2019 Jul 3]. Available from: https://github.com/Mastercorp/U-Net-Pytorch-0.4
79. Mathieu M, Couprie C, LeCun Y. Deep multi-scale video prediction beyond mean square error. ArXiv151105440 Cs Stat [Internet]. 2015 Nov 17 [cited 2019 Jul 4]; Available from: http://arxiv.org/abs/1511.05440
80. Brunet D, Vrscay ER, Wang Z. On the Mathematical Properties of the Structural Similarity Index. IEEE Trans Image Process. 2012 Apr;21(4):1488 99.
81. Keller P, Instruments M. Technologies for Precision Magnetic Field Mapping. :16.
82. Oliphant TE. Python for Scientific Computing. Comput Sci Eng. 2007 May;9(3):10 20.

83. Paszke A, Gross S, Chintala S, Chanan G, Yang E, DeVito Z, et al. Automatic differentiation in PyTorch. 2017 Oct 28 [cited 2019 Jul 4]; Available from: https://openreview.net/forum?id=BJJsrmfCZ
84. Neuroimaging in Python — NiBabel 2.5.0dev documentation [Internet]. [cited 2019 Jul 4]. Available from: https://nipy.org/nibabel/
85. Sacred is a tool to help you configure, organize, log and reproduce experiments developed at IDSIA.: IDSIA/sacred [Internet]. IDSIA; 2019 [cited 2019 Jul 4]. Available from: https://github.com/IDSIA/sacred
86. Subramanian VR. Web-based dashboard for Sacred. Contribute to vivekratnavel/omniboard development by creating an account on GitHub [Internet]. 2019 [cited 2019 Jul 4]. Available from: https://github.com/vivekratnavel/omniboard
87. Chan K-S. Matlab GUI pipeline application for quantitative susceptibility mapping (QSM): kschan0214/sepia [Internet]. 2019 [cited 2019 Jul 4]. Available from: https://github.com/kschan0214/sepia
88. Carlos Milovic / FANSI-toolbox [Internet]. GitLab. [cited 2019 Jul 4]. Available from: https://gitlab.com/cmilovic/FANSI-toolbox
89. Cornell MRI Research Lab Research Interests [Internet]. [cited 2019 Jul 4]. Available from: http://pre.weill.cornell.edu/mri/pages/qsm.html
90. Chunlei Liu — UC Berkeley [Internet]. [cited 2019 Jul 4]. Available from: https://people.eecs.berkeley.edu/~chunlei.liu/software.html
91. Heinrich MP, Stille M, Buzug TM. Residual U-Net Convolutional Neural Network Architecture for Low-Dose CT Denoising. Curr Dir Biomed Eng. 2018;4(1):297–300.
92. Woojin J, Yoon J, Choi JY. On the linearity of deep neural network trained QSM [Internet]. [cited 2019 Jul 4]. Available from: https://index.mirasmart.com/ISMRM2019/PDFfiles/0317.html